ISSN 2074-272X

науково-практичний журнал 2021/3

Електротехніка і Електромеханіка

Electrical Engineering & Electromechanics

Теоретична електротехніка
Інженерна електрофізика.
Техніка сильних електричних та магнітних полів
Електричні машини та апарати
Електротехнічні комплекси та системи
Силова електроніка
Електроізоляційна та кабельна техніка
Електричні станції, мережі і системи

Журнал включено до найвищої категорії «А»
Переліку фахових видань України

З 2015 р. журнал індексується у міжнародній наукометричній базі Web of Science
Core Collection: Emerging Sources
Citation Index

«ELECTRICAL ENGINEERING & ELECTROMECHANICS»

Scientific Journal was founded in 2002

Founders are:

National Technical University «Kharkiv Polytechnic Institute» (Kharkiv, Ukraine)

State Institution «Institute of Technical Problems of Magnetism of the NAS of Ukraine» (Kharkiv, Ukraine)

Journal «Electrical Engineering & Electromechanics» from no. 1 2015 is indexing in Web of Science Core Collection : Emerging Sources Citation Index (ESCI).

Also included in DOAJ (Directory of Open Access Journals), in EBSCO's database, in ProQuest's databases – Advanced Technologies & Aerospace Database and Materials Science & Engineering Database, in Gale/Cengage Learning databases.

Editorial office address:

National Technical University «Kharkiv Polytechnic Institute», Kyrpychova Str., 2, Kharkiv, 61002, Ukraine

phones: +380 57 7076281, +380 67 3594696, **e-mail:** a.m.grechko@gmail.com (**Grechko O.M.)**

ISSN (print) 2074-272X

ISSN (online) 2309-3404

Printed 25 June 2021. Format 60 × 90 ⅛. Paper – offset. Laser printing. Edition 200 copies.

Printed by Printing house «Madrid Ltd» (18, Gudanova Str., Kharkiv, 61024, Ukraine)

ELECTRICAL ENGINEERING & ELECTROMECHANICS
Scientific journal

no. 3, 2021

TABLE OF CONTENTS

Electrical Machines and Apparatus

Electrotechnical Complexes and Systems

Power Electronics

Theoretical Electrical Engineering

Engineering Electrophysics. High Electric and Magnetic Field Engineering

Electrical Insulation and Cable Engineering

Power Stations, Grids and Systems

UDC 621.316 https://doi.org/10.20998/2074-272X.2021.3.01

I. Yatchev, I. Balabozov, K. Hinov, I. Hadzhiev, V. Gueorgiev

INFLUENCE OF THE SHAPE OF THE INPUT PULSES ON THE CHARACTERISTICS OF HYBRID ELECTROMAGNETIC SYSTEM WITH MAGNETIC FLUX MODULATION

Introduction. *Nowadays, the accelerated development of materials and technologies and the finding of new ones is a prerequisite for the improvement of well-known electromagnetic constructions used in various devices, as well as for the development of new ones.* ***New construction*** *of hybrid electromagnetic system with magnetic flux modulation (HEMSMM) is studied. The construction is composed of: ferromagnetic frame with air gaps, input and output coils and permanent magnets. Two input coils connected to the pulsed power supply are used to change the path of the generated by the permanent magnets constant magnetic flux. Input pulses with different shapes are applied to the input coils and signals in the output coils are obtained and compared.* ***The main purpose*** *of the work is to find the shape of the input pulses which leads to higher output power in comparison with the other shapes.* ***Methods.*** *Finite element method and COMSOL software is used for computer modelling of the proposed construction, where coupled electromagnetic field – electric circuit analysis is carried out.* ***Results.*** *A mathematical and numerical 3D model of new HEMSMM construction is realised and studied. The model allows to calculate and compare power efficiency of the studied device, when input pulses with different shapes are applied.* ***Practical value.*** *The developed computer model enables the study of the HEMSMM and other electromagnetic devices at different operating modes. It can be further improved and used in the search for optimal parameters of a particular electromagnetic device.* References 13, table 1, figures 13.

Key words: **FEM modelling, hybrid electromagnetic system, magnetic flux modulation, permanent magnets.**

Вступ. *У наш час прискорене вдосконалення існуючих і винахід нових матеріалів та обладнання є необхідною умовою вдосконалення відомих електромагнітних конструкцій, що використовуються в різних пристроях, а також для розробки нових виробів. Досліджується* ***нова конструкція*** *гібридної електромагнітної системи з модуляцією магнітного потоку (ГЕСМММ). Конструкція складається з: феромагнітної каркасу з повітряними зазорами, вхідних та вихідних котушок та постійних магнітів. Дві вхідні котушки, підключені до імпульсного джерела живлення, використовуються для зміни шляху постійного магнітного потоку, що створюється постійними магнітами. Вхідні імпульси різної форми подаються на вхідні котушки, а сигнали у вихідних котушках отримуються та порівнюються.* ***Основна мета*** *роботи – знайти форму вхідних імпульсів, що призводить до вищої вихідної потужності в порівнянні з іншими формами.* ***Методи.*** *Метод скінченних елементів та програмне забезпечення COMSOL використовуються для комп'ютерного моделювання запропонованої конструкції, де проводиться аналіз зв'язаних електромагнітного поля та електричного кола.* ***Результати.*** *Реалізовано та досліджено математичну та числову тривимірну модель нової конструкції ГЕСМММ. Модель дозволяє розрахувати та порівняти енергетичну ефективність досліджуваного пристрою, коли застосовуються вхідні імпульси різної форми.* ***Практична цінність.*** *Розроблена комп'ютерна модель дозволяє досліджувати ГЕСМММ та інші електромагнітні пристрої при різних режимах роботи. Вона може бути додатково вдосконалена та використана для пошуку оптимальних параметрів конкретного електромагнітного пристрою.* Бібл. 13, табл. 1, рис. 13.

Ключові слова: **моделювання методом скінченних елементів, гібридна електромагнітна система, модуляція магнітного потоку, постійні магніти.**

Introduction. Energy efficiency in the creation of new devices and in the modernization of existing ones is one of the basic requirements laid down in their design. The need to increase device efficiency leads to continuous search for new constructive variants and application of new materials and technologies. In electromagnetic systems, a good opportunity to increase their energy efficiency and to improve their technical parameters is the application of permanent magnets by means of which the neutral electromagnetic actuators can be replaced with polarized ones. There are also electromagnetic systems in which the magnetic flux created by a permanent magnet (PM) is redirected to parallel ferromagnetic paths using a control coil. The change of magnetic field in the system is used to generate electricity. Such devices are hybrid electromagnetic systems with magnetic flux modulation (HEMSMM).

The idea of creating a hybrid device that uses a magnetic flux of a permanent magnet in combination with a variable magnetic flux created by a coil is not new [1-3]. Some of these designs are only conceptual and not realized due to lack of available materials with suitable characteristics.

Many HEMSMM constructions with closed (without an air gap in the path of the magnetic flux) and open magnetic path (with one or more air gaps in the path of the magnetic flux) and their working principles are described in [1]. The patent application and patents of motionless magnetic generator are described in [2-6]. Electromagnetic construction with two input and two output coils and special microprocessor circuits are described in [2]. The electronic control system of that device ensures ferromagnetic resonance of the core. Several modifications of construction with built-in PM and airgaps with variable resistors is proposed in [3]. Construction with control coil that is positioned outside of the frame with main magnetic flux is presented in [4]. Combination of DC and AC current source are used for power feeding of the system. In [5], two PMs are placed close to the coil with magnetic core and airgap between them is controlled to achieve change in magnetic flux. A device with perforated disks inserted in the airgaps is presented in [6]. The control system is realized with simple multivibrators. In [7] main working principles of hybrid electromagnetic system are described and using of new nanocrystalline materials for better energy efficiency of such devices is proposed. A three-dimensional computer model of magnetic field is used for studying influence of geometry of permanent magnet over the

energy efficiency of an electromechanical system in [8]. Basic theoretical principles and formulations related to electromagnetism and magnetic field are discussed in [9] and [10].

The goal of the paper is to study the influence of input pulses with different parameters, mainly their shape, on the characteristics of a new construction of HEMSMM. The obtained results from the FEM simulations are compared.

Studied construction. Previous research by the authors for HEMSMM device is published in [11], where an existing simple construction with one PM and two control coils is studied. Also, an experimental study with a prototype of the HEMSMM system was conducted by the authors in [12]. In the present paper, a new construction with two built-in permanent magnets (PMs) in ferromagnetic core is presented. The path of magnetic flux from the PMs is controlled with two input coils which are supplied with voltage pulses with different shapes. It is also possible to set different amplitude, frequency and filling factor of the voltage pulses. In the ferromagnetic core, where the input coils are mounted, two air gaps are included in the centre of the coils. Four output coils are connected to resistive load and the output power is determined.

In Fig. 1, the main parts of the studied construction are shown. They are:

- 1 – ferromagnetic frame;
- 2 – input (control) coil 1;
- 3 – input (control) coil 2;
- 4 – output (signal) coil 6;
- 5 – output (signal) coil 5;
- 6 – output (signal) coil 4;
- 7 – output (signal) coil 3;
- 8 – permanent magnets;
- 9 – air gaps.

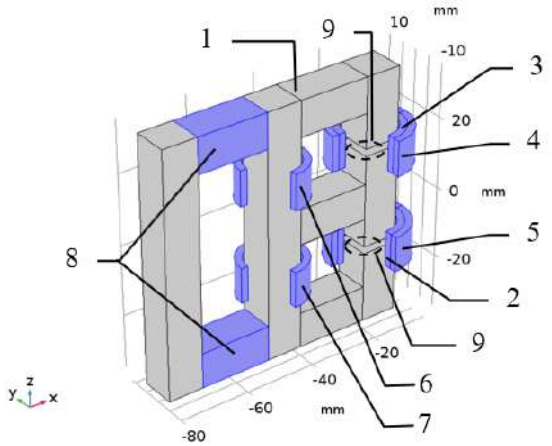

Fig. 1. Geometry of the studied new HEMSMM construction

Mathematical and numerical model. COMSOL Multiphysics [13] software is used for computer modelling, where coupled 3D electromagnetic field – electric circuit problem is solved. Inductance and active resistance of the coils are obtained from electromagnetic field interface and are directly employed in electric circuit. An active load is connected to the output coil. The influence of the shape of the input (voltage) pulses applied to the control coils is studied. Simulations with sinusoidal, rectangular and triangular pulses are made. The electric circuit used in the simulations is given in Fig. 2.

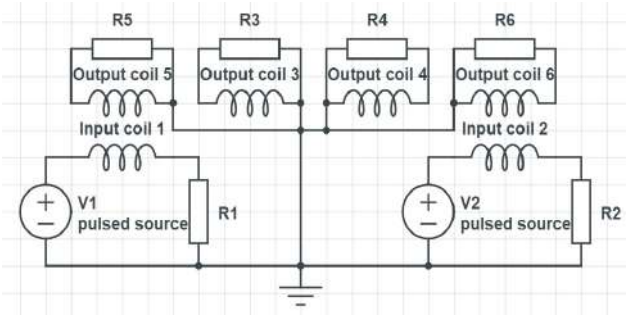

Fig. 2. Electric circuit used in the simulations

The mathematical model consists of one field equation and 6 circuit equations (one for each coil). The computer model with studied HEMSMM construction is solved in two steps. In the first step, the electric circuit does not participate and a stationary problem with respect to the electromagnetic field is solved. Results for the static magnetic field created only by the permanent magnets are achieved and are used as initial condition for the next step. In second step, time dependent coupled field-circuit problem is solved. Here, the coils are connected and powered by the electric circuit in Fig. 2.

All simulations can be also used to study the system for different frequencies and duty cycle of the input pulses.

Field equation for the first step (static case) is:

$$\nabla \times \left(\mu_0^{-1} \nabla \times \boldsymbol{A} - \boldsymbol{M} \right) = 0 , \quad (1)$$

where $\boldsymbol{A}$ is the magnetic vector potential; $\boldsymbol{M}$ is the magnetization; μ_0 is the magnetic permeability of vacuum.

Field equation for time dependent step is:

$$\sigma \cdot \frac{\partial \boldsymbol{A}}{\partial t} + \nabla \times \left(\mu_0^{-1} \nabla \times \boldsymbol{A} - \boldsymbol{M} \right) = N \cdot \frac{i(t)}{S} , \quad (2)$$

where σ is the electrical conductivity of the material; N is number of turns in the coil; i is the current through the coil; S is the coil cross section.

The circuit equations for the six coils are:

$$u_1(t) = R_1 \cdot i_1(t) + \partial \Psi_1 / \partial t ; \quad (3)$$

$$u_2(t) = R_2 \cdot i_2(t) + \partial \Psi_2 / \partial t ; \quad (4)$$

$$-\partial \Psi_3 / \partial t = R_3 \cdot i_3(t) ; \quad (5)$$

$$-\partial \Psi_4 / \partial t = R_4 \cdot i_4(t) ; \quad (6)$$

$$-\partial \Psi_5 / \partial t = R_5 \cdot i_5(t) ; \quad (7)$$

$$-\partial \Psi_6 / \partial t = R_6 \cdot i_6(t) , \quad (8)$$

where $u_1(t)$ and $u_2(t)$ are voltages of coil 1 and coil 2 respectively; R_1 to R_6 are active resistances of the coils; $i_1(t)$ to $i_6(t)$ are currents through the coils; Ψ is flux linkage.

Some of the main parameters used in computer modelling of the construction are:

- all coils are cylindrical with 100 turns made of copper conductor;
- the magnetic frames are of ferromagnetic material of *B-H* curve presented in Fig. 3. The cross section of the frame is 10×10 mm;

• the permanent magnets are modelled with relative permeability μ_r = 1.05 and coercive force of 970 kA/m.

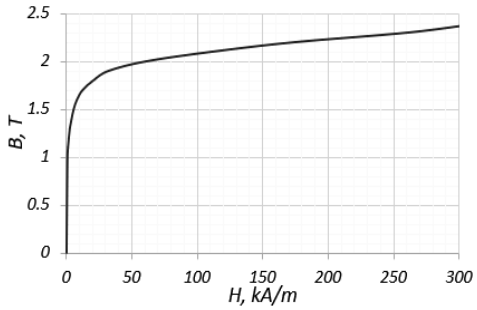

Fig. 3. *B-H* curve of used ferromagnetic material used in the modelling

Results from simulations. Distribution of the magnetic flux density of the studied construction, when the control coils are not energized is shown in Fig. 4. In this case the fluxes are due to PMs built in the ferromagnetic frame.

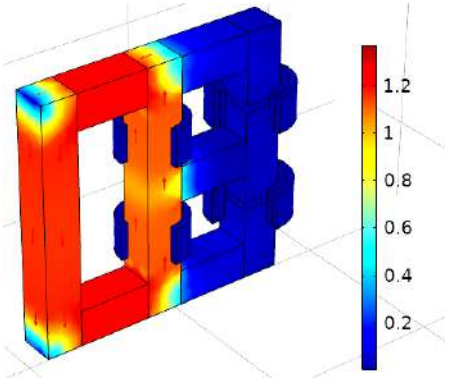

Fig. 4. Magnetic flux density of the studied HEMSMM construction, when the input coils are not energized

The flux density working point of the permanent magnet is close to the point of the remanent flux density and its variation is less than 1 %. The change of magnetic flux density in the system, when voltage pulses are applied to the input coil 1 and to input coil 2, is presented in Fig. 5.

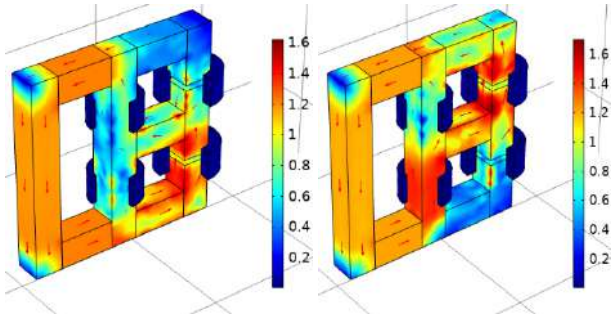

a *b*

Fig. 5. Magnetic flux density of the studied HEMSMM construction:
a) power supply of input coil 1
b) power supply of input coil 2

In Fig. 6 to Fig. 8, results for the voltage of input coil 1 and output coil 5, when different shapes of input pulses are applied, are presented. Due to similarity, the results for the other coils are not given.

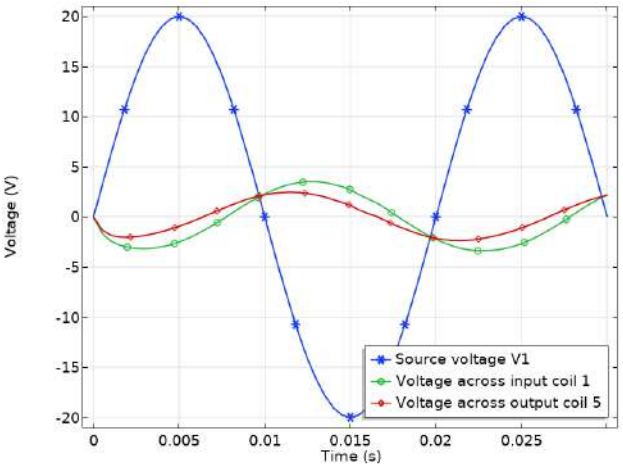

Fig. 6. Voltage of input coil 1 and output coil 5 with sinusoidal waveforms

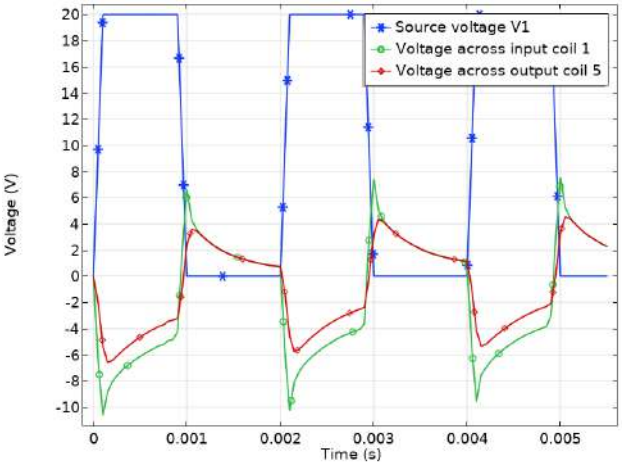

Fig. 7. Voltage of input coil 1 and output coil 5, pulses with rectangular shape

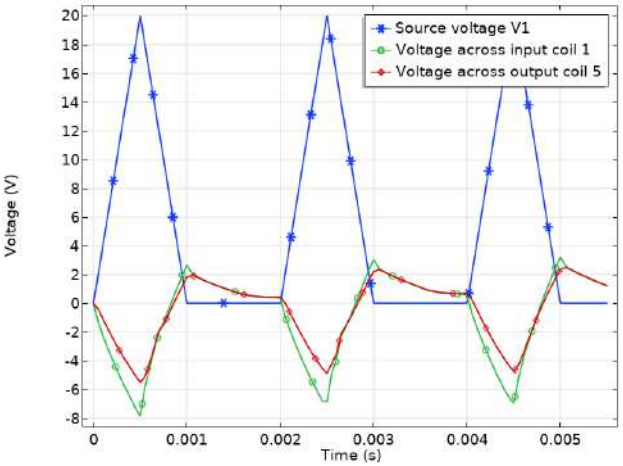

Fig. 8. Voltage of input coil 1 and output coil 5, pulses with triangular shape

Currents through input and output coils in the system for two of the cases (rectangular and triangular pulses) are given in Fig. 9 and Fig. 10. It is worth to note that the current through output coils 3 and 4 is closer to sinusoidal form when the input pulses are triangular, the reason for that is the slower changing of the magnetic fluxes in the magnetic core of that zone of the system, when triangular pulses are applied.

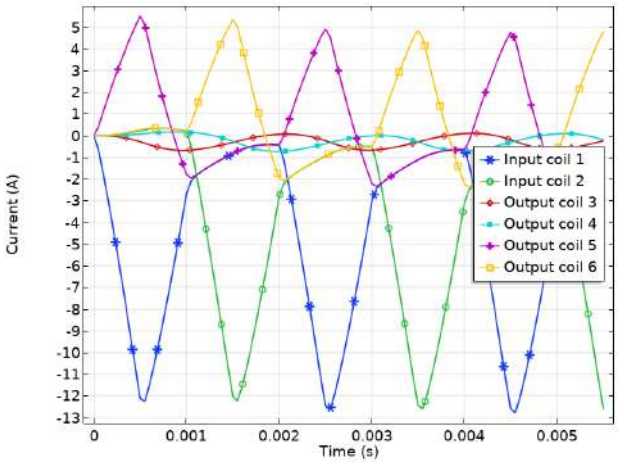

Fig. 9. Currents through the coils when triangular pulses are applied

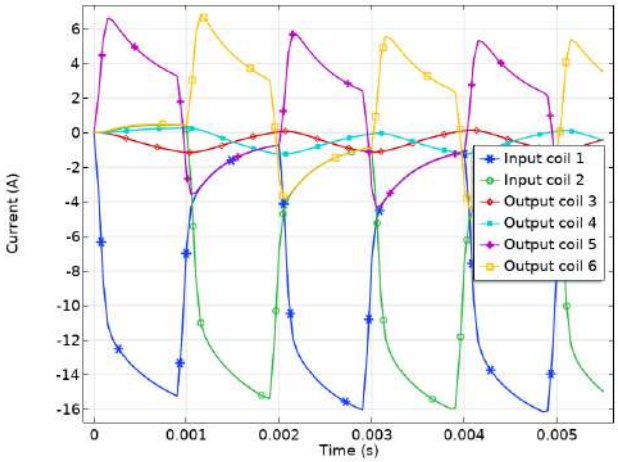

Fig. 10. Currents through the coils when rectangular pulses are applied

Results for the input and output power of each coil of the system and for the studied three different shapes (sinusoidal, rectangular and triangular) of the input pulses, are obtained. Some of the results are shown in Fig. 11 to Fig. 13.

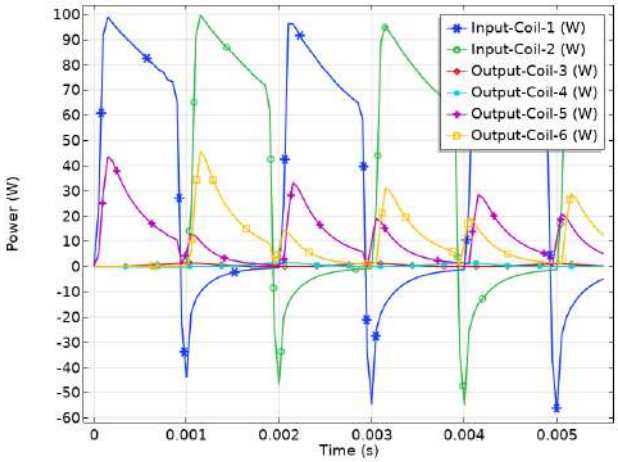

Fig. 11. Input and output power when rectangular pulses are applied

When rectangular pulses are used, the shape of output power does not match the input power shape. In the case with triangular pulses, the shapes of input and output power match better.

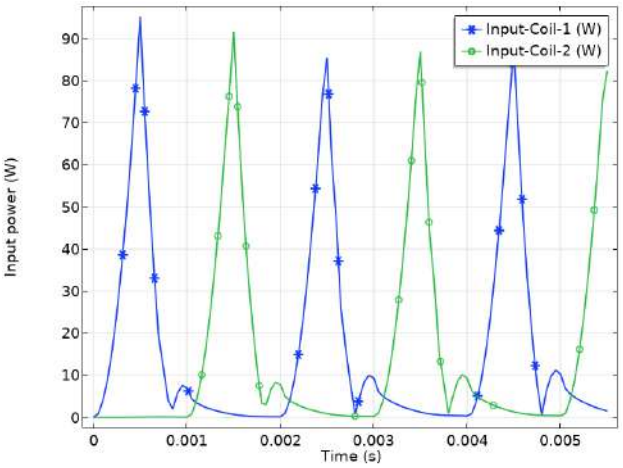

Fig. 12. Input power when triangular pulses are applied

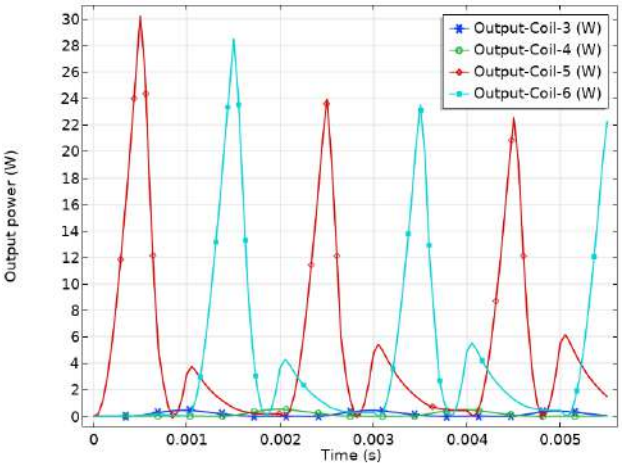

Fig. 13. Output power when triangular pulses are applied

The average input and output power of the coils is calculated and is presented in Table 1, where and comparison is made and efficiency of the system for input pulses with different shapes is achieved.

Table 1

Comparison of input and output power of the studied system

Shape of the input power pulse	Average input power (coil 1 + 2)	Average output power (coils 3 + 4 + 5 + 6)	Efficiency
Sinusoidal	46,14 W	8,10 W	17,55 %
Rectangular	60,69 W	22,25 W	36,66 %
Triangular	24,44 W	9,73 W	39,82 %

The table shows the results obtained for the average input and output power of the system under different shapes of the input power pulses.

Conclusions.

The developed computer model enables the study of the hybrid electromagnetic system with magnetic flux modulation at different operating modes. For the proposed construction, the influence of the shape of the input power pulses on the efficiency of the system is studied. From the results obtained for the studied pulse shapes, the best results with respect to the efficiency are obtained with triangular pulses. The developed computer models can also be used to investigate other parameters, as well as to optimize the design of such devices.

Acknowledgment.

The present work is supported by the National Science Fund of Bulgarian Ministry of Education and Science, Project No. DN 17/13.

Conflict of interest. The authors declare that they have no conflicts of interest.

REFERENCES

1. Kunel H. Procedures and devices for energy production. Patent DE3024814, 1982.

2. Suarez J. Estatico processor electrical power. ES Patent 2265253 B1, 2008.

3. Matsanov R. Pulse generator. Patent WO2010094993A1, 2010.

4. Tatevosian A.S., Tatevosian A.A., Dorokhin V.N. Permanent magnet machine. RU Patent 2542322 C2, 2015.

5. Fridrich J. Electric power generation device. Patent CZ305224B6, 2015.

6. Gleich A. Permanent magnet-driven current generator. Patent application DE102014017612A1, 2016.

7. Karastoyanov D. Hybrid electromagnetic systems for energy efficiency of electrical systems. *AIP Conference Proceedings*, vol. 2022, 6 November 2018, art. no. 020016. doi: https://doi.org/10.1063/1.5060696.

8. Leonov S.V., Zhiganov A.N., Kerbel'B.M., Fedorov D.F., Makaseev Y.N., Kremlev I.A. Analysis of the influence of permanent magnet geometry on the energy efficiency of electromechanical systems. *Russian Physics Journal*, 2016, vol. 59, no. 2, pp. 308-313. doi: https://doi.org/10.1007/s11182-016-0772-1.

9. Hacker V., Sumereder Ch. 5. The magnetic field. *Electrical Engineering*, Berlin, Boston, De Gruyter Oldenbourg, 2020, pp. 91-108. doi: https://doi.org/10.1515/9783110521115-005.

10. Gunther L. Electricity, Magnetism, and Electromagnetic Waves. *The Physics of Music and Color*, Springer, Cham, 2019. doi: https://doi.org/10.1007/978-3-030-19219-8_5.

11. Yatchev I., Balabozov I., Hinov K., Minchev M., Gueorgiev V. Electromagnetic field analysis of a hybrid electromagnetic system with magnetic flux modulation with one permanent magnet and two collecting coils. *2018 20th International Symposium on Electrical Apparatus and Technologies (SIELA)*, 2018, pp. 1-4. doi: https://doi.org/10.1109/siela.2018.8447108.

12. Balabozov I., Tomov D., Yatchev I., Hadzhiev I., Brauer H. Experimental study of the influence of some parameters on the characteristics of hybrid electromagnetic system with magnetic flux modulation. *2020 21st International Symposium on Electrical Apparatus & Technologies (SIELA)*, 2020, pp. 1-4. doi: https://doi.org/10.1109/siela49118.2020.9167093.

13. COMSOL Multiphysics 5.3 User's Guide, COMSOL, Inc., 2018.

Received 29.03.2021
Accepted 11.05.2021
Published 25.06.2021

Ivan Yatchev[1], *Doctor of Technical Sciences, Professor,*
Iosko Balabozov[1], *PhD, Associate Professor,*
Krastyo Hinov[1], *PhD, Associate Professor,*
Ivan Hadzhiev[2], *PhD, Assistant Professor,*
Vultchan Gueorgiev[1], *PhD, Associate Professor,*
[1] Technical University of Sofia,
8 Kl. Ohridski Blvd, 1000, Sofia, Bulgaria,
e-mail: yatchev@tu-sofia.bg (Corresponding author),
i.balabozov@tu-sofia.bg, k_hinov@yahoo.co.uk,
vulchy@tu-sofia.bg
[2] Technical University of Sofia, Plovdiv Branch,
25 Tsanko Dyustabanov Str., 4000 Plovdiv, Bulgaria,
e-mail: hadzhiev_tu@abv.bg

How to cite this article:
Yatchev I., Balabozov I., Hinov K., Hadzhiev I., Gueorgiev V. Influence of the shape of the input pulses on the characteristics of hybrid electromagnetic system with magnetic flux modulation. *Electrical Engineering & Electromechanics*, 2021, no. 3, pp. 3-7. doi: https://doi.org/10.20998/2074-272X.2021.3.01.

UDC 621.3 https://doi.org/10.20998/2074-272X.2021.3.02

H. Benbouhenni, S. Lemdani

COMBINING SYNERGETIC CONTROL AND SUPER TWISTING ALGORITHM TO REDUCE THE ACTIVE POWER UNDULATIONS OF DOUBLY FED INDUCTION GENERATOR FOR DUAL-ROTOR WIND TURBINE SYSTEM

Aim. *This work presents the amelioration of direct power control using synergetic-super twisting algorithms for asynchronous generators integrated into dual-rotor wind turbine systems.* ***Method.*** *The main role of the direct power control is to control the active and reactive powers and reduce the harmonic distortion of stator current of asynchronous generator for variable speed dual-rotor wind turbine systems. The traditional strategy is more attractive due to its high efficiency and simple algorithm. Super twisting algorithms are a non-linear command strategy; characterized by robustness against the parameters change or disturbances, it gives a good power quality under different conditions such as changing generator parameters.* ***Novelty.*** *Synergetic-super twisting algorithms are designed. Synergetic-super twisting algorithms construction is based on synergetic command and super twisting algorithms in order to obtain a robust control strategy and a fast system with acceptable precision. We use in our study a 1.5 MW asynchronous generator integrated to dual-rotor wind turbine system in order to regulate the active and reactive powers.* ***Results.*** *As shown in the results figures using synergetic-super twisting algorithms the ameliorate performances especially minimizes the torque, active and reactive power undulations, and reduces harmonic distortion of stator current (THD = 0.19 %) compared to traditional strategy.* References 40, tables 2, figures 28.

Key words: **super twisting algorithm, synergetic command, asynchronous generator, direct active and reactive power command.**

Мета. *Робота представляє вдосконалення безпосереднього регулювання потужності за допомогою синергетичих алгоритмів супер-скручування для асинхронних генераторів, інтегрованих у системи вітряних генераторів з подвійним ротором.* ***Метод.*** *Основна роль безпосереднього регулювання потужності полягає у керуванні активною та реактивною потужностями та зменшенні гармонічних спотворень струму статора асинхронного генератора для вітряних генераторів з подвійним ротором зі змінною швидкістю обертання. Традиційна стратегія є більш привабливою завдяки її високій ефективності та простому алгоритму. Алгоритми супер-скручування – це нелінійна командна стратегія; характеризується стійкістю до зміни параметрів або порушень, це забезпечує хорошу якість енергії в різних умовах, таких як зміна параметрів генератора.* ***Новизна.*** *Розроблені синергетичні алгоритми супер-скручування. Побудова алгоритмів синергетичного супер-скручування базується на алгоритмах синергетичних команд та супер-скручування, для того щоб отримати надійну стратегію керування та швидку систему з прийнятною точністю. У нашому дослідженні ми використовуємо асинхронний генератор потужністю 1,5 МВт, інтегрований в систему вітряних турбін з подвійним ротором для регулювання активної та реактивної потужностей.* ***Результати.*** *Як показано на рисунках з результатами, із використанням алгоритмів синергетичного супер-скручування, покращені характеристики особливо мінімізують крутний момент, коливання активної та реактивної потужності та зменшують гармонічні спотворення струму статора (THD = 0,19%) порівняно з традиційною стратегією.* Бібл. 40, табл. 2, рис. 28.

Ключові слова: **алгоритм супер-скручування, синергетична команда, асинхронний генератор, команда прямої активної та реактивної потужності.**

Introduction. Nowadays, the increasing demand for electrical energy, its sources and the ever-increasing consumption has allowed more attention to be given to the design of commands and techniques through which high-quality, undulations-free energy can be obtained. Also, the global warming crisis has created more competition between countries and university researchers. On the other hand, and the use of oil is no longer an option because it causes an increase in global warming and thus exacerbates the global crisis. Endangering human health and social stability for the sake of primary services such as electricity grids, transportation and communication systems, and the production of goods does not exist without thinking of a way to reduce global warming and emissions into the atmosphere.

In the field of electric power generation, the use of wind energy and renewable sources is essential to reduce the greenhouse effect. For these reasons, it has been suggested to use wind energy in generating electric power, and the most important advantage is that it is free to generate electricity and reduce the emission of toxic gases in to the atmosphere, regardless of the negative aspects of using wind energy. This source prevents the risks of increasing global warming. On the other hand, the financial cost and the difficulty of implementation and control increase the possibility of not using wind energy, which could cause an increase in the demand for the use of non-renewable resources such as gas, for example, and thus an increase in the emission of CO_2. Also, an increase in the cost of producing electrical energy, which leads to imposing taxes on electric energy consumption.

In the field of electric power generation, there are several electric generators used in generating electric energy using wind energy, for example, asynchronous and synchronous generators.

In our work, we will study the asynchronous generator (ASG) in generating electrical energy using a renewable source. Among the advantages of using an ASG is that it is solid and simple to command, unlike other generators [1]. In the industrial field, there are several types of command methods for electrical machines, especially electrical generators. Among these methods, we mention direct torque command [2], direct power command [3], hybrid command [4], and artificial intelligence use command [5]. Direct power command is

among the other methods used. This method has its pros and cons just like the other methods, an easy and uncomplicated way, all generators can be converted. Among its disadvantages, we find ripples in the active and reactive powers, which are the most prominent negatives that characterized them. There are several scientific studies in this field that have concluded that fluctuations in reactive and active power oscillations can be reduced by using modern technologies such as fuzzy logic [6], neural networks [7], neuro-fuzzy command [8], sliding mode control (SMC) technique [9], genetic algorithm [10], synergetic control (SYC) [11], super twisting algorithm (STA) [12], etc.

The sliding mode is a particular operating mode of variable structure systems. It is considered one of the simplest approaches for controlling nonlinear systems and systems with an imprecise model. This command has the following characteristics [13]:

- the response of the system is insensitive and robust to variations in certain parameters and the effects of load disturbances and disturbances;
- it suffices to know a terminal for $u(t)$ which simplifies the adjustment;
- it choice of the switching surface is fairly free;
- the order is softened by the presence of the equivalent order, which can be deleted at the cost of an increase of $u(t)$.

The sliding surface S is a scalar function such that the variable to be adjusted slides on this surface. The purpose of the command is to keep the surface at zero. The main drawback of the command in higher-order sliding mode lies in the need to know the state variables and their derivatives. A sliding regime of order r (noted r-sliding) acts on the surface and its $(r - 1)$ first successive derivatives to time. The objective is to force the system to evolve not only on the surface but also on its $(r - 1)$ first successive derivatives and to keep the sliding set at zero:

$$S = \dot{S} = \ddot{S} = ... = \left(S^{r-1}\right) = 0 ,$$

with r designates the relative degree of the system, and its $(r–1)$ first successive derivatives with respect to time.

STA algorithm is a kind of high-order SMC technique. It is characterized by simplicity and durability compared to some techniques. This method was proposed by the Levant in 1993 [14]. This method has been applied in several fields [15-19]. Furthermore, the SYC method is also applied. It tries to overcome the problem of controlling the power converter by using the internal dynamic characteristics of the system, the most important advantages of this approach are order reduction, decoupling design procedure, and insensitivity to parameter changes [20]. On the other hand, this method reduces the vibrations present in the sliding command and improves the stability of the system [21].

A new nonlinear control has been proposed in this paper. This proposed nonlinear control is based on STA algorithms and synergetic control theory.

The **aim** of this work is the improve the performance of direct reactive and active power control (DRAPC) using synergetic-super twisting algorithms (SYSTA) for ASG-based dual-rotor wind power (DRWP) system under variable speed wind and also to reduce fluctuations in torque, current and active power.

This method is called SYSTA, and it is the product of a marriage of properties of both synergetic control and STA algorithms. This method can be applied to all controls without exception, and it has provided very satisfactory results compared to the classical method.

Model of DRWP. Traditionally, the applied systems of wind turbine systems can be classified into variable speed (VS) and fixed speed turbines (FST). The VS turbine systems (VSTSs) are now more often applied than the systems with FST. The main advantages of VSTSs are: increasing the production of wind power, the ability to achieve maximum power conversion efficiency, and reduction of mechanical stresses. On the other hand, the DRWP is a wind turbine used to generates electrical power. The DRWP system has been proposed as new wind energy, as shown in Fig. 1.

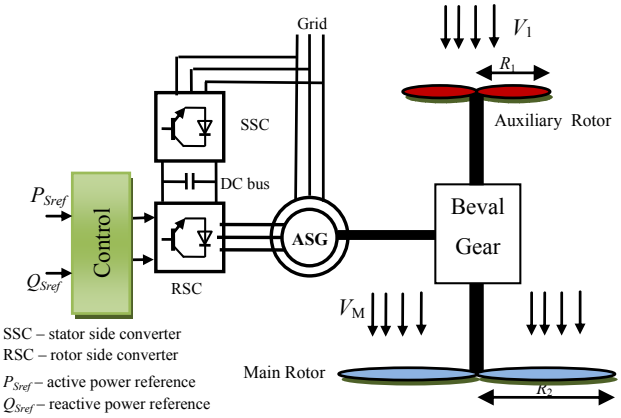

Fig. 1. Block diagram of DRWP with a ASG

The aerodynamic torque of the auxiliary rotor is [22]:

$$T_A = \frac{1}{2 \cdot \lambda_A^3} \cdot \rho \cdot \pi \cdot R_A^5 \cdot C_p \cdot w_A^2 , \quad (1)$$

and aerodynamic torque of the main rotor is:

$$T_M = \frac{1}{2 \cdot \lambda_M^3} \cdot \rho \cdot \pi \cdot R_A^5 \cdot C_p \cdot w_M^2 , \quad (2)$$

where λ_A, λ_M are the tip speed ration of the auxiliary and main rotors; R_M, R_A are the blade radius of the main and auxiliary rotors, ρ is the air density; w_A, w_M are mechanical speed of the auxiliary and main rotors; C_p is the power coefficient

The tip speed ratio of the auxiliary rotor (AR) is:

$$\lambda_A = \frac{w_A \cdot R_A}{V_1} , \quad (3)$$

and the tip speed ratio of the main rotor (MR) is:

$$\lambda_M = \frac{w_M \cdot R_M}{V_M} , \quad (4)$$

where V_M is the speed of the unified wind on main rotor and V_1 is the wind speed on an auxiliary wind turbine (AWT).

The total aerodynamic torque of DRWP (T_T) is the sum of AR torque (T_A) and the MR torque (T_M):

$$T_{DRWT} = T_T = T_A + T_M. \quad (5)$$

The wind speed on the auxiliary and main turbines is the essential element to calculating the tip speed ratio. Equation (6) represents the wind speed in the main turbine [23]

$$V_x = V_1\left(1-\frac{1-\sqrt{(1-C_T)}}{2}\cdot\left(1+\frac{2\cdot x}{\sqrt{1+4\cdot x^2}}\right)\right), \quad (6)$$

where x is the non-dimensional distance from the auxiliary rotor disk, V_x is the velocity of the disturbed wind between rotors at point x; C_T is the trust coefficient, which is taken 0.9 [24]. The distance between the main and the auxiliary turbines is 15 m.

The C_p is given as:

$$C_p(\lambda,\beta) = \frac{1}{\lambda+0.08\beta} - \frac{0.035}{\beta^3+1}, \quad (7)$$

where λ is the tip speed ratio; β is pitch angle.

Synergetic-super twisting algorithm. A system with variable structure is a system whose structure changes during its operation, it is characterized by the choice of a structure and switching logic. This choice allows the system to switch from one structure to another at any time. Moreover, such a system can have new properties which do not exist in every structure.

In the control of systems with variable structure by sliding mode, the state trajectory is brought to a surface, then using the switching law, it is forced to stays in the vicinity of this surface, this latter is called surface sliding movement and the movement along which occurs is called sliding movement [25].

During the last century, many nonlinear methods have been proposed for controlling electrical machines. Among the most famous of them we find control by slip control and this is due to the simplicity of the method and durability. Recently a new theory has appeared called synergetic control [26]. This method is more simple and uncomplicated based on the area derivation calculation. The SYC theory is one of the new methods of robust control [27]. It is characterized by its external disturbance rejection capabilities, simplicity of design, and the global stability assurance of the system [28]. The SYC method is a strategy quite close to the SMC strategy in the sense that it forces the system to evolve with a dynamic pre-chosen by the designer. This novel technique does not require the linearization of the model and explicitly uses a nonlinear model for the synthesis of the control. Also, the SYC method eliminates more the chattering phenomenon compared than the SMC strategy [29].

Equation (8) illustrates the principle of the SYC method, as it depends on the derivation of the surface

$$T\dot{S}(x)+S(x)=0, \quad (8)$$

where $T>0$ is a speed of convergence of surfaces to the intersection of manifolds $S=0$.

The following to ensure the stability of SYC method: $S(0)=0$, $S(x)x>0$ for all $x\neq 0$.

The solution of Eq. (8) is given by:

$$S(t)=\dot{S}_0 e^{t/T}. \quad (9)$$

Basically, STA design follows two steps to implement. In the STA strategy, the command input applies on the second-order derivative of the sliding surface, reverses the SMC it acts on the first derivative of the sliding surface [30]. The command input of the STA method comprises two inputs as (10)

$$w(t)=w_1+w_2, \quad (10)$$

where:

$$w_1(t)=\lambda_1\sqrt{|S|}\cdot sign(S), \quad (11)$$

$$w_2(t)=\lambda_2\int sign(S)dt. \quad (12)$$

The designed strategy has the same objective as the STA and SYC method, it will force the state trajectory to operate on the surface $S=0$. The surface is selected according to system constraints. The proposed method is a combination of the STA and SYC method. This proposed controlled named SYSTA algorithm, where this controller is a simple structure and more robust compared to SYC and STA techniques. Our goal for this controller is to minimize more and more the active and reactive power undulations.

Equation (13) illustrates the principle of the SYSTA controllers

$$u(t)=u_1(t)+u_2(t). \quad (13)$$

where the $u_1(t)$ and $u_2(t)$ represent the STA method and the synergetic command, respectively

$$u_1(t)=\alpha_1\sqrt{|S(t)|}\cdot sign(S(t))+\alpha_2\int sign(S(t))dt, \quad (14)$$

$$u_2(t)=\alpha\frac{dS(t)}{dt}+S(t). \quad (15)$$

The command input of the designed SYSTA method is obtained as (16)

$$u(t)=\alpha_1\sqrt{|S(t)|}\cdot sign(S(t))+\alpha_2\int sign(S(t))dt+ \\ +\alpha\frac{dS(t)}{dt}+S(t), \quad (16)$$

where the tuning constants α, α_1 and α_2 are used to tune the SYSTA technique to smoothen the regulator.

This is the design process using the SYSTA controller for the DRAPC method. On the other hand, Fig. 2 shows a block diagram representation of the SYSTA technique for DRAPC command in DRWP systems.

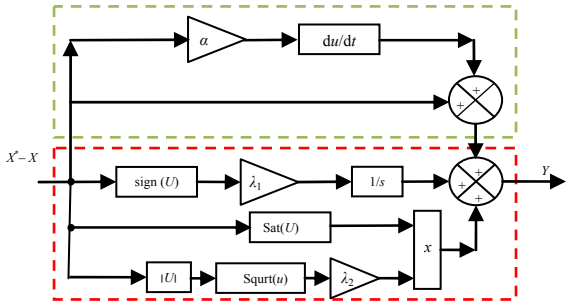

Fig. 2. Structure of the command law of the proposed SYSTA technique

This designed command is used in this work for minimizing electromagnetic torque, rotor current, active power, reactive power, and rotor flux undulations in an ASG-based DRWP system using the DRAPC method which the inverter was controlled by the modified space vector modulation (SVM) technique.

DRAPC technique. The principle of the DRAPC strategy is the direct regulation of the reactive and active

powers of the generator, by applying different voltage vectors to the inverter, which determines its state. The two controlled variables are active and reactive powers which are usually controlled by hysteresis comparators. The idea is to keep the reactive power quantities and the active powers within these hysteresis bands. The output of these regulators determines the optimum voltage vector to be applied at each switching instant [31].

This technique involves the operation of the inverter at two standard levels with a variable control frequency which is sometimes high and incompatible with high power applications due to the level of switching losses.

Two command techniques have been used to implement DRAPC commands:

- command by a lookup table;
- command by a SVM technique.

The purpose of a DRAPC strategy is to keep the reactive power and active power modulus within the hysteresis bands by choosing the output voltage of the inverter. When the active power or reactive power modulus reaches the upper or lower limit of the hysteresis, an appropriate voltage vector is applied to bring the relevant magnitude back from its hysteresis band. To study the basic principle of the main direct control strategies of the ASG, it is essential to be able to characterized the behavior of the main variables which govern the power state of the generator, namely the reactive power and the active power. To this end, we will establish below rules of behavior of the reactive power and the active power on the scale of the sampling period, thus allowing the establishment of a relation between the application of a voltage vector and the direction of variation of these variables.

The basic structure of the DRAPC strategy is shown in Fig. 3, inverter command is instantaneous, which requires a very small sampling period.

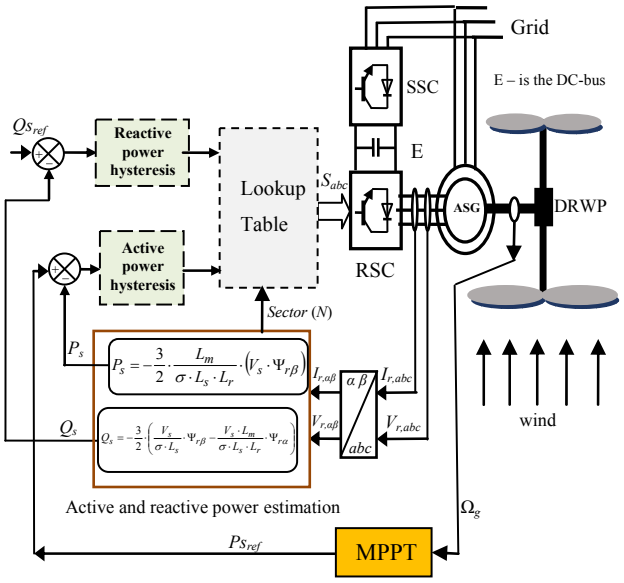

Fig. 3. Traditional DRAPC command technique

The principle is the direct regulation of the reactive and active powers of the ASG by applying the various voltage vectors of the rotor inverter, which rotor flux (Ψ_r) determines its state. The two controlled variables are the active power and the reactive power which are controlled by hysteresis regulators. In a DRAPC strategy, it is preferable to work with a high calculation frequency to reduce the reactive and active power oscillations caused by the regulators [32]. A voltage inverter achieves seven distinct positions in the phase plane, corresponding to the eight sequences of the voltage vector at the output of the rotor inverter [33].

The reactive power Q_s is expressed as a function of the quadrature rotor flux and the direct rotor flux as follows:

$$Q_s = -\frac{3}{2}\cdot\left(\frac{V_s}{\sigma\cdot L_s}\cdot\Psi_{r\beta} - \frac{V_s\cdot L_m}{\sigma\cdot L_s\cdot L_r}\cdot\Psi_{r\alpha}\right). \quad (17)$$

The active power command depends directly on the control of the rotation of the rotor flux vector.

$$P_s = -\frac{3}{2}\cdot\frac{L_m}{\sigma\cdot L_s\cdot L_r}\cdot\left(V_s\cdot\Psi_{r\beta}\right). \quad (18)$$

The rotor flux Ψ_r can be estimated from measurements of the stator current and voltage of the generator.

From the equation:

$$\Psi_r = \int_0^t (V_r - R_r\cdot i_r)dt\,, \quad (19)$$

we obtain the components α and β of the vector Ψ_r:

$$\begin{cases}\Psi_{r\alpha} = \int_0^t (V_{r\alpha} - R_r\cdot i_{r\alpha})dt;\\ \Psi_{r\beta} = \int_0^t (V_{r\beta} - R_r\cdot i_{r\beta})dt.\end{cases} \quad (20)$$

The rotor flux amplitude is given by:

$$\Psi_r = \sqrt{\Psi_{r\alpha}^2 + \Psi_{r\beta}^2}\,, \quad (21)$$

where

$$\left|\overline{\Psi_r}\right| = \left|\overline{V_r}\right| \Big/ w_r\,. \quad (22)$$

The rotor flux (θ_r) angle is calculated by:

$$\theta_r = \text{arctg}\left(\frac{\Psi_{r\beta}}{\Psi_{r\alpha}}\right). \quad (23)$$

The estimation of the reactive power and the active power requires prior knowledge of the components of the current and those of the stator voltage. It is retained in the case of a nonlinear command applied to the ASG in particular and especially the command by DRAPC strategy.

Figure 4 shows the logic output deviation HC_p of the controller following the evolution of the active power (P_s) compared to the reference active power (Ps_{ref}).

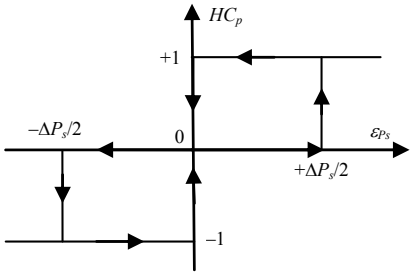

Fig. 4. Active power hysteresis comparator

This corrector makes it possible to command the generator in both directions of rotation, either for a positive or negative active power.

The corrector output, presented by the Boolean variable HC_p indicates directly whether the active power amplitude must be increased in absolute value (HC_p = 1) for a positive setpoint and (HC_p = –1) for a negative setpoint, or reduced (HC_p = 0) this corrector allows a rapid decrease in active power.

This comparator is modeled by the following algorithm, such that HC_p represents the output state of the comparator and ΔP_s the limit of the hysteresis band

$$\begin{cases} \text{if } E_{PS} < \Delta P_s \text{ so } HC_p = 1; \\ \text{if } 0 \le E_{PS} < \Delta P_s \text{ and } \dfrac{dE_{PS}}{dt} > 0 \text{ so } HC_p = 0; \\ \text{if } 0 \le E_{PS} < \Delta P_s \text{ and } \dfrac{dE_{PS}}{dt} < 0 \text{ so } HC_p = 1; \\ \text{if } E_{PS} < -\Delta P_s \text{ so } HC_p = -1; \\ \text{if } -\Delta P_s \le E_{PS} \le 0 \text{ and } \dfrac{dE_{PS}}{dt} > 0 \text{ so } HC_p = 0; \\ \text{if } -\Delta P_s \le E_{PS} \le 0 \text{ and } \dfrac{dE_{PS}}{dt} < 0 \text{ so } HC_p = -1, \end{cases} \tag{24}$$

where $E_{Ps} = P_{Sref} - P_S$.

Its purpose to keep the end of the reactive power (Q_s) in a circular crown as shown in Fig. 5. The output of the corrector must indicate the direction of evolution of the modulus of Q_s, in order to select the corresponding voltage vector.

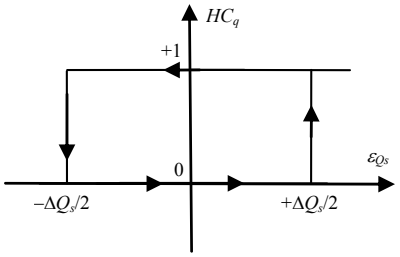

Fig. 5. Reactive power hysteresis comparator

For this, a simple two-level hysteresis corrector is ideal, and also allows very good dynamic performance to be obtained.

The output of the corrector is represented by a Boolean variable (HC_q) and indicates directly whether the amplitude of the flow must be increased (HC_q = 1) or decreased (HC_q = 0) in order to maintain:

$$\left| Q_s^* - Q_s \right| \le \varepsilon_{Qs} = \Delta Q_s \,, \tag{25}$$

where Q_s^* = Q_{Sref} is the reactive power reference; ΔQ_s is the corrector hysteresis width; ε_{Qs} is half the width of the corrector hysteresis band.

The choice of the voltage vector to apply depends on the sign of the error between the reference reactive power Q_{Sref} and the estimated reactive power

$$\begin{cases} HC_q = 1 \text{ for } E_{Qs} > \varepsilon_{Qs}; \\ HC_q = 0 \text{ for } E_{Qs} < \varepsilon_{Qs}. \end{cases} \tag{26}$$

We can write like this:

$$\begin{cases} \text{if } E_{Qs} < \Delta Q_s \text{ so } HC_q = 0; \\ \text{if } 0 \le E_{Qs} \le \Delta Q_s \text{ and } \dfrac{dE_{Qs}}{dt} > 0 \text{ so } HC_q = 0; \\ \text{if } 0 \le E_{Qs} \le \Delta Q_s \text{ and } \dfrac{dE_{Qs}}{dt} < 0 \text{ so } HC_q = 1; \\ \text{if } E_{Qs} < -\Delta Q_s \text{ so } HC_q = 0. \end{cases} \tag{27}$$

Indeed, if we introduce the difference ΔQ_s, between the reference reactive power (Q_{Sref}) and the estimated reactive power (Q_s) in a two-level hysteresis comparator (see Fig. 5), it generates at its output the value HC_q = +1 to increase the reactive power and HC_q = 0 to reduce it, this also allows obtaining a very good dynamic performance of the reactive power [34].

The choice of the voltage vector to apply depends on the sign of the error between the reference reactive power (Q_{Sref}) and the estimated flux reactive power.

The Control Panel is built according to the state of the variables HC_q and HC_p, and of the zone Ni of the position of Φ_s. It therefore, takes the following form [35] from Table 1.

Table 1

Traditional lookup table of DRAPC technique

N_i		1	2	3	4	5	6
HC_q	HC_p						
1	1	5	6	1	2	3	4
	0	7	0	7	0	7	0
	–1	3	4	5	6	1	2
0	1	6	1	2	3	4	5
	0	0	7	0	7	0	7
	–1	2	3	4	5	6	1

where: HC_q = 0 reduce the reactive power;
HC_q = 1 increased the reactive power;
HC_p = 1 increase the active power;
HC_p = 0 reduce the active power;
HC_p = –1 maintain the active power.

DRAPC with synergetic STA control. Direct reactive and active power control has been known to produce a fast response and strong strategy over the electrical generators used in the production of electric current using wind energy. However, there are undulations in active power, torque, reactive power, and current. There are several theories and modern strategies that have been used to minimizes the fluctuations that occur in both active and reactive powers. Among these methods, we find: backstepping control, neural networks, neuro-fuzzy control, synergetic control, sliding mode control, and fuzzy logic.

In this paper, a nonlinear DRAPC of ASG is presented based on an SYSTA controller. The variation of rotor and stator resistance due to changes DRAPC controller by introducing errors in the estimated flux linkage, reactive and active powers. The use of the SYSTA strategy minimizes the risks of a risk in the resistance value of the ASG, which leads to a decrease in the undulations.

The DRAPC with SYSTA controllers (SYSTA-DRAPC) is a modification of the classical DRAPC strategy, where the switching table and hysteresis

controllers, have been replaced by a space vector pulse width modulation (SVPWM) technique and SYSTA controllers as shown in Fig. 6. Both of them do not need advanced mathematical models. The DRAPC with SYSTA controller's goal is to control the active and reactive powers of the ASG. The active power is regulated by the quadrature axis voltage V_{qr}^{*}, while the reactive power is regulated by the direct axis voltage V_{dr}^{*}.

The sliding surfaces $S(x)$ representing the error between the measured and reference active and reactive powers are given by this relation:

$$S_q = Q_{Sref} - Q_s; \tag{28}$$

$$S_p = P_{Sref} - P_s. \tag{29}$$

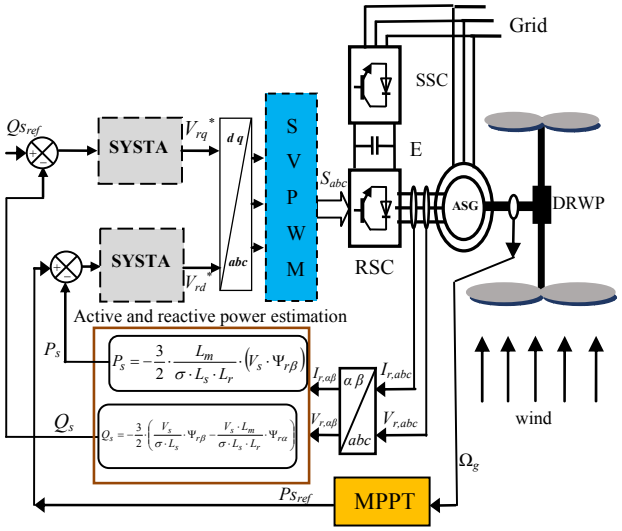

Fig. 6. DRAPC strategy with SYSTA controllers

Reactive and active power SYSTA controllers are used to influence respectively on the two rotor voltage components as in (30) and (31)

$$V_{qr}^{*} = \alpha_1 \cdot \sqrt{|S_p(t)|} \cdot sign(S_p(t)) + \\ + \alpha_2 \int sign(S_p(t)) + \alpha \frac{dS_p(t)}{dt} + S_p(t); \tag{30}$$

$$V_{dr}^{*} = \alpha_1 \cdot \sqrt{|S_q(t)|} \cdot sign(S_q(t)) + \\ + \alpha_2 \int sign(S_q(t)) + \alpha \frac{dS_q(t)}{dt} + S_q(t). \tag{31}$$

This proposed controller is implemented for a DRAPC technique based on the SYSTA controllers to obtain a minimum active power undulations and to minimize the chattering phenomenon. The controller structure for the SYSTA controllers for the reactive power and active power of the DRAPC technique are presented in Fig. 7 and Fig. 8, respectively.

Numerical simulations. The behavior of the structure of the proposed strategies, applied to a high power ASG (1.5 MW), is simulated under the Matlab / Simulink environment and the sampling time is 10^{-5} s. The simulation is performed under the following conditions:

The hysteresis band of the reactive power comparator is, in this case, fixed at ±0.05 VAR, and that of the active power comparator at ±0.001 W.

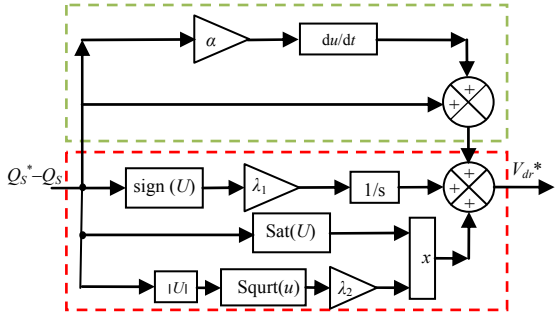

Fig. 7. SYSTA-reactive power controller

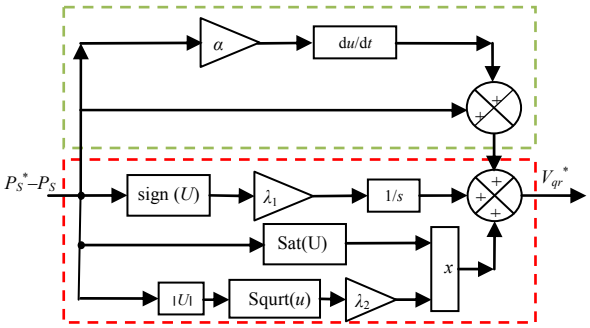

Fig. 8. SYSTA-active power controller

The ASG used in our study has the following parameters: two poles, 50 Hz, 380/696 V, P_{sn} = 1.5 MW, L_m = 0.0135 H, R_s = 0.012 Ω, J = 1000 kg·m^2, R_r = 0.021 Ω, L_s = 0.0137 H, L_r = 0.0136 H, and f_r = 0.0024 N·m/s [36].

A. First test. This first test is the reference tracking test and the results obtained are shown in Fig. 9-18. Figure 9 shows the torque of the proposed and classical strategies. It can be seen, that the amplitudes of the torque depend on the value of the load active power.

Figures 11, 12 represent the active and reactive powers of both strategies. The reactive and active powers track almost perfectly their reference values. Figure 10 shows the current of both DRAPC techniques. It, therefore, confirms that the amplitudes of the currents depend on the value of the load active power and the state of the drive system.

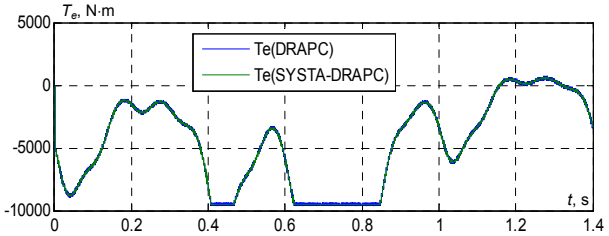

Fig. 9. Torque T_e

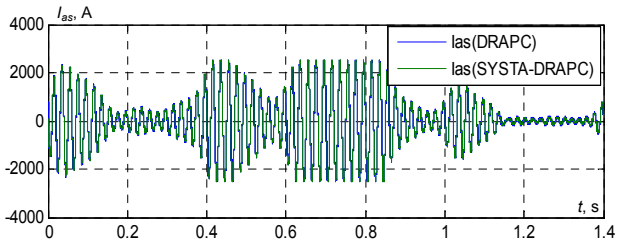

Fig. 10. Stator current I_{as}

The zoom in the current, torque, reactive power, and active power is shown in Fig. 13–16, respectively. It can be seen that the proposed strategy minimized the

undulations in current, torque, reactive power, and active power compared to the classical strategy.

Figures 17, 18 show the THD value of the current of both DRAPC strategies. It can be seen through these Figures that the THD value is reduced for the SYSTA-DRAPC (0.19 %) when compared to the classical DRAPC method (1.08 %). On the other hand, this designed strategy minimized the THD value of current compared to other strategies (see Table 2). Based on the results above, it can be said that the SYSTA-DRAPC strategy has proven its efficiency in minimizing undulations and chattering phenomena in addition to keeping the same advantages of the classical DRAPC strategy.

Table 2

Compare results with other methods

	Method Name	THD (%)
Ref. [37]	Field Oriented Control FOC	3.7
Ref.[38]	Direct Power Control DPC	4.88
	Virtual-Flux Direct Power Control VFDPC	4.19
Ref. [39]	Sliding Mode Control SMC	3.05
Ref. [40]	Second Order Continuous Sliding Mode – Direct Torque Control SOCSM-DTC	0.98
Proposed strategy	DRAPC	1.08
	SYSTA-DRAPC	0.19

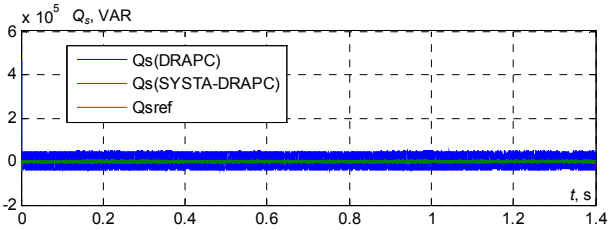

Fig. 11. Reactive power Q_s

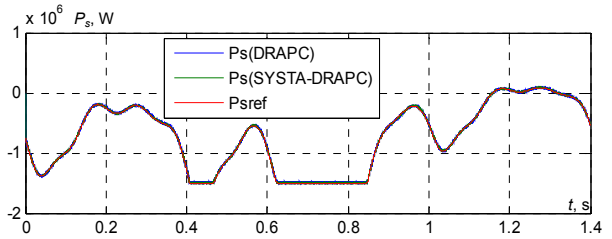

Fig. 12. Active power P_s

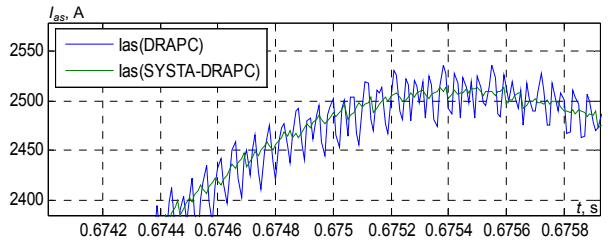

Fig. 13. Zoom of stator current I_{as}

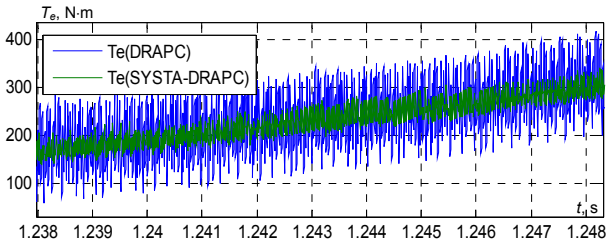

Fig. 14. Zoom of torque T_e

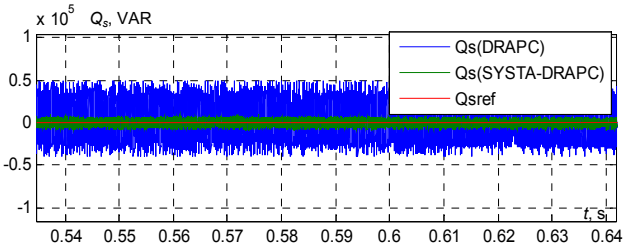

Fig. 15. Zoom of reactive power Q_s

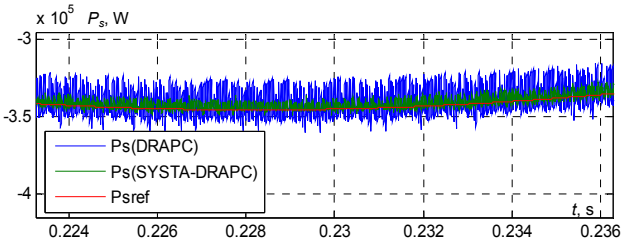

Fig. 16. Zoom of active power P_s

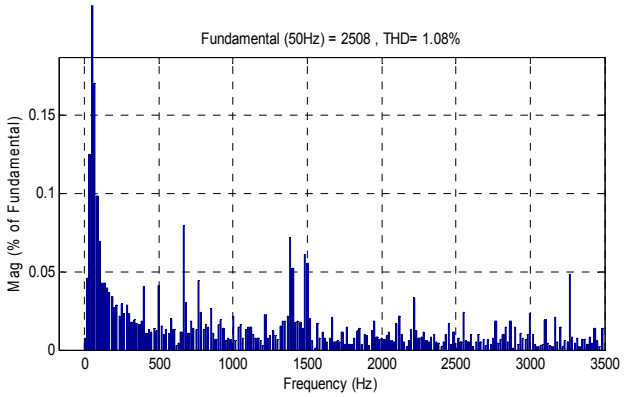

Fig. 17. THD of DRAPC method

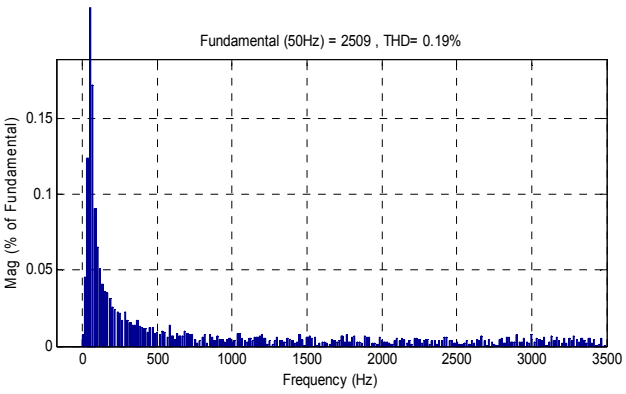

Fig. 18. THD of SYSTA-DRAPC method

B. Second test. In this test, we changed the values of both L_s, L_r, R_s, R_r and M, in order to find out which method is not affected by a change of parameters. The results obtained are shown in Fig. 19–24. Note that there is a change in reactive power, torque, active power, and current due to the fact that both torque and current are related to the changing values of parameters. On the other hand, the classical method was greatly affected by the change of parameters compared to the designed technique (Fig. 25–28), and this is evident in the value of THD (Fig. 19–20). Thus it can be concluded that the DRAPC with proposed SYSTA controllers is more robust than the traditional DRAPC technique.

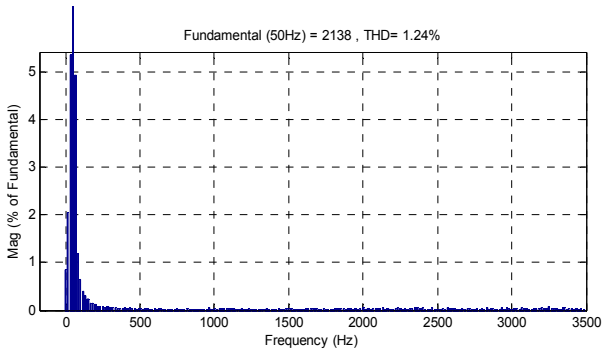

Fig. 19. THD of DRAPC method

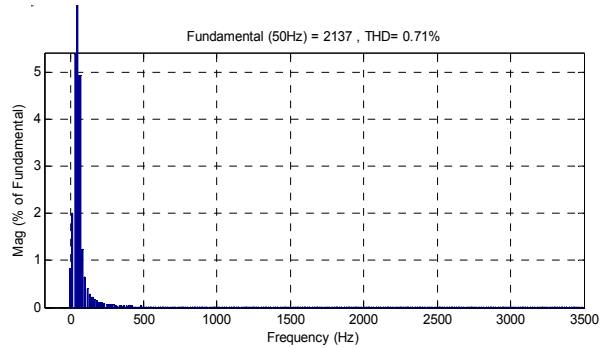

Fig. 20. THD of SYSTA-DRAPC method

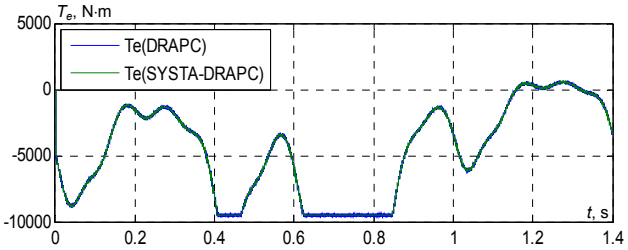

Fig. 21. Torque T_e

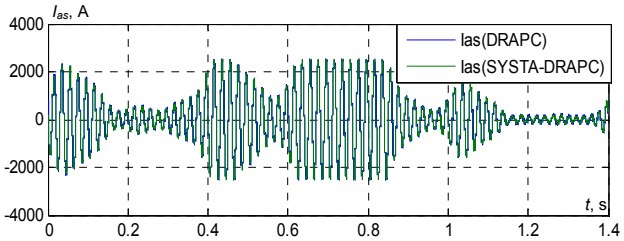

Fig. 22. Stator current I_{as}

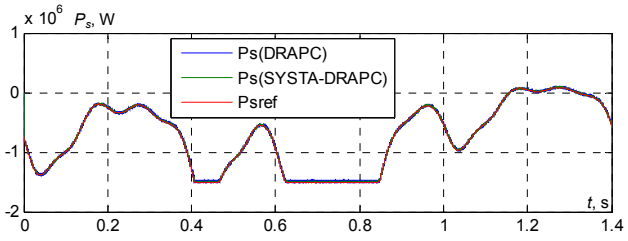

Fig. 23. Active power P_s

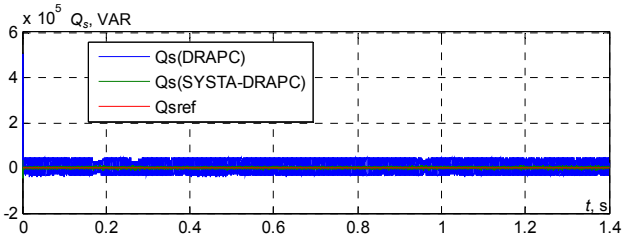

Fig. 24. Reactive power Q_s

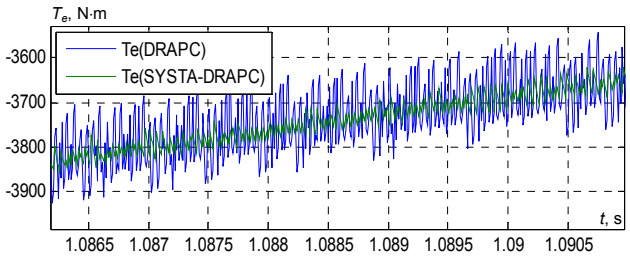

Fig. 25. Zoom of torque T_e

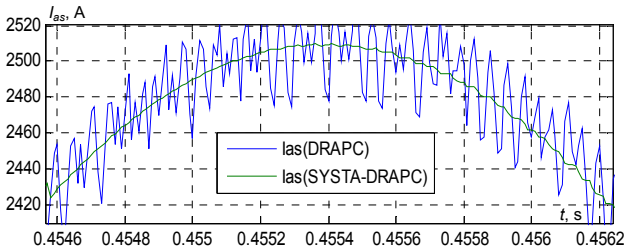

Fig. 26. Zoom of stator current I_{as}

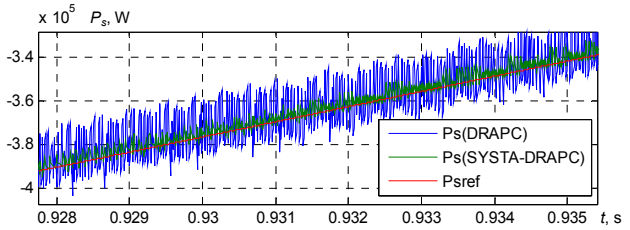

Fig. 27. Zoom of active power P_s

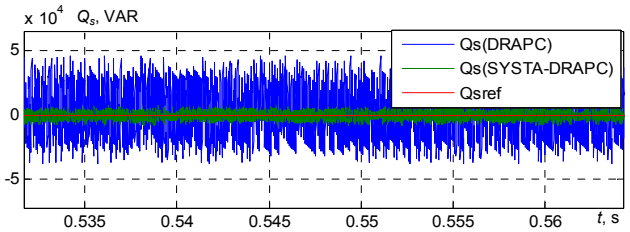

Fig. 28. Zoom of reactive power Q_s

Conclusions.

In this work, a novel nonlinear command theory for an asynchronous generator was designed based on a synergetic-super twisting algorithm. This command algorithm technique was employed to command the reactive and active powers of the asynchronous generator. The results indicated that the characteristics of the system had improved by using the synergetic-super twisting controllers and that this method could be applied to all electrical generators without exception. This is due to the results obtained. This designed method is easy to apply and does not require any effort, unlike other methods, where it requires mathematical calculations such as sliding mode control and backstepping command, and it is likely has a future in generating electrical energy using electric generators.

Conflict of interest. The authors declare that they have no conflicts of interest.

REFERENCES

1. Klimann A. H. R. The asynchronous generator: Mirage in electrical engineering. *Proceedings of the IEEE*, 1978, vol. 66, no. 8, pp. 986-986. doi: https://doi.org/10.1109/proc.1978.11064.

2. Benbouhenni H., Boudjema Z. Two-level DTC based on ANN controller of DFIG using 7-level hysteresis command to

reduce flux ripple comparing with traditional command. *2018 International Conference on Applied Smart Systems (ICASS)*, 2018, pp. 1-8. doi: https://doi.org/10.1109/icass.2018.8652013.

3. Hamed H. A., Abdou A. F., Moursi M. S. E., EL-Kholy E. E. A modified DPC switching technique based on optimal transition route for of 3L-NPC converters. *IEEE Transactions on Power Electronics*, 2018, vol. 33, no. 3, pp. 1902-1906. doi: https://doi.org/10.1109/tpel.2017.2743230.

4. Xiong P., Sun D. Backstepping-based DPC strategy of a wind turbine-driven DFIG under normal and harmonic grid voltage. *IEEE Transactions on Power Electronics*, 2016, vol. 31, no. 6, pp. 4216-4225. doi: https://doi.org/10.1109/tpel.2015.2477442.

5. Jayachandra B., Mahesh A. ANN based direct power control of 2-level PWM rectifier. *2018 International Conference on Power Energy, Environment and Intelligent Control (PEEIC)*, 2018, pp. 623-627. doi: https://doi.org/10.1109/peeic.2018.8665617.

6. Lamterkati J., Khaffalah M., Ouboubker L., El afia A. Fuzzy logic based improved direct power control of three-phase PWM rectifier. *2016 International Conference on Electrical and Information Technologies (ICEIT)*, 2016, pp. 125-130. doi: https://doi.org/10.1109/eitech.2016.7519575.

7. Benbouhenni H. Application of five-level NPC inverter in DPC-ANN of doubly fed induction generator for wind power generation systems. *International Journal of Smart Grid*, 2019, vol. 3, no. 3, pp. 128-137. Available at: https://www.ijsmartgrid.org/index.php/ijsmartgridnew/article/view/66/pdf (accessed 12 May 2020).

8. Amrane F., Chaiba A. A novel direct power control for grid-connected doubly fed induction generator based on hybrid artificial intelligent control with space vector modulation. *Revue Roumaine des sciences techniques. Série Électrotechnique et Énergétique*, 2016, vol. 61, no. 3, pp. 263-268. Available at: http://revue.elth.pub.ro/index.php?action=details&id=597 (accessed 12 May 2020).

9. Huang J., Zhang A., Zhang H., Ren Z., Wang J., Zhang L., Zhang C. Improved direct power control for rectifier based on fuzzy sliding mode. *IEEE Transactions on Control Systems Technology*, 2014, vol. 22, no. 3, pp. 1174-1180. doi: https://doi.org/10.1109/tcst.2013.2273368.

10. Heydari E., Rafiee M., Pichan M. Fuzzy-genetic algorithm-based direct power control strategy for DFIG. *Iranian Journal of Electrical and Electronic Engineering*, 2018, vol. 14, no. 4, pp. 353-361. doi: http://dx.doi.org/10.22068/IJEEE.14.4.353.

11. Benbouhenni H. Synergetic control theory scheme for asynchronous generator based dual-rotor wind power. *Journal of Electrical Engineering, Electronics, Control and Computer Science*, 2021, vol. 7, no. 3, pp. 19-28. Available at: https://jeeeccs.net/index.php/journal/article/view/215/173 (accessed 12 May 2020).

12. Yaichi I., Semmah A., Wira P., Djeriri Y. Super-twisting Sliding Mode Control of a Doubly-fed Induction Generator Based on the SVM Strategy. *Periodica Polytechnica Electrical Engineering and Computer Science*, 2019, vol. 63, no. 3, pp. 178-190. doi: https://doi.org/10.3311/PPee.13726.

13. Benbouhenni H. A comparative study between NSMC and NSOSMC strategy for a DFIG integrated into wind energy system. *Carpathian Journal of Electronic and Computer Engineering*, 2019, vol. 12, no. 1, pp. 1-8. doi: https://doi.org/10.2478/cjece-2019-0001.

14. Levant A. Higher-order sliding modes, differentiation and output-feedback control. *International Journal of Control*, 2003, vol. 76, no. 9-10, pp. 924-941. doi: https://doi.org/10.1080/0020717031000099029.

15. Benbouhenni H. A comparative study between DTC-NSTMC and DTC-FSTSMC control scheme for a DFIG-based wind turbine. *Majlesi Journal of Energy Management*, 2018, vol. 7, no. 4, pp. 43-53. Available at: http://journals.iaumajlesi.ac.ir/em/index/index.php/em/article/view/370 (accessed 12 May 2020).

16. Benbouhenni H., Boudjema Z., Belaidi A. DPC based on ANFIS super-twisting sliding mode algorithm of a doubly-fed induction generator for wind energy system. *Journal Européen des Systèmes Automatisés*, 2020, vol. 53, no. 1, pp. 69-80. doi: https://doi.org/10.18280/jesa.530109.

17. Benbouhenni H., Boudjema Z., Belaidi A. Direct power control with NSTSM algorithm for DFIG using SVPWM technique. *Iranian Journal of Electrical & Electronic Engineering*, 2021, vol. 17, no. 1, pp. 1-11. doi: http://dx.doi.org/10.22068/IJEEE.17.1.1518.

18. Listwan J. Application of super-twisting sliding mode controllers in direct field-oriented control system of six-phase induction motor: experimental studies. *Power Electronics and Drives*, 2018, vol. 3, no. 1, pp. 23-34. doi: https://doi.org/10.2478/pead-2018-0013.

19. Gonzalez T., J Moreno. A., Fridman L. Variable gain super-twisting sliding mode control. *IEEE Transactions on Automatic Control*, 2012, vol. 57, no. 8, pp. 2100-2105. doi: https://doi.org/10.1109/tac.2011.2179878.

20. Qian J., Li K., Wu H., Yang J., Li X. Synergetic control of grid-connected photovoltaic systems. *International Journal of Photoenergy*, 2017, vol. 2017, pp. 1-11. doi: https://doi.org/10.1155/2017/5051489.

21. Kondratiev I., Dougal R., Veselov G., Kolesnikov A. Hierarchical control for electromechanical systems based on synergetic control theory. *2009 IEEE Control Applications, (CCA) & Intelligent Control*, (ISIC), 2009, pp. 495-500. doi: https://doi.org/10.1109/cca.2009.5280959.

22. Benbouhenni H., Zinelaabidine B., Abdelkader B. Comparison study between neural STSM and ANFIS-STSM method in DPC control scheme of DFIG-based dual-rotor wind turbines. *International Journal of Energy and Environment*, 2020, vol. 14, pp. 33-46. doi: https://doi.org/10.46300/91012.2020.14.7.

23. Yahdou A., Hemici B., Boudjema Z. Second order sliding mode control of a dual-rotor wind turbine system by employing a matrix converter. *Journal of Electrical Engineering*, 2016, vol. 16, no. 3, pp. 89-99. Available at: http://jee.ro/articles/WO1439151618W55c7b6024978d.pdf (accessed 12 May 2020).

24. Yahdou A., Djilali A.B., Boudjema Z., Mehedi F. Improved vector control of a counter-rotating wind turbine system using adaptive backstepping sliding mode. *Journal Européen des Systèmes Automatisés*, 2020, vol. 53, no. 5, pp. 645-651. doi:https://doi.org/10.18280/jesa.530507.

25. Benbouhenni H. ANFIS-sliding mode control of a DFIG supplied by a two-level SVPWM technique for wind energy conversion system. *International Journal of Applied Power Engineering*, 2020, vol. 9, no. 1, pp. 36-47. doi: https://doi.org/10.11591/ijape.v9.i1.pp36-47.

26. Berkane S., Tayebi A. Construction of synergistic potential functions on SO(3) with application to velocity-free hybrid attitude stabilization. *IEEE Transactions on Automatic Control*, 2017, vol. 62, no. 1, pp. 495-501. doi: https://doi.org/10.1109/tac.2016.2560537.

27. Butt R. S., Ahmad I., Iftikhar R., Arsalan M. Integral backstepping and synergetic control for tracking of infected cells during early antiretroviral therapy. *IEEE Access*, 2019, vol. 7, pp. 69447-69455. doi: https://doi.org/10.1109/access.2019.2907201.

28. Prasad R., Padhy N. P. Synergistic frequency regulation control mechanism for DFIG wind turbines with optimal pitch dynamics. *IEEE Transactions on Power Systems*, 2020, vol. 35, no. 4, pp. 3181-3191. doi: https://doi.org/10.1109/tpwrs.2020.2967468.

29. Ettouil R., Chabir K., Abdelkrim M. N. Optimal synergetic control for wind turbine system. *The International Journal of Engineering and Science*, 2018, vol. 7, no. 5, pp. 44-48. doi: https://doi.org/10.9790/1813-0705014448.

30. Benbouhenni H. Rotor flux and torque ripples minimization for direct torque control of DFIG by NSTSM algorithm. *Majlesi Journal of Energy Management*, 2018, vol. 7, no. 3, pp. 1-9. Available at: http://journals.iaumajlesi.ac.ir/em/index/index.php/em/article/view/369 (accessed 12 May 2020).
31. Benbouhenni H. Twelve sectors DPC control based on neural hysteresis comparators of the DFIG integrated to wind power. *Tecnica Italiana-Italian Journal of Engineering Science*, 2020, vol. 64, no. 2-4, pp. 347-353. doi: https://doi.org/10.18280/ti-ijes.642-433.
32. Shah A. P., Mehta A. J. Direct power control of DFIG using super-twisting algorithm based on second-order sliding mode control. *2016 14th International Workshop on Variable Structure Systems (VSS)*, 2016, pp. 136-141. doi: https://doi.org/10.1109/vss.2016.7506905.
33. Malinowski M., Jasinski M., Kazmierkowski M. P. Simple direct power control of three-phase PWM rectifier using space-vector modulation (DPC-SVM). *IEEE Transactions on Industrial Electronics*, 2004, vol. 51, no. 2, pp. 447-454. doi: https://doi.org/10.1109/tie.2004.825278.
34. Benbouhenni H., Boudjema Z., Belaidi A. Power control of DFIG in WECS using DPC and NDPC-NPWM methods. *Mathematical Modelling of Engineering Problems*, 2020, vol. 7, no. 2, pp. 223-236. doi: https://doi.org/10.18280/mmep.070208.
35. Gong B., Wang K., Meng F., You J., Y Luo. A comparative study on switching tables of direct power control for voltage source rectifier. *2014 IEEE International Conference on Mechatronics and Automation*, 2014, pp. 1978-1983. doi: https://doi.org/10.1109/icma.2014.6886006.
36. Benbouhenni H. Sliding mode with neural network regulator for DFIG using two-level NPWM strategy. *Iranian Journal of Electrical & Electronic Engineering*, 2019, vol. 15, no. 3, pp. 411-419. doi: http://dx.doi.org/10.22068/IJEEE.15.3.411.
37. Amrane F., Chaiba A., Badr Eddine B., Saad M. Design and implementation of high performance field oriented control for grid-connected doubly fed induction generator via hysteresis rotor current controller. *Revue Roumaine des sciences techniques. Série Électrotechnique et Énergétique*, 2016, vol. 61, no. 4, pp. 319-324. Available at: http://revue.elth.pub.ro/index.php?action=details&id=609 (accessed 12 May 2020).
38. Yusoff N. A., Razali A. M., Karim K. A., Sutikno T., Jidin A. A concept of virtual-flux direct power control of three-phase AC-DC converter. *International Journal of Power Electronics and Drive System*, 2017, vol. 8, no. 4, pp. 1776-1784. doi: http://doi.org/10.11591/ijpeds.v8.i4.pp1776-1784.
39. Boudjema Z., Meroufel A., Djerriri Y., Bounadja E. Fuzzy sliding mode control of a doubly fed induction generator for energy conversion. *Carpathian Journal of Electronic and Computer Engineering*, 2013, vol. 6, no. 2, pp. 7-14. Available at: http://cjece.ubm.ro/vol/6-2013/202-6117.pdf (accessed 12 May 2020).
40. Boudjema Z., Taleb R., Djerriri Y., Yahdou A. A novel direct torque control using second order continuous sliding mode of a doubly fed induction generator for a wind energy conversion system. *Turkish Journal of Electrical Engineering & Computer Sciences*, 2017, vol. 25, no.2, pp. 965-975. doi: https://doi.org/10.3906/elk-1510-89.

Received 18.03.2021
Accepted 28.04.2021
Published 25.06.2021

Habib Benbouhenni[1]*, Doctor of Electrical Engineering,*
Soufiane Lemdani[2]*, Doctor of Electrical Engineering,*
[1] Department of Electrical & Electronics Engineering,
Nisantasi University, Istanbul, Turkey,
e-mail: habib.benbouenni@nisantasi.edu.tr (Corresponding author)
[2] Department of Electrical Engineering,
University of Science and Technology of Oran-Mohamed-Boudiaf, Oran, Algeria,
e-mail: lamdaniso@yahoo.fr

How to cite this article:
Benbouhenni H., Lemdani S. Combining synergetic control and super twisting algorithm to reduce the active power undulations of doubly fed induction generator for dual-rotor wind turbine system. *Electrical Engineering & Electromechanics*, 2021, no. 3, pp. 8-17. doi: https://doi.org/10.20998/2074-272X.2021.3.02.

UDC 621.3.07 https://doi.org/10.20998/2074-272X.2021.3.03

M.S. Mahgoun, A.E. Badoud

NEW DESIGN AND COMPARATIVE STUDY VIA TWO TECHNIQUES FOR WIND ENERGY CONVERSION SYSTEM

Introduction. *With the advancements in the variable speed direct drive design and control of wind energy systems, the efficiency and energy capture of these systems is also increasing. As such, numerous linear controllers have also been developed, in literature, for MPPT which use the linear characteristics of the wind turbine system. The major limitation in all of those linear controllers is that they use the linearized model and they cannot deal with the nonlinear dynamics of a system. However, real systems exhibit nonlinear dynamics and a nonlinear controller is required to handle such nonlinearities in real-world systems.* ***The novelty*** *of the proposed work consists in the development of a robust nonlinear controller to ensure maximum power point tracking by handling nonlinearities of a system and making it robust against changing environmental conditions.* ***Purpose.*** *In the beginning, sliding mode control has been considered as one of the most powerful control techniques, this is due to the simplicity of its implementation and robustness compared to uncertainties of the system and external disturbances. Unfortunately, this type of controller suffers from a major disadvantage, that is, the phenomenon of chattering.* ***Methods.*** *So in this paper and in order to eliminate this phenomenon, a novel non-linear control algorithm based on a synergetic controller is proposed. The objective of this control is to maximize the power extraction of a variable speed wind energy conversion system compared to sliding mode control by eliminating the phenomenon of chattering and have a good power quality by fixing the power coefficient at its maximum value and the Tip Speed Ratio maintained at its optimum value.* ***Results.*** *The performance of the proposed nonlinear controllers has been validated in MATLAB/Simulink environment. The simulation results show the effectiveness of the proposed scheme, suppression of the chattering phenomenon and robustness of the proposed controller compared to the sliding mode control law.* References 33, table 1, figures 17.
Key words: **synergetic controller, sliding mode controller, maximum power point tracking, macro-variable, wind energy conversion system.**

Вступ. *З досягненнями у проектуванні та керуванні вітряними енергосистемами з регульованою швидкістю, зростають також ефективність та захоплення енергії цих систем. Так, в літературі також розроблено численні лінійні контролери для відстеження точки максимальної потужності, які використовують лінійні характеристики системи з вітряними турбінами. Основним обмеженням у всіх цих лінійних контролерах є те, що вони використовують лінеаризовану модель і не можуть мати справу з нелінійною динамікою системи. Однак реальні системи демонструють нелінійну динаміку, і для обробки таких нелінійностей у реальних системах необхідний нелінійний контролер.* ***Новизна*** *запропонованої роботи полягає у розробці надійного нелінійного контролера для забезпечення відстеження точки максимальної потужності шляхом обробки нелінійності системи та забезпечення її стійкості до змін умов навколишнього середовища.* ***Мета.*** *Спочатку управління ковзним режимом вважалося одним з найпотужніших методів управління, що пов'язано з простотою його реалізації та надійністю порівняно з невизначеністю системи та зовнішніми збуреннями. На жаль, цей тип контролера страждає від головного недоліку, а саме явища вібрування.* ***Методи.*** *Тому у цій роботі з метою усунення цього явища пропонується новий нелінійний алгоритм управління, заснований на синергетичному контролері. Завдання цього контролю – максимізувати відбір потужності системи перетворення енергії вітру зі змінною швидкістю порівняно із регулюванням ковзного режиму, усуваючи явище вібрування, і мати хорошу якість енергії, фіксуючи коефіцієнт потужності на його максимальному значенні та підтримуючи кінцевий коефіцієнт швидкості на його оптимальному значенні.* ***Результати.*** *Ефективність запропонованих нелінійних контролерів перевірена в середовищі MATLAB/Simulink. Результати моделювання показують ефективність запропонованої схеми, придушення явища вібрування та стійкість запропонованого контролера порівняно із законом управління ковзного режиму.* Бібл. 33, табл. 1, рис. 17.
Ключові слова: **синергетичний контролер, контролер ковзного режиму, відстеження точки максимальної потужності, макрозмінна, система перетворення енергії вітру.**

1. Introduction. Nowadays, most countries of the world are facing difficulties in using conventional sources for power generation due to exhaustion of fossil fuels and environmental issues like air pollution and greenhouse gases. For these reasons, energy producers are heading to the use of renewable energy sources (sun, wind, biomass, etc) to produce electricity. These new energies appear today as a solution to energy production problems in the world [1, 2]. As a renewable energy source, wind energy is one of the most promising renewable energy resources for generating electricity due to its cost competitiveness compared to other conventional types of energy resources.

A wind energy conversion system (WECS) can be separated into three main conversion stages, including the transformation from the wind kinetic energy to the rotational mechanical energy in the wind turbine, the transformation from the turbine mechanical energy to the electrical energy by an electrical generator, and the connection between the electrical generator and the power grid by an electronic power converter [3]. The generated energy can be used either for standalone loads or fed into the power grid through an appropriate power electronic interface [4].

In WECS, several types of electric generators are used such as squired-cage induction generator, doubly fed induction generator [5]. Lately, with the advances of power electronic technology, permanent magnet synchronous generator based variable speed WECS are becoming more popular over other types of generators which are used in wind energy systems because of advantages such as its simple structure, ability of operation at low velocities, self-excitation capability leading to high power factor and high efficiency operation [6], moreover permanent magnet synchronous motor can be connected directly to the turbine without system of gearbox [7]. According to Betz's law, only 59.3 % of total available wind energy can be converted into mechanical energy considering no mechanical losses in the system [8]

and in most cases about 20-60 % of the Betz's limit can be obtained from wind turbines [9].

However, the conventional way to get the maximum power from wind is based on the optimum mathematical relationship. The turbine output power is a function of rotor speed if the wind speed is assumed to be constant. Thus controlling the rotor speed allows control over power production from the generator [10]. There are several other mathematical relationships suitable for maximum power tracking. In many cases electromagnetic torque vs. power relation is used to obtain the maximum power [11].

Basically, the studied maximum power point tracking (MPPT) methods for WECSs include three strategies:

1. Relying on wind speed measurement used by tip speed ratio (TSR) method;
2. Relying on wind turbine power curve used by power signal feedback and optimal torque control methods;
3. Relying on hill climb search of wind turbine power curve without any knowledge about this curve used by perturb and observe method [12].

Control design, in WECS is becoming a challenging task due to the nonlinear dynamics and uncertainties present in these systems [13]. The requirements of the control system include tracking a speed reference, generated by MPPT, by controlling the rotational speed in a variable speed wind turbine system [14, 15], while the most important part of the control design for nonlinear dynamical systems is to guarantee the stability.

Conventional control methods are based on proportional-integral (PI) regulators, which were initially developed for linear systems, and their design is limited by the parameters tuning, which is delicate and requires adjustment in a changing environment due to random variations of the power source [16]. Different model based control systems, such as sliding mode, known for its simplicity, speed and robustness was widely adopted and has shown its effectiveness in many applications.

Unfortunately, this type of controller suffers from a major disadvantage, that is, the phenomenon of chattering. The chattering phenomenon occurs due to implementation issues of the sliding mode control signal in digital devices operating with a finite sampling frequency, where the switching frequency of the control signal cannot be fully implemented [17].

In order to eliminate this phenomenon, a more recent technique (synergistic approach) is proposed in [18], the synergetic control method presents a suitable option to control nonlinear uncertain systems operating in disturbed environments. That's why several studies have been conducted in this field.

In this study, we adopted the tip speed ratio control strategy with a non-linear control algorithm based on a sliding mode theory and synergetic controller in order to maximize the power extraction of a variable speed of WECS. The main aspect of control design is definition of a macro-variable for synergetic control and sliding surface for sliding mode control.

In [19, 20] synergetic control is proposed as a nonlinear control technique to track photovoltaic systems and it is shown using simulation that synergetic control eliminates chattering effect compared to sliding mode control. The synergetic controller which has received much attention for photovoltaic systems can also be designed for WECS.

In our paper, the motivation is to use a nonlinear synergetic control of the wind speed turbine in order to operate at maximum power extraction. This new approach does not require the linearization of the model and explicitly uses a nonlinear model to design the control law.

The aim of paper is to optimize the power produced by a wind energy system under varying conditions based on two maximum power point tracking techniques.

The rest of the paper is organized as follows. The modeling of all parts of the wind speed turbine and problem formulation for MPPT to extract the maximum power are presented in Section 2. The synergetic and sliding mode control theory is summarized in Section 3, followed by the design of the synergetic controller and sliding mode. Simulation results and comparison with two well known controllers, sliding mode controller and synergetic controller, are presented in Section 4. Conclusion is given in Section 5.

2. Wind turbine modeling. WECS includes various multidisciplinary subsystems which can be classified as aerodynamic, structural and electrical. The aerodynamic subsystem represents the aerodynamic model of the wind turbine. The structural subsystems include blades, tower and drive train models. The electrical subsystems include the generator, the back-to-back converter and the system control models.

Model of wind turbine. The wind speed can be modelled as a deterministic sum of harmonics with frequency in range of 0.1–10 Hz as follows [21]:

$$V(t) = V_0\left(1 + \sum_{n=1}^{i} A_n \sin \omega_n t\right), \quad (1)$$

where V_0 is the average wind speed; A_n is the magnitude of n^{th} kind of eigenswing, ω_n is the eigenfrequency of n^{th} kind of eigenswing excited in the turbine rotating.

The aerodynamic (mechanical) power developed by a wind turbine is given by the following expression [22, 23]:

$$P_{aer} = \frac{1}{2} \cdot C_p(\lambda, \beta) \cdot \rho \cdot \pi \cdot R^2 \cdot V^3, \quad (2)$$

where ρ is the air density, kg/m^3; R is the radius of the turbine blade, m; V is the wind speed, m/s; $C_p(\lambda, \beta)$ is the power coefficient which is a function of both a factor λ known as the tip speed ratio (TSR) and blade pitch angle β (deg).

TSR is defined as the ratio of the turbine's blade-tip speed to the wind velocity, and can be expressed as:

$$\lambda = \frac{R \cdot \Omega_t}{V}, \quad (3)$$

where Ω_t is the rotor speed of a wind turbine, rad/s.

Several numerical expressions exist for $C_p(\lambda, \beta)$. Here the used relation is given by [24]:

$$C_p(\lambda, \beta) = (0.5 - 0.0167(\beta - 2)) \cdot \sin\left(\frac{\pi(\lambda + 0.1)}{18 - 0.3(\beta - 2)}\right) - 0.00184(\lambda - 3)(\beta - 2), \quad (4)$$

The C_p curve is shown in Fig. 1, from which there is an optimum λ at which the power coefficient C_p is maximal.

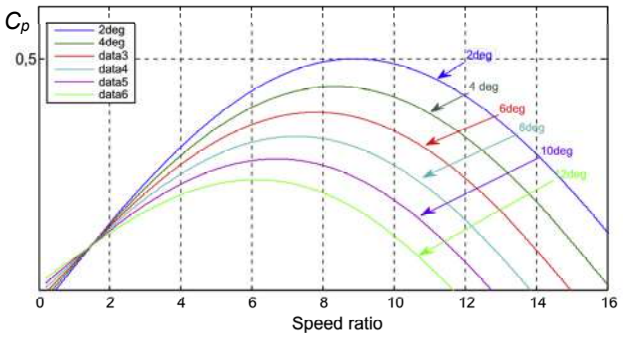

Fig. 1. Power coefficient $C_p(\lambda, \beta)$ versus tip-speed ratio for various values of β

The value of the power coefficient C_p is a function of λ and β, it reaches the maximum at the particular λ named λ_{opt}. Hence, to maximize the extracted energy of wind turbine λ should be maintained at λ_{opt} with the optimal rotor speed of the turbine which is determined from (3) and given as

$$\Omega_{ref} = \frac{\lambda_{opt} \cdot V}{R}, \tag{5}$$

where Ω_{ref} is the rotor speed reference, rad/s.

For a constant β Fig. 2 illustrates that there is only one fixed value of TSR (λ_{opt} = 9.14) for which C_p is maximum ($C_{p\max}$ = 0.5). This special value λ_{opt} is known as the optimal peak speed ratio, it can be expressed by:

$$\lambda_{opt} = \frac{\Omega_{ref} \cdot R}{V}. \tag{6}$$

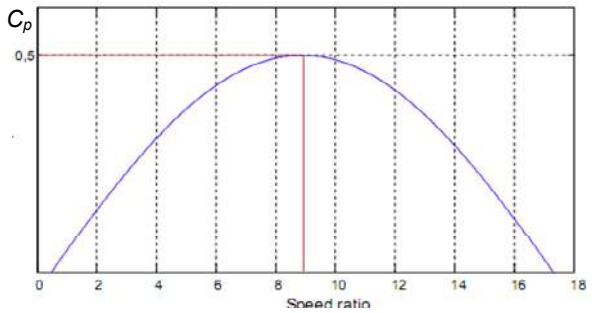

Fig. 2. Power coefficient C_p versus λ at fixed β

Gear box model. The role of gear box is to transform the mechanical speed of the turbine to the generating speed, and the aerodynamic torque to the gear box torque according to the following mathematical formulas [25]:

$$\begin{cases} T_g = T_{aer}/G; \\ \Omega_{tur} = \Omega/G; \\ T_{aer} = P_{aer}/\Omega_{tur}, \end{cases} \tag{7}$$

and the mechanical equation of the shaft, including both the turbine and the generator masses, is given by [24]:

$$J\frac{d\Omega}{dt} = T_g - T_{em} - f \cdot \Omega, \tag{8}$$

where Ω is the mechanical generator speed; Ω_{tur} is the speed of the turbine; T_g is the torque applied on the shaft of turbine; T_{aer} is the aerodynamic torque; P_{aer} is the aerodynamic power; T_{em} is the electromagnetic torque; J is the total moment of inertia; f is the viscous friction coefficient; G is the gear box ratio.

The system of equations (1)-(8) permit to us to construct the block diagram of the wind turbine as shown on Fig. 3 [32, 33].

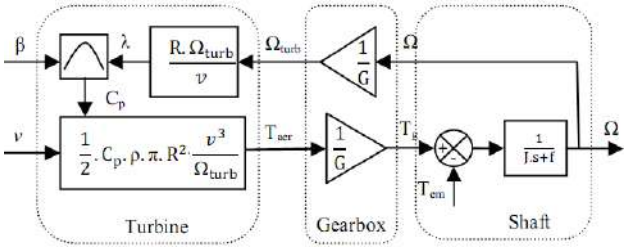

Fig. 3. Wind turbine block diagram.

3. MPPT control strategies. According to Fig. 1, for a particular value of tip speed ratio λ_{opt}, C_p has a unique maximum value at which maximum power is captured from wind by the wind turbine. As a result, to achieve power efficiency maximization, the turbine tip speed ratio must be sustained at its optimum value in spite of wind variations. Also, for a given wind velocity, there is an optimal value for rotor velocity which maximizes the power supplied by the wind. That is equally saying, the turbine system realizes the MPPT function [26]. Consequently, the system can operate at the peak of the $P(\Omega)$ curve, and the maximum power is extracted continuously from the wind. That is illustrated in Fig. 4.

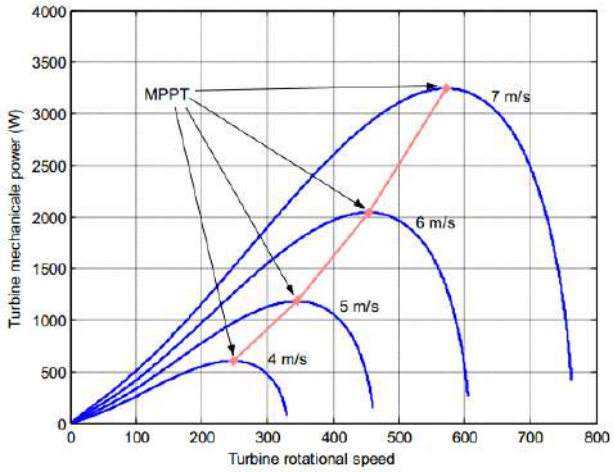

Fig. 4. Turbine powers various speed characteristics for different wind speeds with indication of the MPPT curve

So the MPPT technique consists of varying turbine speed constantly according to wind speed variations, so that the tip speed ratio is maintained in its optimum value, thus the power generation is optimum. In order to extract the maximum power from the wind, we adopted the speed turbine control strategy. It permits to carry the speed of the wind turbine into the desired value which corresponds to the maximum power point. The wind turbine speed control scheme is represented in Fig. 5, where C_Ω is the speed controller.

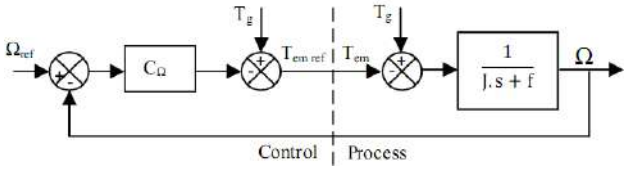

Fig. 5. Speed generator feedback control

This control structure consists to adjust the torque appearing on the turbine shaft in order to fix the turbine speed at a reference that permits to track of the maximum wind power. In this study, we assume that the electromagnetic torque equals to its reference all the time [24].

$$T_{em} = T_{em-ref} \cdot \quad (9)$$

Controller design based to sliding mode. Sliding mode control is one of the non-linear techniques. It is a particular operation mode of variable structure control systems. Its concept consists of moving the state trajectory of the system to a predetermined surface called sliding surface and maintaining it around this latter with an appropriate logic commutation [27]. The design of sliding mode controller is done in three steps [29, 30]:

1. Selection of the sliding surface;
2. Establishing the conditions of existence and convergence;
3. Determination of the control law.

The sliding surface is given by [31]:

$$S(x) = \left(\frac{d}{dt} + \lambda_{sm}\right)^{r-1} \cdot e(x), \quad (10)$$

where λ_{sm} is the positive constant indicating the desired control bandwidth; r is the relative degree, equal to the number of times to derive the output to appear the command; $e(x)$ is the error between the variable and its reference.

For $n = 1$ the error as being the sliding surface:

$$e(\Omega) = \Omega_{ref} - \Omega, \quad (11)$$

where Ω_{ref} is the desired speed.

This surface derivative is:

$$\dot{e}(\Omega) = \dot{\Omega}_{ref} - \dot{\Omega}. \quad (12)$$

Combining the previous equation with equation (8), we obtain:

$$\dot{e}(\Omega) = \dot{\Omega}_{ref} + \frac{1}{J}\left(-T_g + T_{em} + f \cdot \Omega\right), \quad (13)$$

The controller structure includes two parts, one part on the exact linearization and another said stabilizing [26-28], so:

$$T_{em} = T_{em}^{eq} + T_{em}^{n}. \quad (14)$$

Substituting the expression of the control speed by their expressions given in (13), the equations below are defined as follow:

$$\dot{e}(\Omega) = \dot{\Omega}_{ref} + \frac{1}{J}\left(-T_g + \left(T_{em}^{eq} + T_{em}^{n}\right) + f \cdot \Omega\right). \quad (15)$$

During the sliding mode and in permanent regime, we have:

$$e(\Omega) = 0; \quad \dot{e}(\Omega) = 0; \quad T_{em}^{n} = 0.$$

Where the equivalent control is:

$$T_{em}^{eq} = -J \cdot \dot{\Omega}_{ref} - f \cdot \Omega + T_g. \quad (16)$$

Therefore, the correction factor is given by:

$$T_{em}^{n} = -k \cdot \operatorname{sgn} e(\Omega), \quad (17)$$

where k is a positive constant.

The control expression:

$$T_{em} = -J \cdot \dot{\Omega}_{ref} - f \cdot \Omega + T_g - k \cdot \operatorname{sgn} e(\Omega). \quad (18)$$

Controller design based to synergetic control. Synergetic control is a state space approach for the design of control for complex highly connected nonlinear systems [20]. It forces the system state variables to evolve on a designer chosen invariant manifold enabling for desired performance to be achieved despite uncertainties and disturbances without damaging chattering inherent to the sliding mode technique [20]. Synergetic synthesis begins with the definition of the macro-variable based on the equations of the state space. For the macro-variable, it can be expressed as follows:

$$\psi = \psi(x, t). \quad (19)$$

The objective of the synergetic controller is to operate the controlled system on the manifold for which the macro-variable is null $\psi = 0$.

The expected dynamic evolution of the macro-variable is given as a function of:

$$T\dot{\psi} + \psi = 0, \quad T > 0. \quad (20)$$

where the derivative of the total macro-variable is noted by $\dot{\psi}$, and T is a parameter design which designates the convergence rate from the closed loop system to the manifold that is to be specified by $\psi = 0$.

Finally, the control law (evolution in time of the control output) is synthesized according to equation (14) and the dynamic model of the system.

According to synergetic controller, we will select the first set of macro-variables as equation (20):

$$\psi = \Omega_{ref} - \Omega. \quad (21)$$

This derivative is:

$$\dot{\psi} = \dot{\Omega}_{ref} - \dot{\Omega}. \quad (22)$$

Combining equations (8), (20), and (21), we get the electromagnetic torque as the following control law:

$$T_{em-ref} = T_{em} = \frac{J}{T}\left[\frac{T \cdot f}{J}\Omega - \frac{T \cdot T_g}{J} + \left(\Omega_{ref} - \Omega\right)\right]. \quad (23)$$

4. Simulation results. In this section we evaluate the performances and effectiveness of the control strategies by simulating the wind turbine under the turbulent wind speed profile of Fig. 6.

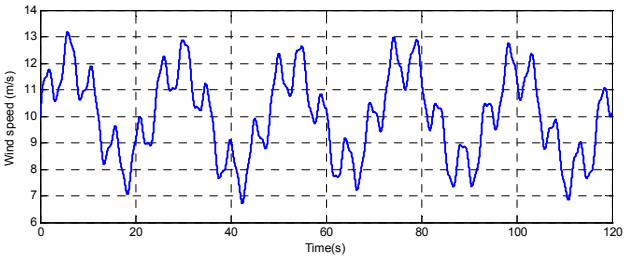

Fig. 6. Wind speed profile

The system parameters that have been chosen for the wind turbine are given in the Table 1.

Table 1

Wind turbine parameters

Parameters	Values
Density of air, kg/m^3	1.22
Radius of rotor, m	3
Gear box ratio	1
Turbine total inertia, kg·m^2	16
Total viscous friction coefficient, N·m/s	0.06

The sliding surface and power coefficient are shown in Fig. 7-9 respectively. For sliding mode controller, good tracking capability was observed but it is perturbed by the high-frequency oscillations (the chattering) which can cause instability and damage to the system and there are no oscillations around the $C_{p\max}$ for synergetic controller.

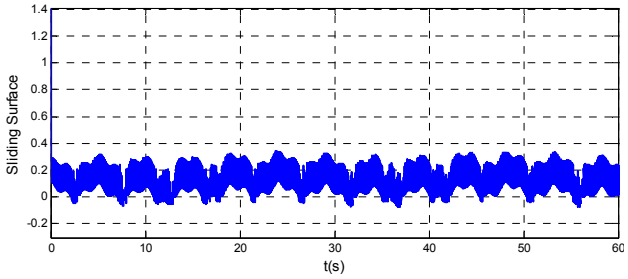

Fig. 7. Sliding surface

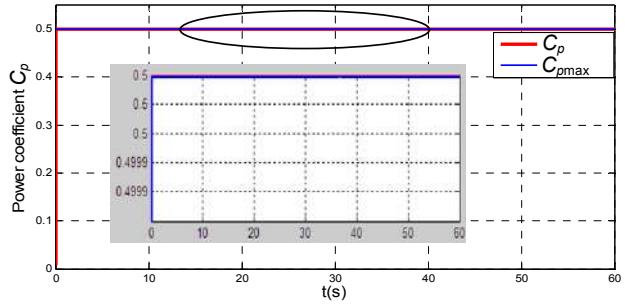

Fig. 8. Power coefficient using synergetic control

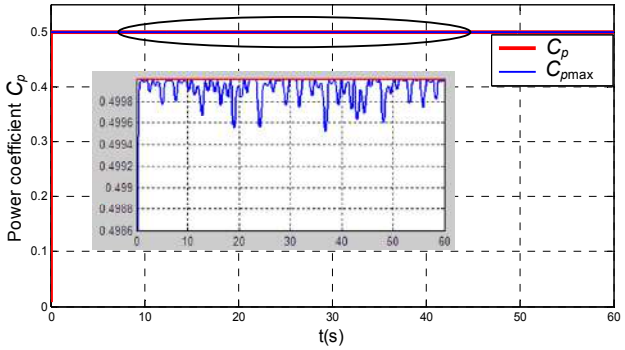

Fig. 9. Power coefficient using sliding mode

Figures 10, 11 show that the TSR follows its reference very well corresponding to the maximum and optimal value TSR λ_{opt} = 9.14 for both controllers, but with sliding mode controller the appearance of high chattering effect is always present.

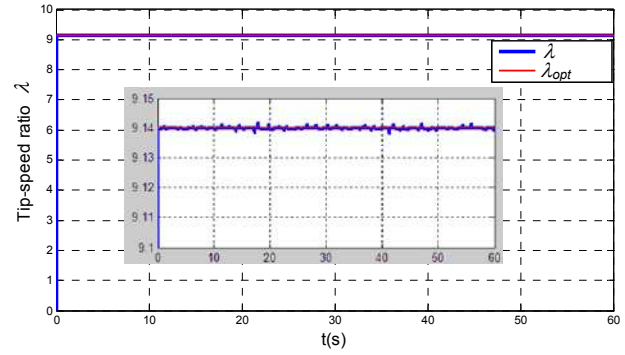

Fig. 10. Tip-speed ratio using synergetic control

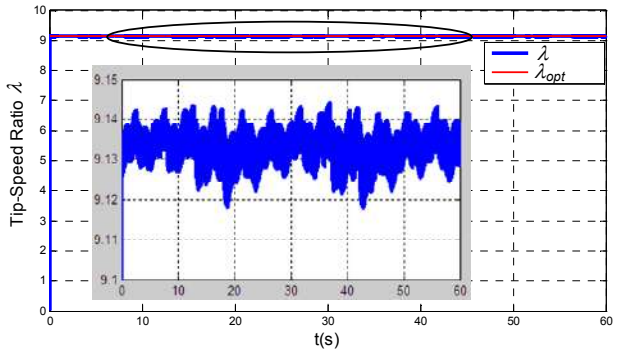

Fig. 11. Tip-speed ratio using sliding mode

According to Fig. 12, 13 the variation of the mechanical speed is adapted to the variation of the wind, which shows the direct influence of the wind on the speed of rotation of the shaft, we also note that the mechanical speed perfectly follows its reference value for the two controllers. But a zoom on these graphs shows that there is an error between the speed of rotation and its reference with the sliding mode controller. This confirms the effectiveness and good performance of the synergetic controller.

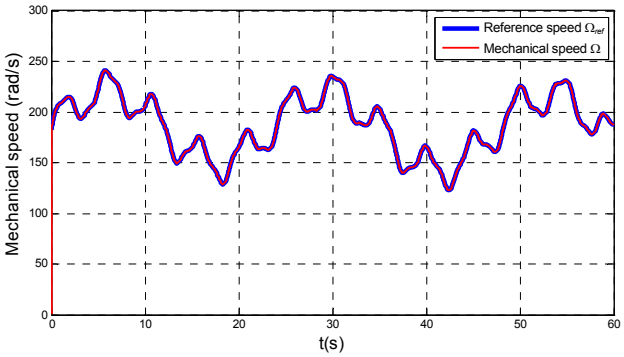

Fig. 12. Mechanical speed using synergetic control

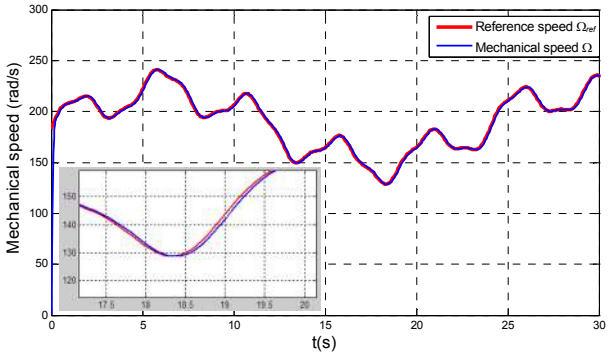

Fig. 13. Mechanical speed using sliding mode

Figures 14, 15 show the response of aerodynamic power. It is clear that the produced power follows well its optimal reference with good dynamics and track perfectly the reference for the two controllers, which means that the maximum power point can be achieved despite fast-varying wind velocity.

We can clearly see that in Fig. 16, 17 the macro-variable function and sliding mode surface equals zero, which shows that the controller parameters are properly chosen. But as we can see, Fig 16 the high chattering effect on the sliding surface.

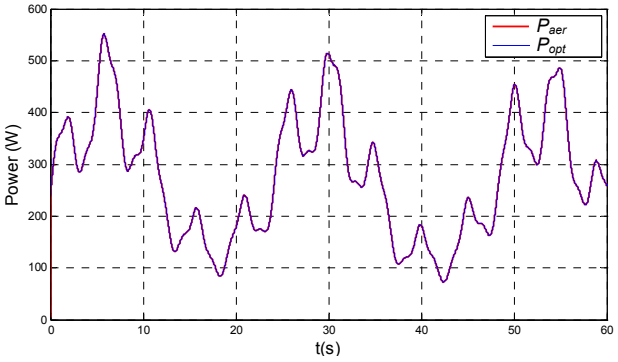

Fig. 14. Aerodynamic power using synergetic control

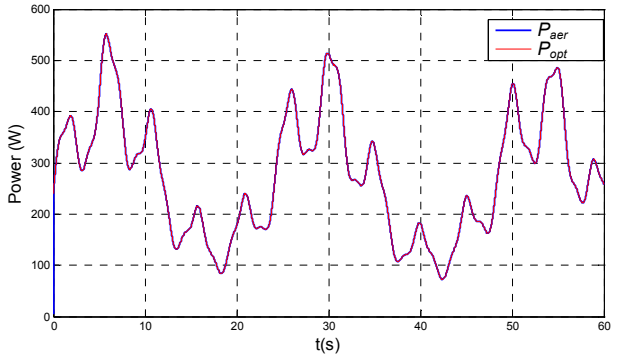

Fig. 15. Aerodynamic power using sliding mode

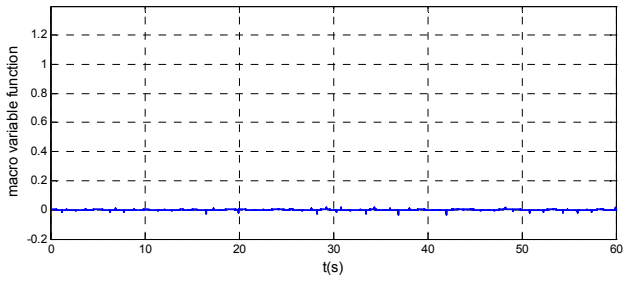

Fig. 16. Macro-variable function

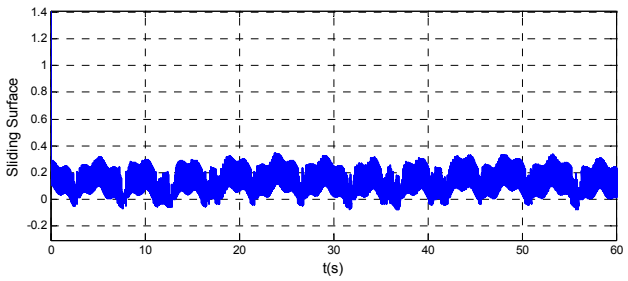

Fig. 17. Sliding surface function

From these results, we noticed that the MPPT controller based on synergetic is the most efficient technique compared to the sliding mode controller. It achieves maximum power with more stability, precision and better response time, and better trajectory tracking. However, the sliding mode method requires slow response time, with more oscillations and a chattering effect. For that, it can be stated that the synergetic control is a robust and efficient approach; it has better performance and a good dynamic response under variable wind speed conditions.

5. Conclusions.

In this paper, two maximum power point tracking strategies techniques are developed and compared to optimize the power produced by a wind energy system under varying conditions. According to the performance analysis of each method, it can be concluded that the maximum power point tracking controller based on synergetic control allows determining and tracking the maximum power point with more efficiency, fast response and high reliability compared to other controllers based on sliding mode. The main advantage of the synergetic controller, compared to the sliding mode, is the good reference tracking, the suppression of the chattering phenomenon and the reduction of the overshoot. The effectiveness and the robustness to external disturbances, noise and uncertainty parameters are shown in the simulation results.

Conflict of interest. The authors declare no conflict of interest.

REFERENCES

1. Jeong H., Lee K., Choi S., W. Choi. Performance improvement of LCL-filter-based grid-connected inverters using PQR power transformation. *IEEE Transactions on Power Electronics*, 2010, vol. 25, no. 5, pp. 1320-1330. doi: https://doi.org/10.1109/tpel.2009.2037225.

2. Lee J.-S., Jeong H.-G., Lee K.-B. Active damping for wind power systems with LCL filters using a DFT. *Journal of Power Electronics*, 2012, vol. 12, no. 2, pp. 326-332. doi: https://doi.org/10.6113/jpe.2012.12.2.326.

3. Bounar N., Labdai S., Boulkroune A., Farza M., M'Saad M. Adaptive fuzzy control scheme for variable-speed wind turbines based on a doubly-fed induction generator. *Iranian Journal of Science and Technology, Transactions of Electrical Engineering*, 2020, vol. 44, no. 2, 629-641. doi: https://doi.org/10.1007/s40998-019-00276-6.

4. Agarwal V., Aggarwal R.K., Patidar P., Patki C. A novel scheme for rapid tracking of maximum power point in wind energy generation systems. *IEEE Transactions on Energy Conversion*, 2010, vol. 25, no. 1, pp. 228-236. doi: https://doi.org/10.1109/tec.2009.2032613.

5. Rolan A., Luna A., Vazquez G., Aguilar D., Azevedo G. Modeling of a variable speed wind turbine with a permanent magnet synchronous generator. *2009 IEEE International Symposium on Industrial Electronics*, 2009, pp. 734-739. doi: https://doi.org/10.1109/isie.2009.5218120.

6. Chan T., Lai L.L. Permanent-magnet machines for distributed power generation: a review. *2007 IEEE Power Engineering Society General Meeting*, 2007, pp. 1-6. doi: https://doi.org/10.1109/PES.2007.385575.

7. Jlassi I., Estima J.O., Khojet El Khil S., Mrabet Bellaaj N., Marques Cardoso A.J. Multiple open-circuit faults diagnosis in back-to-back converters of PMSG drives for wind turbine systems. *IEEE Transactions on Power Electronics*, 2015, vol. 30, no. 5, pp. 2689-2702. doi: https://doi.org/10.1109/TPEL.2014.2342506.

8. Bouderbala M., Bossoufi B., Lagrioui A., Taoussi M., Aroussi H.A., Ihedrane Y. Direct and indirect vector control of a doubly fed induction generator based in a wind energy conversion system. *International Journal of Electrical and Computer Engineering*, 2019, vol. 9, no. 3, pp. 1531-1540. doi: https://doi.org/10.11591/ijece.v9i3.pp1531-1540.

9. He Q., Zhang F., Liu D., Gao C., Shi S., Xi P. Analysis on the development status and problems of China's offshore wind power. *2018 2nd IEEE Conference on Energy Internet and Energy System Integration (EI2)*, 2018, pp. 1-4. doi: https://doi.org/10.1109/EI2.2018.8582177.

10. Worku M.Y., Abido M.A. Maximum Power Control of DFIG Based Grid Connected Wind Turbine Generator System. *Renewable Energy and Power Quality Journal*, 2018, vol. 1, pp. 444-449. doi: https://doi.org/10.24084/repqj16.344.

11. Boukhezzar B., Lupu L., Siguerdidjane H., Hand M. Multivariable control strategy for variable speed, variable pitch

wind turbines. *Renewable Energy*, 2007, vol. 32, no. 8, pp. 1273-1287. doi: https://doi.org/10.1016/j.renene.2006.06.010.
12. Wang Q., Chang L. An intelligent maximum power extraction algorithm for inverter-based variable speed wind turbine systems. *IEEE Transactions on Power Electronics*, 2004, vol. 19, no. 5, pp. 1242-1249. doi: https://doi.org/10.1109/TPEL.2004.833459.
13. Toulabi M., Bahrami S., Ranjbar A.M. An Input-to-State Stability Approach to Inertial Frequency Response Analysis of Doubly-Fed Induction Generator-Based Wind Turbines. *IEEE Transactions on Energy Conversion*, 2017, vol. 32, no. 4, pp. 1418-1431. doi: https://doi.org/10.1109/TEC.2017.2696510.
14. Kumar D., Chatterjee K. A review of conventional and advanced MPPT algorithms for wind energy systems. *Renewable and Sustainable Energy Reviews*, 2016, vol. 55, pp. 957-970. doi: https://doi.org/10.1016/j.rser.2015.11.013.
15. Lee S.-W., Chun K.-H. Adaptive Sliding Mode Control for PMSG Wind Turbine Systems. *Energies*, 2019, vol. 12, no. 4, p. 595. doi: https://doi.org/10.3390/en12040595.
16. Li S., Haskew T.A., Xu L. Conventional and novel control designs for direct driven PMSG wind turbines. *Electric Power Systems Research*, 2010, vol. 80, no. 3, pp. 328-338. doi: https://doi.org/10.1016/j.epsr.2009.09.016.
17. Pratap B., Singh N., Kumar V. Robust Control of Variable Speed Wind Turbine Using Quasi-Sliding Mode Approach. *Procedia Computer Science*, 2018, vol. 125, pp. 398-404. doi: https://doi.org/10.1016/j.procs.2017.12.052.
18. Kolesnikov A., Veselov G., Kolesnikov A. *Modern applied control theory: synergetic approach in control theory*. Moscow-Taganrog, TRTU Publ., 2000.
19. Attoui H., Khaber F., Melhaoui M., Kassmi K., Essounbouli N. Development and experimentation of a new MPPT synergetic control for photovoltaic systems. *Journal of Optoelectronics and Advanced Materials*, 2016, vol. 18, no. 1-2, pp. 165-173. Available at: https://joam.inoe.ro/articles/development-and-experimentation-of-a-new-mppt-synergetic-control-for-photovoltaic-systems/ (accessed 21 May 2020).
20. Akoro E., Tevi G.J., Faye M.E., Doumbia M.L., Maiga A.S. Artificial Neural Network Photovoltaic Generator Maximum Power Point Tracking Method using Synergetic Control Algorithm. *International Journal on Emerging Technologies*, 2020, vol. 11, no. 2, pp. 590-594. Available at: https://www.researchtrend.net/ijet/pdf/Artificial%20Neural%20Network%20Photovoltaic%20Generator%20Maximum%20Power%20Point%20Tracking%20Method%20using%20Synergetic%20Control%20Algorithm%20Edjadessamam%20AKORO%201893n7.pdf (accessed 21 May 2020).
21. Ounnas D., Ramdani M., Chenikher S., Bouktir T. Optimal Reference Model Based Fuzzy Tracking Control for Wind Energy Conversion System. *International Journal of Renewable Energy Research*, 2016, vol. 6, no. 3, pp. 1129-1136. Available at: https://www.ijrer.org/ijrer/index.php/ijrer/article/view/4258/pdf (accessed 21 May 2020).
22. Aissou R., Rekioua T., Rekioua D., Tounzi A. Nonlinear predictive control of a permanent magnet synchronous generator used in wind energy. *Journal of Electrical Engineering*, 2014, vol. 14, no. 4, pp. 331-336. Available at: http://jee.ro/articles/WN1397935592W5352cde8e8fe5.pdf (accessed 21 May 2020).
23. Daghigh A., Javadi H., Torkaman H. Considering wind speed characteristics in the design of a coreless AFPM synchronous generator. *International Journal of Renewable Energy Research*, 2016, vol. 6, no. 1, pp. 263-270. Available at: https://www.ijrer.org/ijrer/index.php/ijrer/article/view/3135/pdf (accessed 21 May 2020).
24. Watson S., Moro A., Reis V., Baniotopoulos C., Barth S., Bartoli G., Bauer F., Boelman E., Bosse D., Cherubini A., Croce A., Fagiano L., Fontana M., Gambier A., Gkoumas K., Golightly C., Latour M.I., Jamieson P., Kaldellis J., Macdonald A., Murphy J., Muskulus M., Petrini F., Pigolotti L., Rasmussen F., Schild P., Schmehl R., Stavridou N., Tande J., Taylor N., Telsnig T., Wiser R. Future emerging technologies in the wind power sector: A European perspective. *Renewable and Sustainable Energy Reviews*, 2019, vol. 113, art. no. 109270. doi: https://doi.org/10.1016/j.rser.2019.109270.
25. Messaoud M., Abdessamed R. Modeling and optimization of wind turbine driving permanent magnet synchronous generator. *Jordan Journal of Mechanical and Industrial Engineering*, 2011, vol. 5, no. 6. Available at: http://jjmie.hu.edu.jo/files/v5n6/JJMIE%20-77-10.pdf (accessed 21 May 2020).
26. Errami Y., Ouassaid M., Maaroufi M. A performance comparison of a nonlinear and a linear control for grid connected PMSG wind energy conversion system. *International Journal of Electrical Power & Energy Systems*, 2015, vol. 68, pp. 180-194. doi: https://doi.org/10.1016/j.ijepes.2014.12.027.
27. Bennassar A., Banerjee S., Jamma M., Essalmi A., Akherraz M. Real time high performance of sliding mode controlled induction motor drives. *Procedia Computer Science*, 2018, vol. 132, pp. 971-982. doi: https://doi.org/10.1016/j.procs.2018.05.113.
28. Evangelista C., Valenciaga F., Puleston P. Active and reactive power control for wind turbine based on a MIMO 2-sliding mode algorithm with variable gains. *IEEE Transactions on Energy Conversion*, 2013, vol. 28, no. 3, pp. 682-689. doi: https://doi.org/10.1109/TEC.2013.2272244.
29. Krim Y., Abbes D., Krim S., Faouzi Mimouni M. Power management and second-order sliding mode control for standalone hybrid wind energy with battery energy storage system. *Proceedings of the Institution of Mechanical Engineers, Part I: Journal of Systems and Control Engineering*, 2018, vol. 232, no. 10, pp. 1389-1411. doi: https://doi.org/10.1177/0959651818784320.
30. Meng Z., Shao W., Tang J., Zhou H. Sliding-mode control based on index control law for MPPT in photovoltaic systems. *CES Transactions on Electrical Machines and Systems*, 2018, vol. 2, no. 3, pp. 303-311. doi: https://doi.org/10.30941/CESTEMS.2018.00038.
31. Chavira F., Ortega-Cisneros S., Rivera J. A novel sliding mode control scheme for a PMSG-based variable speed wind energy conversion system. *Energies*, 2017, vol. 10, no. 10, art. no. 1476. doi: https://doi.org/10.3390/en10101476.
32. Levron Y., Shmilovitz D. Maximum power point tracking employing sliding mode control. *IEEE Transactions on Circuits and Systems I: Regular Papers*, 2013, vol. 60, no. 3, pp. 724-732. doi: https://doi.org/10.1109/TCSI.2012.2215760.
33. Rajendran S., Jena D. Backstepping sliding mode control for variable speed wind turbine. *2014 Annual IEEE India Conference (INDICON)*, 2014, pp. 1-6. doi: https://doi.org/10.1109/INDICON.2014.7030634.

Received 14.04.2021
Accepted 24.05.2021
Published 25.06.2021

Mohamed Seddik Mahgoun [1], *PhD Student of Electrical Engineering,*
Abd Essalam Badoud [1], *Associate Professor,*
[1] Automatic Laboratory of Setif,
Electrical Engineering Department,
University Ferhat Abbas Setif 1,
Setif, Algeria.
e-mail: mahgounm@yahoo.fr,
badoudabde@univ-setif.dz (Corresponding author)

How to cite this article:
Mahgoun M.S., Badoud A.E. New design and comparative study via two techniques for wind energy conversion system. *Electrical Engineering & Electromechanics*, 2021, no. 3, pp. 18-24. doi: https://doi.org/10.20998/2074-272X.2021.3.03.

UDC 681.513, 621.365, 62-83-52 https://doi.org/10.20998/2074-272X.2021.3.04

Ya.S. Paranchuk, Y.V. Shabatura, O.O. Kuznyetsov

ELECTROMECHANICAL GUIDANCE SYSTEM BASED ON A FUZZY PROPORTIONAL-PLUS-DIFFERENTIAL POSITION CONTROLLER

Purpose. *The purpose is to develop solutions for the implementation of optimal laws of arms positioning, overshoot-free and requiring no post-adjustments.* ***Method****. The control model is based on the fuzzy set theory; and the structural modeling methodology is used to study the dynamics indices.* ***Results.*** *The structural scheme of the positional electromechanical system with a fuzzy proportional-plus-differential position controller and the method of control adaptation to the position reference signal change are obtained.* ***Scientific novelty****. A model of a fuzzy proportional-differential controller signal adaptation in the structure of a positional electromechanical system is proposed.* ***Practical value****. A solution is obtained for the implementation of optimal guidance process, non-overshooting and requiring no post-adjustments, also featuring the maximum weapons speed and minimal sensitivity to parametric disturbances*. References 20, tables 1, figures 12.
Key words: **fuzzy controller, positioning, adaptation, overshoot, speed.**

Запропоновано позиційну електромеханічну систему наведення озброєння на основі адаптивного нечіткого пропорційно-диференційного (ПД) регулятора положення. Створено структурну Simulink-модель системи позиціонування озброєння основі нечіткої адаптивної моделі керування. Проведено комп'ютерні дослідження динаміки процесів позиціонування при використанні пропорційного та запропонованого адаптивного нечіткого ПД регулятора положення. Результати досліджень показали, що при використанні нечіткої адаптивної моделі керування процесом позиціонування реалізуються оптимальні без перерегулювання та режимів дотягування закони руху озброєння. Бібл. 20, табл. 1, рис. 12.
Ключові слова: **нечіткий регулятор, позиціонування, адаптація, перерегулювання, швидкодія.**

Предложено позиционную электромеханическую систему наведения вооружения на основе адаптивного нечеткого пропорционально-дифференциального (ПД) регулятора положения. Разработано структурную Simulink-модель системы наведения вооружения на основе нечеткой адаптивной модели управления. Проведены компьютерные исследования динамики процессов позиционирования при использовании пропорционального и предложенного адаптивного нечеткого ПД регулятора положения. Результаты исследований показали, что при использовании нечеткой адаптивной модели управления процессом позиционирования реализуются оптимальные без перерегулирования и режимов дотягивания законы движения вооружения. Библ. 20, табл. 1, рис. 12.
Ключевые слова: **нечеткий регулятор, позиционирование, адаптация, перерегулирование, быстродействие.**

Introduction. At the present stage of development of armaments of missile troops and artillery, there is a tendency to increase the range, increase mobility and accuracy of weapons. This trend is realized both in the creation of new high-precision means of destruction, and in the process of modernization of existing ones.

Samples of these weapons, which were created and manufactured in the 70-80s of last century, do not fully meet modern requirements for accuracy and speed of guidance. The reason for this is the imperfect element base, system and circuitry of control systems of the specified time period, which today is mostly morally obsolete and physically worn out.

In view of this, it can be argued about the relevance and feasibility of directing efforts and finances to the modernization of these models of missile technology in the direction of improving their tactical and technical characteristics [1, 2].

Problem definition. Mentioned models of missile weapons include, for example, rocket-propelled grenade launchers based on the BM-21 combat vehicle, or others. The process of guiding the package of guides (PGs) in azimuth and pitch in these machines is implemented by manual drive or non-positional electromechanical system (EMS) according to the scheme «electromechanical amplifier – DC motor» using the appropriate forming and stabilizing feedbacks [2].

This EMS contains backlash, elasticity, in particular a pair of torsions, gaps and other nonlinearities. It is characterized by the inconsistency of the moment of inertia and load at different loads of PGs by missiles, as well as asymmetry of the load at different directions of movement. These factors negatively affect the dynamics and statics of the process of positioning PGs in the guidance process.

Control of the movement of the guide package (the process of guidance, positioning) in both planes in the existing EMS is performed manually from the remote control. There is no position adjustment circuit. In such a control system, the efficiency and accuracy of weapons guidance is significantly influenced by a subjective factor – the qualification of the operator (gunner). To eliminate this factor, it is advisable to automate the process of positioning the PGs by using a high-precision sensor and the setter of the aiming angle and the implementation of automatic angle adjustment by the mismatch signal. This approach eliminates the influence of the subjective factor and guarantees the predicted indicators of the dynamics and statics of the process of weapons guidance, in particular the static positioning accuracy.

Analysis of recent research and publications. It is known that positional electric drives are able to implement the desired laws and trajectories of the actuators as well as the quality of static accuracy and speed of positioning. Therefore, the task of obtaining the highest control speed in the absence of overregulation and traction modes at «creeping» speeds and the required static positioning accuracy can be considered relevant and important in the modernization and optimization of

electromechanical guidance systems in azimuth and pitch of the BM-21 combat vehicle [3, 4].

An effective system approach to solve this problem is the implementation of an electromechanical control system of the PG movement according to the scheme «pulse-width converter – DC motor» (PWC-DCM) according to the subordinate control principle using internal control circuits of current (torque) and speed of the motor and their standard setting for the modular optimum and additionally introduced external position control circuit [5, 6].

The classic approach in the construction of positional automatic control systems (ACS) is the use of proportional (P) position controller (PC) [3-7]. This structure of the ACS makes it possible to obtain the desired indicators of the dynamics of positioning in the modes of large displacements in the implementation of the trapezoidal tachogram of the electric drive movement.

But when working out tasks for smaller movements, which are performed at lower speeds, the positioning processes are accompanied by traction modes, the duration of which is commensurate with the braking time when working out large movements [8]. To eliminate these modes, a parabolic PC is used, which is most often included in the control circuit of the three-circuit control system with internal control circuits of current and speed with proportional-integral (PI) and P regulators, respectively, and their standard settings [8].

The predicted dynamics of the positioning process in the above structures is achieved under the condition of constant load torque, initial position, moment of inertia and other parameters. If these conditions are not met, the dynamics of the actuator movement will deviate from the optimal, which corresponds to the selected structure of the ACS and the principle of adjusting the coordinate controllers.

To eliminate the negative impact on the optimal laws of motion of the above coordinate and parametric perturbations in modern control models and with incomplete information about the state of the control object, intelligent approaches based, in particular, on fuzzy logic algorithms are used [9-13]. Such control models are used in positional ACS, including for tasks of optimization and adaptation of control in the modes of positioning and tracking in the conditions of action of coordinate and parametric perturbations.

It is known that classical proportional-differential (PD) regulators are well distinguished by their properties of improving the quality of transients, in particular in positioning systems in positioning and tracking modes. In [13-15] it is shown that fuzzy PD regulators and fuzzy proportional-integral-differential (PID) regulators provide a significant improvement in the quality of system dynamics, in particular positional, compared to the use of classical PID regulators and especially in cases where in the control object there are various kinds of nonlinearities and parametric uncertainties.

The main advantage and feature of fuzzy control is the possibility of its effective use in systems with complex mathematical descriptions and parametric and coordinate fluctuations, existing uncertainties, elasticities, nonlinearities, backlashes, gaps, etc.

In addition, as shown in [14-18], the advantages of fuzzy controllers are their simplicity, as well as low sensitivity to parametric changes and uncertainties in the control object due to the mechanism of rapid information processing based on fuzzy inference models. These features are inherent in the mechanism of weapons guidance of the BM-21. This further argues for the feasibility of using fuzzy control models to improve the dynamics and statics of the processes of positioning PGs.

The goal of the paper is to develop the structure and study the effectiveness of using an adaptive fuzzy PD position regulator to improve the accuracy and efficiency of weapons guidance by implementing the optimal laws of PG movement on the full range of position control in the structure of positional three-circuit EMS for guidance of the PGs of the combat vehicle during its modernization.

Therefore, the task of developing system solutions to implement the exact positioning of the PGs of the BM-21 without over-regulation and modes of tightening under the conditions of these perturbations and parametric changes for the system of vertical guidance of the PGs is relevant and important.

At the present stage of EMS development there is a tendency of wide application for the problems of automatic coordinate control and optimal control of modes of methods of the theory of artificial intelligence, the components of which is a transformation of typical proportional-integral, proportional-differential and proportional-integral-differential control laws on their fuzzy or neurofuzzy versions [13-20].

The object of control of the considered EMS is the mechanism of vertical guidance of the PGs which belongs to the class of complex systems, because it contains nonlinear elements, uncertainties, mechanical links with backlash, delay, limited stiffness, the parameters of which are also not constant and change in the process of guidance and depend on the level of missile loading of the PGs and other factors. In view of this, we use a fuzzy version of the proportional-differential PC for the position control circuit of the EMS under consideration, which a priori gives the position control circuit adaptive properties that are invariant to the action of parametric perturbations. In other words, the use of fuzzy PD position regulator should ensure the implementation of the desired optimal without overregulation and modes of traction at maximum speed of the laws of motion of the PGs in the full range of position regulation in the space of real parametric changes and coordinate perturbations.

For this purpose, we use the general structure of the fuzzy controller (FC), on the basis of which we can get different versions of fuzzy proportional-differential regulators of direct action. As the input signals of FC we take the error of adjusting the aiming angle $e(t) = \varphi_{ref}(t) - \varphi(t)$ and its derivative $de(t)/dt \cong (e(t_i) - e(t_{i-1})) / (t_i - t_{i-1})$ – the rate of error change. Given the fact that currently these regulators in the structures of the ACS are implemented on a digital element base (microcontrollers), its mathematical model is presented in discrete form. In this approach, the error signal derivative at the input of the FC is fed in finite increments.

The mathematical model of the classical analog PD regulator is presented by the following equation:

$$u(t) = k_r[e(t) + T_d \cdot de(t)/dt], \quad (1)$$

where $e(t)$, $u(t)$ are the input and output signals, k_r, T_d are the transmission ratio and differentiation constant of the PD regulator, respectively.

The transition in (1) to discrete time makes it possible to obtain a mathematical model of the PD controller for its digital implementation:

$$u(k) = k_r\left[\frac{T_d}{T_0}\cdot\Delta e(k) + e(k)\right], \quad (2)$$

where T_0 is the time quantization interval; k = 1,2,3,… is the discretization step number in time; $\Delta e(k) = e(k) - e(k-1)$.

The main requirement for positional EMS of the guidance of the PGs for a given angle φ_{ref} is the implementation of optimal laws of motion of guides in the positioning process (without overregulation and tightening modes) at maximum speed on the full range of position regulation under real coordinate and parametric perturbations.

The values of the maximum speed, acceleration and voltage of the PWC in the proposed positional EMS of the guidance of the PGs are taken the same as in the real existing system of providing movement of the PGs of the BM-21 combat vehicle.

The structure of positional EMS. The block diagram of the proposed three-circuit positional EMS for guidance of the PGs of the BM-21 combat vehicle with adaptive fuzzy PD position regulator is shown in Fig. 1. The electric drive of such EMS is realized according to the reversible scheme of PWC-DCM. The regulator of the internal circuit of the current is proportional-integral, and of the speed circuit is proportional.

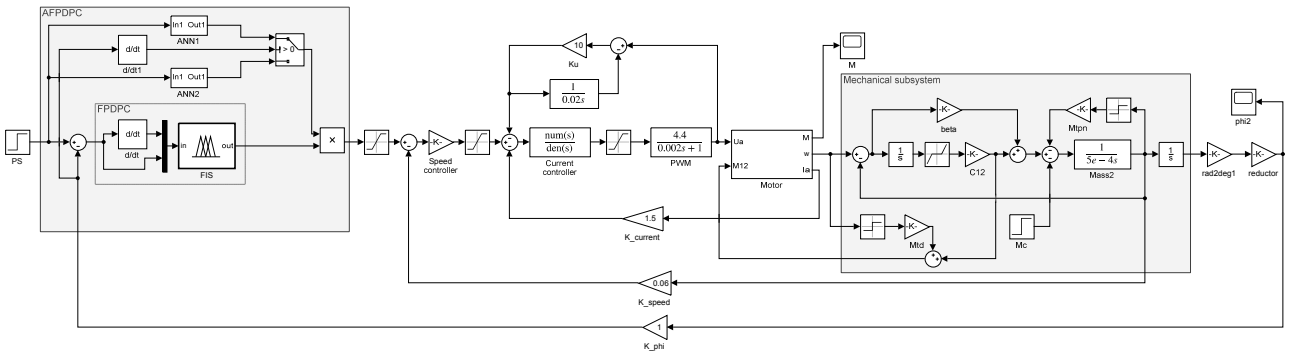

Fig. 1. Block diagram of the EMS of the vertical guidance of the PGs with fuzzy PD position regulator

To study the dynamics and statics of the guidance process of the PGs of the proposed positional EMS, its structural model is created in the Matlab Simulink application with the option to use to compare the dynamics of the classical proportional and the proposed adaptive fuzzy proportional-differential controller in the position control circuit.

Testing of the built three-circuit position with the above-mentioned subordinate adjustment of the EMS coordinates of the guidance of the PGs is performed when using in the control circuit of the position of the classical proportional controller to adjust it to the modular optimum.

Figure 2 shows the time dependencies of the aiming angle adjustment obtained for this model for three positioning angles: 17°, 35° and 60°. The P-position controller is set to the optimal dynamics (optimal law of motion) for the positioning angle φ_{ref} = 35° with transmission factor k_{pn} = 2.11. When positioning at other guidance angles, overregulation and tightening modes are observed.

Synthesis of fuzzy PD. The synthesis of the fuzzy PD regulator and the strategy of fuzzy control of the position of the PGs are based on the use of empirically acquired knowledge about the design, control features, perturbations and indicators of the positioning modes of the PGs of the BM-21.

The fuzzy inference system (FIS) (see Fig. 1) of the PD position controller is presented by the Mamdani model which has two inputs: for proportional $x_1 = e(t)$ and

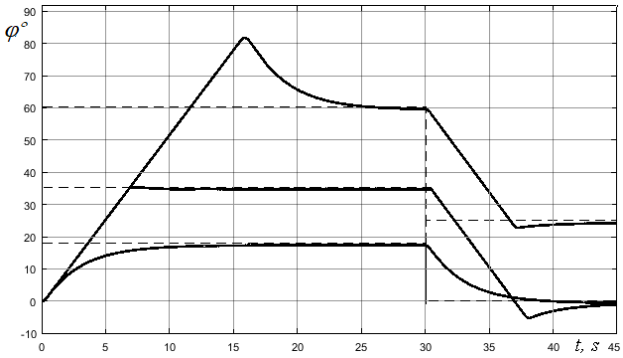

Fig. 2. Reactions $\varphi(t)$ of the EMS to abrupt control signals with proportional PC at the initial setting of the PGs at angles of 17°, 35° and 60° and the subsequent one at 0°, 0° and 35°, respectively

differential $x_2 = de(t)/dt$, where $e(t)$ is the error of angle adjustment $e(t) = \varphi_{ref}(t) - \varphi(t)$ (where $\varphi_{ref}(t)$, $\varphi(t)$ are the signals of the set and current positioning angle of the PGs, respectively).

For the linguistic description of the input variables x_1 and x_2, two trapezoidal external (N, P) and one triangular internal term (Z) with symmetric ranges of change are accepted (Fig. 3).

For the linguistic description of the original linguistic variable of the FIS U_{FIS} which gives the control signal of the speed controller $U_{c.\omega} = U_{FIS}$, two trapezoidal external (Nu, Pu) and one triangular internal term (Zu) with symmetric ranges of change are accepted (Fig. 4).

The functional relationship between the angle reference signal φ_{ref} and the output signal of the FIS U_{FIS}, which is the reference signal $U_{c.\omega}$ of the P-speed controller in such a control strategy is given in linguistic form, namely a set of fuzzy rules of the type (IF…AND…THEN).

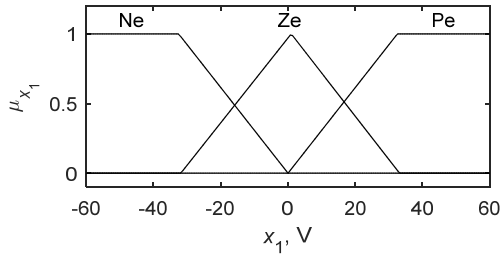

Fig. 3. FIS membership functions of input variables x_1 and x_2

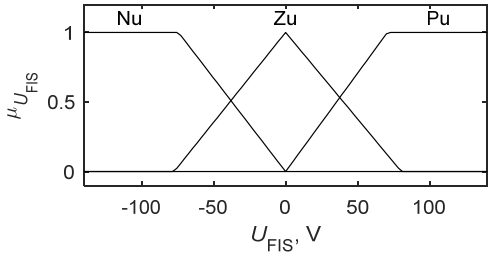

Fig. 4. FIS source variable membership functions U_{FIS}

The FIS rule base is formed on the basis of the analysis of the change of the control error of the position $e(t) = \varphi_{ref}(t) - \varphi(t)$, its derivative $de(t)/dt$ and the current angle of the position of the PGs $\varphi(t)$. The rule base was formed on the basis of comparison of time dependencies of change of desirable and actual (at proportional PC) reactions of EMS at positioning of the PGs on the angle φ_{ref} = 35°. The desired response corresponded to the optimal law of motion – positioning at maximum speed and stop without over-adjustment and traction mode. The optimal transmission factor of the P-position controller was calculated under the modular optimum condition.

The compiled rule base and other parametric and algorithmic degrees of freedom of the fuzzy PD regulator were specified by the results of mathematical experiments on the compiled Simulink model of the developed positional ACS (Fig. 1) by the value of the variant of the integrated quality indicator (T is the regulation time)

$$I = \int_0^{\dot{O}} t \cdot e(t)^2 dt \rightarrow \min. \qquad (3)$$

The obtained rule base of fuzzy PD-position regulator is shown in Table 1.

Table 1

FIS rule base

		Adjustment error – x_1		
		Ne	*Ze*	*Pe*
Derivative of adjustment error – x_2	*Nde*	*N*	*Z*	*Z*
	Zde	*N*	*Z*	*P*
	Pde	*Z*	*Z*	*P*

Figure 5 shows the 3D surface of the output signal of the designed fuzzy PD-position controller on the plane of change of the input linguistic variables x_1 and x_2 of the designed FIS.

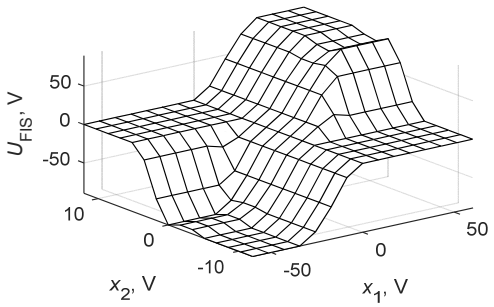

Fig. 5. Characteristics input/output $U_{FIS}(x_1, x_2)$ of the designed fuzzy PD-position controller

Study of positional EMS. The obtained reactions of EMS with the designed fuzzy PD-position regulator when testing control signals for small (φ_{ref} = 15° and 0°), medium (φ_{ref} =35° and 0°) and large (φ_{ref} = 60° and 0°) displacement of the PGs are shown in Fig. 6.

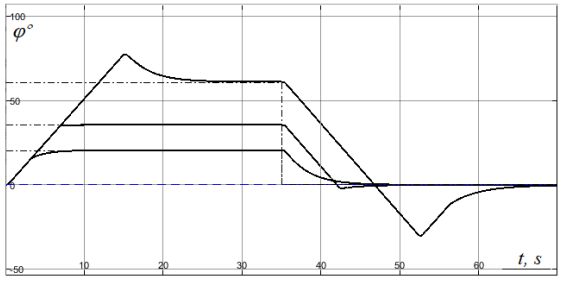

Fig. 6. EMS reactions with fuzzy PD-position regulator

In comparison with the P-regulator (see Fig. 2), when using a fuzzy PD regulator, the position of overregulation and regulation time are smaller.

But to achieve complete invariance of indicators of dynamics and statics of positioning to the value of the control signal (to the value of displacement), i.e. to obtain optimal laws of motion of the PGs for any positioning angles only by changing the parametric and algorithmic degrees of freedom of the designed Mamdani FIS (fuzzy PD position regulator) – no succeeded.

Therefore, in order to obtain optimal laws of motion when positioning the PGs at any angles without over-regulation and traction modes at the maximum possible speed, it is proposed to use the adaptation of the fuzzy PD-position regulator model to change the control signal $\varphi_{ref}(t)$. It is proposed to perform the adaptation by normalizing the output signal of the fuzzy PD controller:

$$U_{FIS}^n = k_n(\varphi_{ref}) \cdot U_{FIS} = U_{c.\omega}, \qquad (4)$$

where U_{FIS}^n is the normalized output signal of the fuzzy PD-position controller, which is the control signal of the speed controller $U_{c.\omega}$ of the positional EMS providing the movement of the PGs; $k_n(\varphi_{ref})$ is the dependence of the normalizing coefficient.

A series of mathematical experiments were performed on the Simulink model to obtain the normalizing functional dependence $k_n(\varphi_{ref})$. For different admissible signals of the task φ_{ref}, the position of the PGs, the value of the normalizing coefficient k_n, at which the

optimal law of motion of the PGs was obtained, is determined.

The analysis of the research results showed that this dependence is asymmetric with respect to the average positioning angle of 35° and different in the modes of raising and lowering the PGs (for φ_{ref} = 35° k_n = 1). This is explained by the active nature of the load torque, the reactive moment of friction, the different action of torsions, and so on. These factors in different ways affect the dynamics indicators of the movement when raising and lowering the PGs. The obtained dependencies $k_n(\varphi_{ref})$ when raising (⟶) and lowering (⟵) of the PGs are shown in Fig. 7.

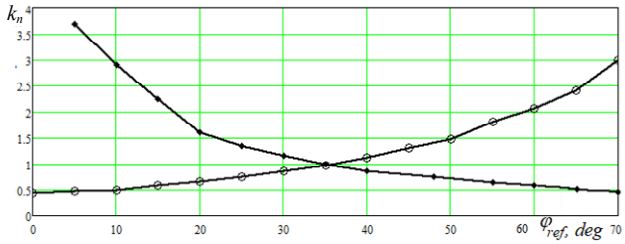

Fig. 7. Dependencies of the normalizing factor $k_n(\varphi_{ref})$ of the FIS output signal for the movement of the PGs up (⟶) and down (⟵)

These dependencies are reproduced in the structure of such an adaptive fuzzy PD-position controller (AFPDPC) by two artificial neural networks (ANN1 and ANN2, Fig. 8 and Fig. 1) of direct signal propagation or other static nonlinear functional transducers.

Figure 8 shows a block diagram of the proposed AFPDPC of the guide package, which indicates: PS – position setter, FPPDS – fuzzy proportional-differential position controller, Plant – control object.

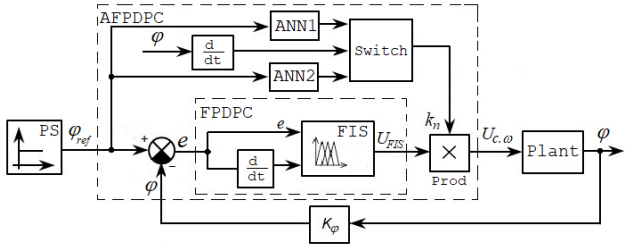

Fig. 8. Block diagram of adaptive fuzzy PD-position regulator of EMS of guidance of the PGs

Switching between the branches up/down of the adaptation coefficient $k_n(\varphi_{ref})$· in the structure of AFPDPC is performed as a function of changing the speed (acceleration sign), which is implemented in the Switch (Fig. 8). At the output of the Switch, the current value of the normalizing factor k_n is formed which is fed to the input of the multiplication element Prod at the output of which the speed reference signal $U_{c.\omega}$ is formed according to (4).

The obtained structural model of AFPDPC is implemented in the structure of the Simulink model of positional EMS of guidance of the PGs (see Fig. 1).

Figures 9, 10 show the time dependencies of the aiming angle $\varphi_{ref}(t)$ obtained on this model during the operation of two programs of changing in the discrete control signal $\varphi_{ref}(t)$ of the position of the PGs (–·–·–) during the operation of the proposed AFPDPC (——) and, for comparison, of the proportional PC (- - -) .

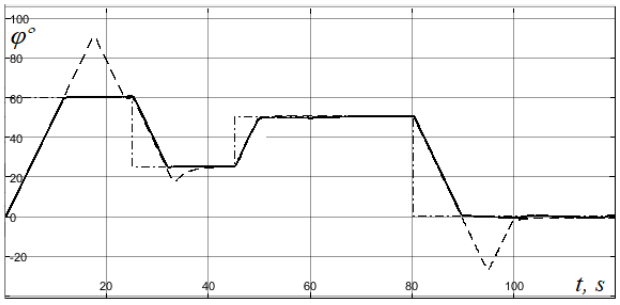

Fig. 9. Time dependencies $\varphi(t)$ at the PGs positioning at angles of 60°, 25°, 50°, and 0° at proportional PC (----) and AFPDPC (——), (–·–·–) – position reference signal

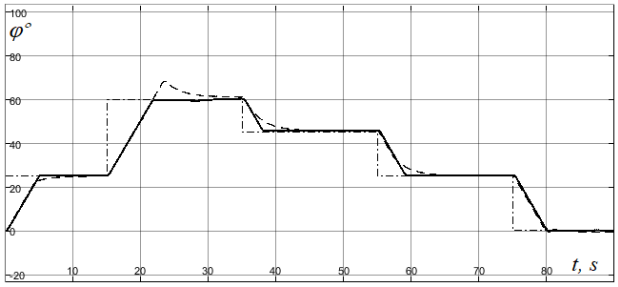

Fig. 10. Time dependencies $\varphi(t)$ at the PGs positioning at angles of 25°, 60°, 45°, 25°, and 0° at proportional PC (----) and AFPDPC (——), (–·–·–) – position reference signal

According to the first program, PG was alternately set at angles φ_{ref} = 60°, 25°, 50°, and 0° (Fig. 10), and according to the second one φ_{ref} = 25°, 60°, 45°, 25°, and 0° (Fig. 10). These time dependencies $\varphi(t)$ of the PG positioning process are obtained when they are loaded by missiles by 50 %.

The value of the accepted quality indicator (3) in the operation of the P-position regulator was 4.15 degrees^2·s, and in AFPDPC was 3.72 degrees^2·s (Fig. 9, the first program) and 3.91 degrees^2·s and 3.69 degrees^2·s, respectively, for the second program (Fig. 10). The improvement in quality when using AFPDPC was 10.4 % and 5.6 % for the first and the second program of change in $\varphi_{ref}(t)$, respectively.

A comparative analysis of the obtained time dependencies $\varphi(t)$ for the discrete (single) nature of the change $\varphi_{ref}(t)$ shows an improvement in the quality of dynamics during the operation of the proposed AFPDPC when positioning PG at different guidance angles regardless of the direction of movement (raising or lowering) in comparison with use of the classical P-regulator in a contour of position of EMS of guidance of the PG.

To obtain a more complete assessment of the dynamics of the synthesized positional EMS of the PG motion with AFPDPC, the guidance processes $\varphi(t)$ with sinusoidal change of the position reference signal $\varphi_{ref}(t)$ were studied (this mode of operation is not typical for the PG guidance mechanism). The obtained dependencies $\varphi(t)$ are shown in Fig. 11.

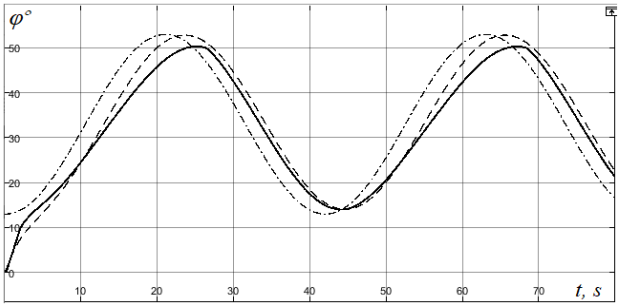

Fig. 11. Time dependencies $\varphi(t)$ of working off of a sinusoidal reference signal $\varphi_{ref}(t)$ (-.-.-) at proportional PC (----) and AFPDPC (▬▬)

The main perturbations that affect the dynamics of the movement of the PGs in the proposed positional EMS of guidance are the moment of static load and the moment of inertia of the guidance mechanism of the PGs which change when they are loaded differently by missiles.

Figure 12 shows the processes $\varphi(t)$ obtained in the model when positioning the PG at an angle of 35° followed by installation in the initial position of 0° at 50 % load (Fig. 12,*a*) and at full load (Fig. 12,*b*) during the operation of proportional PC and the proposed AFPDPC which illustrate the parametric sensitivity of the EMS of guidance of the PGs with these PC.

Analysis of the obtained positioning processes $\varphi(t)$ shows a lower sensitivity of the EMS with AFPDPC compared to the classical proportional PC.

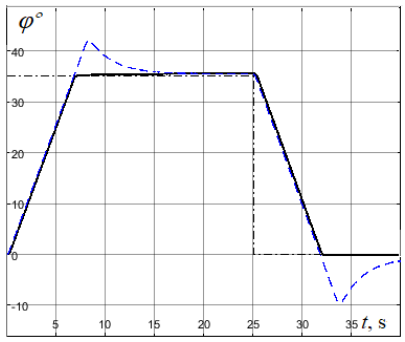

a

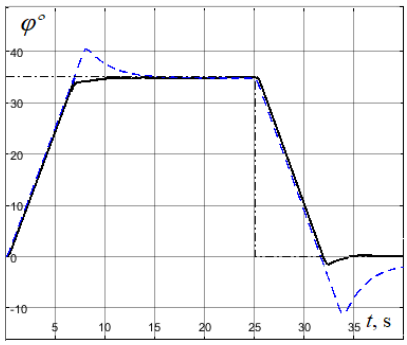

b

Fig. 12. Time dependencies $\varphi(t)$ at positioning of PG on an angle of 35° and 0° at proportional PC (----) and AFPDPC (▬▬) for 50 % (*a*) and 100 % (*b*) of loading of PG, (-.-.-) – position reference signal

Conclusions.

1. The expediency of using fuzzy control models to improve the indicators of dynamics and statics of the process of guidance of the PGs is substantiated.

2. The structure is developed and the fuzzy proportional-differential PC is designed with adaptation to the position reference signal.

3. The structural model of the developed positional EMS of guidance of the BM-21 weapon is created and its realization in the Simulink application of Matlab code is executed.

4. Computer researches of indicators of dynamics of movement of PGs at installation of the weapon on various angles of guidance, various character of $\varphi_{ref}(t)$ and at various loadings of a package of guides are carried out.

5. The obtained results of computer researches have shown that when using the designed adaptive fuzzy PD- position regulator, optimal without over-regulation and tightening modes and with maximum speed laws of movement of guide packets in the full range of guidance angles and at different loads of the PGs are realized.

6. When using the developed system solutions for the control circuit of the EMS adjustment position of the BM-21 armament guidance, a high level of robustness of the dynamics indicators is achieved until the change in the moment of static load and the moment of inertia of the guidance mechanism of the guide package.

Conflict of interest. The authors declare that they have no conflicts of interest.

REFERENCES

1. Krainyk L.V., Hrubel M.H., Yalnytskyi O.D. Analysis of development of the modern fighting wheeled machines. *Systems of Arms and Military Equipment*, 2017, no. 1 (49), pp. 126-131. Available at: http://www.hups.mil.gov.ua/periodic-app/article/17585/eng (accessed 12 October 2020). (Ukr).

2. *BM-21 Combat Vehicle. Technical description and operating instructions*. Moscow, Voenizdat Publ., 1982. 99 p. (Rus).

3. Kuznetsov B.I., Nikitina T.B., Kolomiets V.V., Bovdui I.V. Improving of electromechanical servo systems accuracy. *Electrical Engineering & Electromechanics*, 2018, no. 6, pp. 33-37. doi: https://doi.org/10.20998/2074-272X.2018.6.04.

4. Kuznetsov B.I., Nikitina T.B., Bovdui I.V., Kobilyanskiy B.B. Improving of electromechanical stabilization systems accuracy. *Electrical Engineering & Electromechanics*, 2019, no. 2, pp. 21-27. doi: https://doi.org/10.20998/2074-272X.2019.2.04.

5. Paranchuk Ya.S., Chumakevych V.O., Evdokimov P.M., Moskalyk V.O. High-speed electromechanical guidance and stabilization system based on pulse-width converter with fuzzy control. *Proceedings of International Scientific and Technical Conference «Problems of Enhancing the Energy Efficiency of the Electromechanical Converters in Electrical Energy Systems»*, Sevastopol, Ukraine, 2013, pp. 71-72. (Ukr).

6. Paranchuk Y., Evdokimov P., Kuznyetsov O. Electromechanical positioning system with a neuro-fuzzy corrector. *Przeglad Elektrotechniczny*, 2020, no. 9, pp. 52-55. doi: https://doi.org/10.15199/48.2020.09.11.

7. Chilikin M.G., Klyuchev V.I., Sandler A.S. *Theory of Automated Electric Drives*. Moscow, Energiya Publ., 1979. 616 p. (Rus).

8. Lebedev Ye.D., Neimark V.Ye., Pistrak M.Ya., Slezhanovskiy O.V. *Control of DC Electric Drives with Semiconductor Converters*. Moscow, Energiya Publ., 1970. 200 p. (Rus).

9. De Azevedo H. R., Branodao S. F. M., Da Mota Alves J. B. A fuzzy logic controller for DC motor position control. *Proceedings of IEEE 2nd International Workshop on Emerging*

Technologies and Factory Automation (ETFA '93), 1993, pp. 18-27. doi: https://doi.org/10.1109/etfa.1993.396433.

10. Manikandan R., Arulmozhiyal R. Position control of DC servo drive using fuzzy logic controller. *2014 International Conference on Advances in Electrical Engineering (ICAEE)*, 2014, pp. 1-5. doi: https://doi.org/10.1109/icaee.2014.6838474.

11. Priymak B.I., Bondarenko M.M., Khalimovsky O.M. Fuzzy control of electromechanical objects. *Bulletin of Scientific Works of Dniprodzerzhynsk State Technical University. Special Issue «Problems of Automated Electric Drive»*, 2007, pp. 308-311. (Ukr).

12. Lukichev D.V., Demidova G.L. Fuzzy control system of positioning servo drives of elastic coupling rotary supports, *Vestnik IGEU*, 2013, no. 6, pp. 60-64. Available at: http://vestnik.ispu.ru/sites/vestnik.ispu.ru/files/publications/str.60-64_0.pdf (accessed 12 October 2020). (Rus).

13. Paranchuk Y., Matsyhin A. The system of arc lengths regulation of an electric arc furnace with a neuro-controller, *Przeglad Elektrotechniczny*, 2013, vol. 89, no. 3A, pp. 271-273. Available at: http://pe.org.pl/articles/2013/3a/58.pdf (accessed 12 October 2020).

14. Ying H. *Fuzzy Control and Modeling: Analytical Foundations and Applications*, IEEE press, 2000. 342 p. Available at: https://ieeexplore.ieee.org/book/5263877 (accessed 12 October 2020).

15. Lozynskyy O., Paranchuk Y., Paranchuk R. Fuzzy control law of electrode travel in arc steelmaking furnace. *2015 16th International Conference on Computational Problems of Electrical Engineering (CPEE)*, 2015, pp. 103-106. doi: https://doi.org/10.1109/cpee.2015.7333349.

16. Mendel J. M., John R. I. B. Type-2 fuzzy sets made simple. *IEEE Transactions on Fuzzy Systems*, 2002, vol. 10, no. 2, pp. 117-127. doi: https://doi.org/10.1109/91.995115.

17. Paranchuk Ya.S. , Paranchuk R.Ya. Neural Network System for Continuous Voltage Monitoring in Electric Arc Furnace. *Naukovyi Visnyk Natsionalnoho Hirnychoho Universytetu*, 2016, iss. 2, pp. 74-80. Available at: http://nvngu.in.ua/index.php/en/archive/on-divisions-of-science/electrical-engineering/3398-neutral-network-system-for-continuous-voltage-monitoring-in-electric-arc-furnace (accessed 12 October 2020).

18. Paranchuk Y.S., Paranchuk R.Y. Research of arc furnace electrical mode with a fuzzy control model. *Electrical Engineering & Electromechanics*, 2020, no. 4, pp. 30-36. doi: https://doi.org/10.20998/2074-272X.2020.4.05.

19. Begian M.B., Melek W.W., Mendel J.M. Stability analysis of type-2 fuzzy systems. *2008 IEEE International Conference on Fuzzy Systems (IEEE World Congress on Computational Intelligence)*, 2008, pp. 947-953. doi: https://doi.org/10.1109/fuzzy.2008.4630483.

20. Lozynskyy O., Paranchuk Y., Kobylianskyi O. Simulink model of electric modes in electric arc furnace. *2017 IEEE International Young Scientists Forum on Applied Physics and Engineering (YSF)*, 2017, pp. 54-57. doi: https://doi.org/10.1109/ysf.2017.8126591.

Received 05.04.2021
Accepted 09.05.2021
Published 25.06.2021

Ya.S. Paranchuk[1], *Doctor of Technical Science, Professor,*
Y.V. Shabatura[2], *Doctor of Technical Science, Professor,*
O.O. Kuznyetsov[2], *PhD, Associate Professor,*
[1] Lviv Polytechnic National University,
12, S. Bandera Str., Lviv, 79013, Ukraine,
e-mail: yparanchuk@yachoo.com
[2] Hetman Petro Sahaidachnyi National Army Academy,
32, Heroes of Maidan Str., Lviv, 79026, Ukraine,
e-mail: shabaturayuriy@gmail.com,
oleksiy.kuznyetsov@ukr.net (Corresponding author)

How to cite this article:
Paranchuk Ya.S., Shabatura Y.V., Kuznyetsov O.O. Electromechanical guidance system based on a fuzzy proportional-plus-differential position controller. *Electrical Engineering & Electromechanics*, 2021, no. 3, pp. 25-31. doi: https://doi.org/10.20998/2074-272X.2021.3.04.

UDC 621.314 https://doi.org/10.20998/2074-272X.2021.3.05

S.A. Naida, Y.O. Onykienko, O.I. Drozdenko, O.I. Smolenska, V.S. Baran, N.O. Iakunina

ANALYSIS OF THE INFLUENCE OF LOAD INDUCTANCE ON NONLINEAR DISTORTIONS OF A CLASS D AMPLIFIER CAUSED BY «DEAD TIME»

Goal. *Analysis of the effect of load inductance at the output of the class D amplifier for different values of the duration of «dead time» and assessment of the adequacy of existing mathematical models for calculating the THD at the output of the amplifier depending on the duration of «dead time».* ***Methodology****. The study of the effect of «dead time» on the THD was performed using a computer model of the half-bridge converter board EPC9035 from Efficient Power Conversion. This board contains GaN transistors EPC2022 eGaN®, the corresponding control driver and other necessary elements for operation. The use of GaN transistors has made it possible to investigate the operation in a wide range of frequent switching, both to control the motor and to amplify the audio signal.* ***Results****. It is established that the value of load inductance affects the level of nonlinear distortions caused by «dead time». At inductance values that provide a constant sign of the output current, a difference arises between the duration of the input and output pulses, which increases the THD. At inductance values, when the choke current changes sign during a pulse, there is no error between the duration of the input and output pulses. Changing the inductance changes the relationship between the error signal and the non-error signal. THD changes accordingly. At high conversion frequencies, the voltage spikes caused by the choke current through the built-in diodes during the dead time are partially compensated by overcharging the output capacitance of the transistors, which also reduces harmonic distortion.* ***Originality****. For the first time, the value of the THD at the outlets in the fallowness of the different indices of the inductance of the choke and the theoretical calculation of the value in the results of the computer model was obtained.* ***Practical significance.*** *The dependence of the THD values on the inductance of the choke for converters with a switching frequency range from 1 kHz to 400 kHz, which allows them to be used both to control the motor and to amplify the audio signal.* References 10, tables 2, figures 8.

Key words: **GaN transistors, class D amplifier, nonlinear distortion, dead time, THD.**

В роботі досліджено вплив індуктивності навантаження підсилювача класу D на значення коефіцієнту гармонічних спотворень (КГС) на виході для різних значень тривалості «мертвого часу» або вимкненого стану вихідних транзисторів. Оцінена адекватність існуючих математичних моделей для розрахунку КГС на виході підсилювача в залежності від тривалості «мертвого часу». Наведено результати комп'ютерного моделювання підсилювача класу D та досліджено значення КГС на виході в залежності від різних номіналів індуктивності вихідного дроселя. Виконано порівняння теоретично обчислених значень з результатами комп'ютерного моделювання. В результаті дослідження встановлено, що КГС, спричинений наявністю «мертвого часу» залежить від індуктивності навантаження. Отриманий у результаті моделювання КГС співпадає з розрахованим за формулою тільки для певних значень індуктивності навантаження. В моделі використано GaN транзистори, що дозволило дослідити роботу підсилювача у широкому діапазоні частот перемикання. Бібл. 10, табл. 2, рис. 8.

Ключові слова: **GaN транзистори, підсилювачі класу D, нелінійні спотворення, «мертвий час», коефіцієнт гармонічних спотворень.**

В работе исследовано влияние индуктивности нагрузки усилителя класса D на значение коэффициента гармонических искажений (КГИ) на выходе для различных значений продолжительности «мертвого времени» или выключенного состояния выходных транзисторов. Оценена адекватность существующих математических моделей для расчета КГИ на выходе усилителя в зависимости от продолжительности «мертвого времени». Приведены результаты компьютерного моделирования усилителя класса D и исследованы значение КГИ на выходе в зависимости от различных номиналов индуктивности дросселя. Выполнено сравнение теоретически вычисленных значений с результатами компьютерного моделирования. В результате исследования установлено, что КГИ, вызванный наличием «мертвого времени» зависит от индуктивности нагрузки. Полученный в результате моделирования КГИ совпадает с рассчитанным по формуле только для определенных значений индуктивности нагрузки. В модели использованы GaN транзисторы, что позволило исследовать работу усилителя в широком диапазоне частот переключения. Библ. 10, табл. 2, рис. 8.

Ключевые слова: **GaN транзисторы, усилители класса D, нелинейные искажения, мертвое время, коэффициент гармонических искажений.**

Introduction. Class D amplifiers are widely used in electric drive, audio equipment and other areas where it is necessary to amplify the input signal with maximum efficiency and minimum distortion. The key mode of operation provides efficiency theoretically up to 100 %, and the class D amplifiers themselves are small in size and weight compared to linear amplifiers. The disadvantage of the key mode is electromagnetic interference. Class D amplifiers, as well as other types of amplifiers, are also characterized by nonlinear distortion of the amplified signal. One type of nonlinear distortion is the distortion caused by the so-called «dead time» – the time interval during which the output transistors must be switched off to avoid through currents. Nonlinear distortions of the output signal due to «dead time» are often ignored due to their relatively small values. However, when amplifying the sound signal, such distortions are clearly visible to the ear and significantly reduce the quality of perception of phonograms. Also distortions are undesirable for the output voltage for converters that work as part of power grids.

Studies of the effect of «dead time» on the level of nonlinear distortion at the output of the class D amplifier are sufficiently described in the literature. The analysis of

distortions caused by «dead time» is described in [1], where the differences between the shapes of input and output signals for different types of modulation are analyzed. The result is the calculated signal spectra at the output for the specified values of «dead time». In [2] the output signal is presented as an input PWM signal with the addition of «dead time» intervals, analytical expressions for calculating the values of the harmonics of the output signal are given.

In [3] the mechanisms of creation of nonlinear distortions caused by «dead time» for the voltage converter are considered. The influence of parasitic output capacitances of transistors and current pulsations of output choke current on the level of distortions is analyzed, the method of their compensation is offered. However, no appropriate methodology is given for calculating the THD. An experimental study of the factors influencing the THD of a class D amplifier on GaN/SiC transistors was performed in [4]. The growth of THD with the increase of «dead time» for active load is established. In [5], a study of the dependence of THD on the load current for different values of «dead time» was performed, and it was shown that the main contribution is made by odd harmonics.

Thorough studies of the influence of the duration of the «dead time» on the THD were performed by Chierchie et al. in [6-8]. Theoretical calculations are given, computer modelling and experimental researches of dependence of THD on value of «dead time» are carried out, practical recommendations on a choice of its duration are given.

However, in the above-mentioned works, the effect of the value of the load inductance on the THD is not evaluated, although the current through the output choke is considered as one of the factors of nonlinear distortion.

Thus, it is expedient to investigate the dependence of the processes of formation of nonlinear distortions at the output of the amplifier during the interval of «dead time» on the inductance of the load.

The goal of the work is to analyze the effect of class D amplifier load inductance on THD caused by the presence of «dead time» and assess the adequacy of existing mathematical models for calculating THD at the amplifier output for different values of «dead time».

To achieve this goal it was necessary to solve the following tasks:

- to analyze with the help of a computer model the value of THD at the output of the class D amplifier depending on the different values of the inductance of the choke for active-inductive load;
- to compare the theoretically calculated THD with the results of computer simulation;
- to explain the results obtained and identify the need for and further ways of conducting research.

Description of the computer model. The study of the effect of «dead time» on the THD was performed using a computer model of the half-bridge converter board EPC9035 of Efficient Power Conversion. This board contains GaN transistors EPC2022 eGaN®, the corresponding control driver and other necessary elements for operation. The use of GaN transistors has made it possible to investigate the operation in a wide range of frequent switching, both to control the electric motor and to amplify the audio signal. The main parameters of the PWM signal in the simulation are given in Table 1.

Table 1

PWM signal parameters

Switching frequencies	1 kHz, 2 kHz, 100 kHz, 400 kHz
Signal frequencies	50 Hz
Depth of modulation	0.6

For computer simulation, a modified model of a half-bridge transducer on GaN transistors was used, which is described in [9]. The peculiarity of this model is that the driver chip of the output transistors LM5113 is replaced by virtual switches S1, S2, and control voltage sources are replaced by transistors V4, V5. The existing model of the LM5113 chip does not provide accurate reproduction of processes over time, as described in [10], and in addition, the use of switches and voltage sources simplifies the model and reduces the simulation time. In the proposed model, the power supply is represented as bipolar for symmetric amplification of the sinusoidal signal.

The computer model of the amplifier on GaN transistors is shown in Fig. 1. Element U1 is a pulse-width modulator with a built-in sawtooth voltage generator. Logic elements U2 and U3 are input buffers. Element U2 also inverts the input signal. Logic elements U4 and U5 are buffers of «dead time» circuit formation. The *RC* circuit R1, C1 and the diode D1 form the switch-on delay time («dead time») of the transistor Q1, the *RC* circuit R2, C2 and the diode D2 form the switch-on delay time of the transistor Q2. At high frequencies, the conversion of the *RC* circuit is the only way to form a «dead time», when its duration is tens of nanoseconds or less. At sufficiently low conversion frequencies, the formation of dead time is possible by digital methods [3].

Switches S1, S2 are used to generate control voltages of transistors Q1, Q2. When the switch S1 is closed, the voltage of the source V4 is applied between the source and the gate of the transistor Q1. The charge current of the input capacitor of the transistor Q1 is limited by the internal resistance of the switch S1. After opening this switch, the discharge of the input capacitor occurs through the resistor R3. Similar processes occur when controlling the transistor Q2. The load of the amplifier is the choke L1 and resistor R8. Components for modelling losses on the printed circuit board are resistors R1, R10. The decoupling capacitor C3 is shown in the diagram with parasitic parameters: choke L2 (inductance of terminals), and resistor R10 (internal resistance). The parasitic parameters of the supply wires are represented by chokes L3, L4 and resistors R11, R12. The 12 V power supply is split in half to speed up the simulation process. The point of connection of the sources is connected to the «ground», which made it possible to abandon the use in the circuit of a capacitor divider, which is necessary for the operation of a half-bridge converter when powered by a unipolar source.

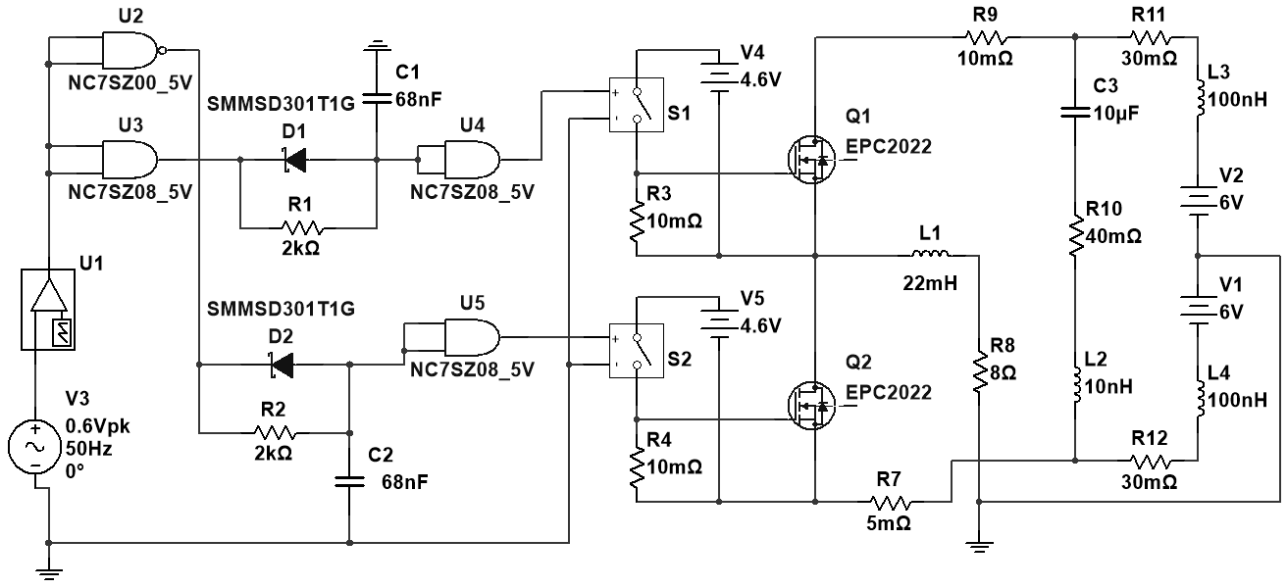

Fig. 1. Computer model of a half-bridge transducer for estimating the effect of «dead time» duration on THD

Problem description. Figure 2 illustrates the process of creating nonlinear distortions due to the introduction of «dead time». The input PWM pulses $U_{in}(t)$ are indicated by a line with triangles, the pulses at the output of the amplifier $U_0(t)$ – by a solid line, the output current $I_0(t)$ – by a dotted line , «dead time» is shaded. As can be seen from Fig. 2, the duration of the input and output pulses do not match when the sign of the output current is constant. In this case, at the output of the amplifier there are nonlinear distortions of the amplified signal, regardless of the method of implementation of the PWM. The reason is that during both «dead time» intervals the diode of only one of the transistors operates and provides current flow through the choke in the «dead time» interval, delaying the change of the signal at the output when the input signal has already changed the sign.

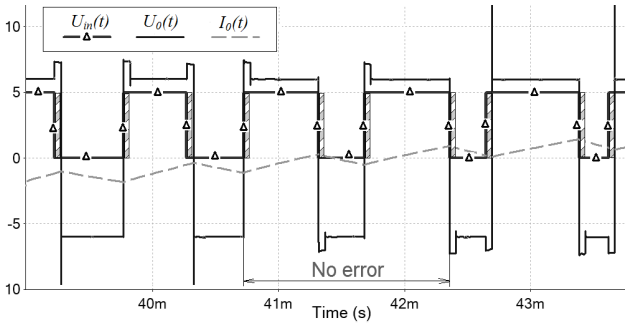

Fig. 2. Illustration of the process of creating nonlinear distortions due to the introduction of «dead time»

If the sign of the output current changes during the pulse duration, the current through the choke at different intervals of «dead time» flows through the diodes of different transistors. The duration of the input and output pulses are the same, and no distortion occurs. This interval is indicated in Fig. 2 as «No error». Thus, at certain values of inductance at the output of the amplifier and the depth of modulation, the delay in changing the sign of the output voltage disappears, and therefore the total value of the THD decreases. Therefore, it is advisable to investigate the effect of choke inductance at the output of the amplifier on the THD, taking into account that the load inductance, in particular class D sound amplifiers, can have a wide range of values.

Description of the mathematical model of the spectrum of the output signal to calculate the dependence of the THD on the duration of the «dead time». In [6], the authors proposed a method for calculating the THD, dividing the width-modulated signal at the output of the amplifier into three components: a symmetrical rectangular signal with a fill factor of $0.5p_c(t)$; a sequence of pulses, the duration of which depends on the modulating signal, $p_s(t)$, and the error signal $e(t)$ caused by «dead time». The output voltage of the amplifier is calculated by the formula given in [6]:

$$v_0(t) = p_c(t) + p_s(t) - e(t). \quad (1)$$

Accordingly, the spectrum of the output signal is the sum of the spectra of the components. The full spectrum at the output of the amplifier and the amplitude of the individual harmonics C_n is calculated by the following formulas [6]:

$$V_{o,p}(f) = P_{c,p}(f) + P_{s,p}(f) - E_p(f), \quad (2)$$

where

$$P_{c,p}(f) = jT\,\mathrm{sinc}\left(\frac{T}{2}f\right)\sin\left(\pi\frac{T}{2}f\right)\frac{\sin(\pi MTf)}{\sin(\pi Tf)}, \quad (3)$$

$$P_{s,p}(f) = \sum_{k=0}^{M-1}\frac{1}{j\pi f}\left(e^{-j2\pi(k+1/2)Tf} - e^{-j2\pi(kT+\tau_k)f}\right); \quad (4)$$

$$E_p(f) = \left(\sum_{k=0}^{\frac{M}{2}-1} e^{-j2\pi f(kT)} - \sum_{k=\frac{M}{2}}^{M-1} e^{-j2\pi f(kT+\tau_k)}\right)\times \quad (5)$$

$$\times\, 2\Delta\frac{\sin(\Delta f)}{\Delta f}e^{-j\pi\Delta f};$$

$$\tau_k = \frac{T}{2}\left[1+\frac{M}{\pi}\cot(\theta_k)+\frac{M}{2m\pi^2}\csc\theta_k\left(-2M+\right.\right. \quad (6)$$

$$\left.\left.+\sqrt{4M^2+6m_0^2\pi^2-2m\pi\left[4M\cos\theta_k+m\pi\cos(2\theta_k\right]}\right)\right];$$

$$\theta_k = 2\pi(k+0{,}5)/M\ ; \tag{7}$$

$$C_n = \frac{1}{MT} V_{o,p}(f)\,|_{f=\frac{n}{MT}}, \tag{8}$$

where $M = f_c/f_s$ is the ratio of the switching frequency f_c to the signal frequency f_s, $T = 1/f_c$ is the switching period, Δ is the duration of the «dead time» relative to the period T, m is the modulation depth, k is the number of the switching interval.

THD, which was used for comparison with the results of computer simulation, was calculated in % by the formula given below [6]:

$$THD = \frac{100}{|C_1|^2} \sum_{n=2}^{6} |C_n|^2\ , \tag{9}$$

where C_1 is the amplitude of the first harmonic of the signal.

Estimation of the influence of load inductance on THD values caused by «dead time». The calculation of the THD at the output of the amplifier is performed by the formula

$$THD = \frac{\sqrt{A_2^2 + A_3^2 + A_4^2 + \ldots + A_k^2}}{A_1}, \tag{10}$$

where A_1, A_2, ... A_k are the harmonics of the output signal.

To calculate the CGS, the first 7 harmonics were taken, by analogy with formula (9).

The computer model shown in Fig. 1, contains a pulse-width modulator U1, which increases the nonlinear distortion of the output signal. In order to estimate the contribution of nonlinear distortions of the modulator to the overall level, the THD at its output is calculated for each of the operating frequencies of the amplifier. The results of the calculations are given in Table 2.

Table 2

THD at the output of the PWM element for different frequencies of transformation

Parameters	THD, %
f_c = 1 kHz	0.033
f_c = 2 kHz	0.05
f_c = 100 kHz	0.012
f_c = 400 kHz	0.01

As can be seen from Table 2, THD values for different conversion frequencies vary in the range of 0.01–0.05 % and will be taken into account in further comparison of results. It should be noted that the feature of the PWM element U1 is the reduction of the THD at high conversion frequencies.

Figure 3 shows the results of the calculation of the THD at the output of the amplifier depending on the value of the inductance of the output choke. The simulation was performed for a signal frequency of 50 Hz and conversion frequencies of 1 kHz, 2 kHz, 100 kHz and 400 kHz. The duration of «dead time» during simulation was 10 %. The inductance values varied in the range from 47 μH to 22 mH. The value of the load resistor remained unchanged – 8 Ω.

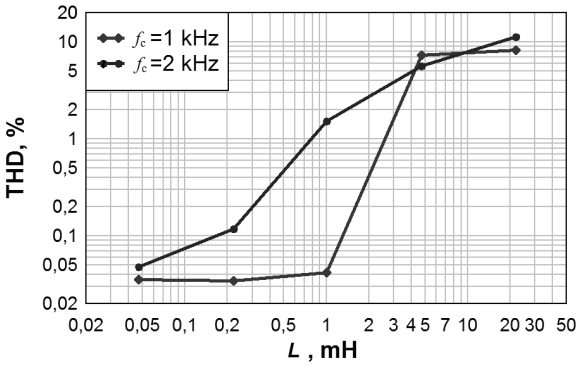

Fig. 3. Dependence of THD on the value of inductance of the output choke

As can be seen from Fig. 3, with increasing load inductance, the THD increases. At a maximum value of inductance of 22 mH, the maximum THD is observed both for the conversion frequency of 1 kHz and for the frequency of 2 kHz. Although the dependence for the frequency of 2 kHz is more gentle.

Similar dependencies are observed when amplifying the sound signal with conversion frequencies of 100 kHz and 400 kHz (Fig. 4). As the inductance of the choke increases, the distortions caused by the «dead time» increase. Although for a frequency of 400 kHz after a certain maximum there is a decrease in THD.

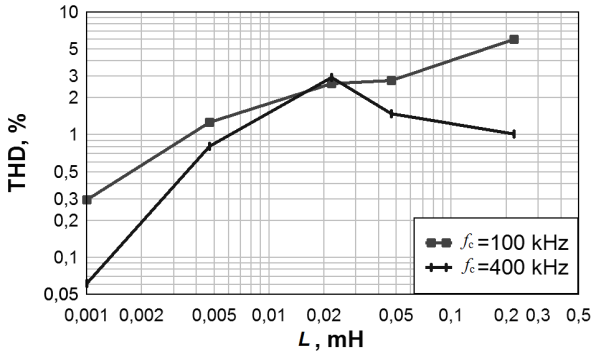

Fig. 4. Dependence of THD on the value of the inductance of the output choke for the conversion frequencies of 100 and 400 kHz

Thus, it can be argued that the value of the inductance at the output of the amplifier affects the level of nonlinear distortion caused by «dead time», changing the ratio of intervals when the current sign does not change (input and output signals do not match in duration) and changes (PWM signal pulse duration at the input and at the output coincides). Reducing the load circuit time constant also reduces the THD of the output signal, which was noted in [5].

Additional factors that affect the THD at low supply voltages may be the voltage jumps on the diodes of the transistors in the mode when the current sign does not change during the switching period. The fact that both transistors are closed and the choke current flows twice through the diode of one of the transistors can increase the THD. The voltage drop across the diode U_d is added to the supply voltage (Fig. 5,*a*) and changes the amplitude of the current $I_0(t)$ through the choke. Reducing the duration of «dead time» reduces the impact of output voltage $U_0(t)$

jumps on the THD. The effect of voltage drop across diodes on THD requires further research.

Figure 5,*b* shows the shape of the output pulses for a switching frequency of 400 kHz (solid line), when the sign of the output current $I_0(t)$ does not change. When the input voltage $U_{in}(t)$ changes to zero, there is a process of delaying the output voltage drop $U_0(t)$ due to the charge of the output capacitance of the transistor in the interval of «dead time». In the next «dead time» interval, the current flows through the diode and creates a delay in switching the output voltage compared to the input signal (line with triangles).

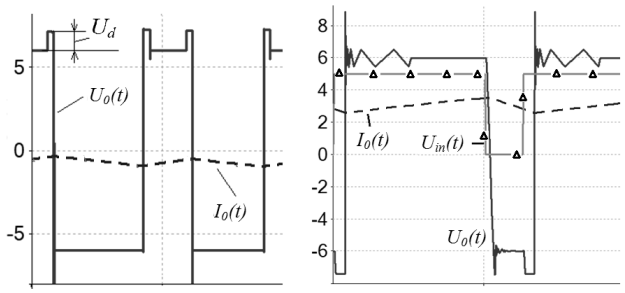

Fig. 5. Output voltage jumps due to voltage drop across diodes (*a*) and the effect of the output capacitance of the transistor on the shape of the output pulses (*b*)

Comparison of mathematical and computer simulation results. Next, a comparison of the THD calculated according to the formulas above with the THD obtained by simulation for different values of inductance of the choke is carried out. Figure 6 shows the dependencies of the THD on the duration of the «dead time» calculated by formula (1) and modelled for the following parameters of the amplifier: signal frequency f_s = 50 Hz, conversion frequencies f_c = 1 kHz, 2 kHz, modulation depth m = 0.6.

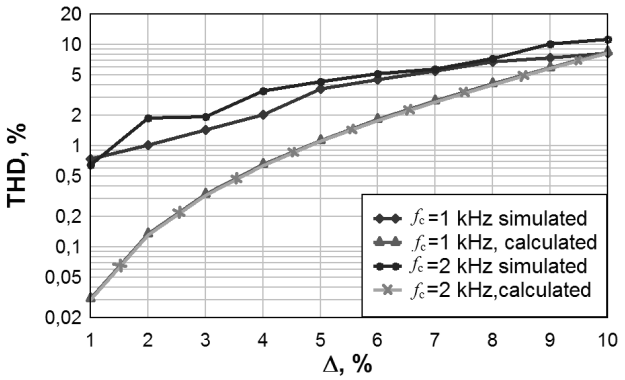

Fig. 6. Dependence of THD on the value of Δ for the inductance of the choke 22 mH

The curves show that the dependence of THD on the duration of «dead time» as a result of modelling exceeds the calculations by formula (1) by 0.6 % – 4 %. The high values of the THD can be explained by the fact that the inductance of the output choke provides the current sign constant throughout almost the entire period of the signal, which is amplified, so the THD increases with increasing Δ.

Figure 7 shows the curves of the THD dependence on the duration of the «dead time» for the case when the output inductance provides a change in the sign of the current twice for the switching period. In this case, the THD does not change significantly when changing Δ from 1 % to 10 %, which differs from the values of THD at the output of the amplifier, calculated by formula (9).

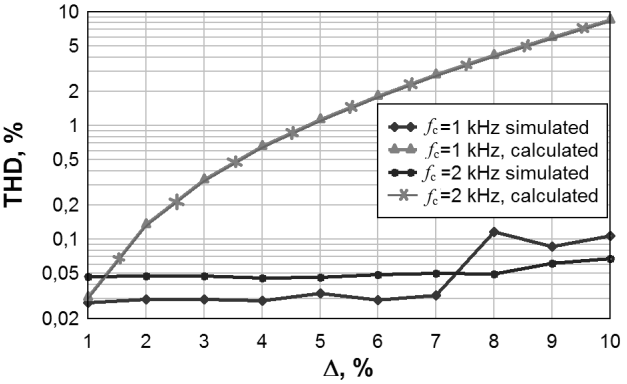

Fig. 7. Dependence of THD on the value of Δ for the inductance of the choke 470 μH

The greatest interest is the effect of load inductance on the THD at switching frequencies from 100 kHz, on which the sound amplifiers of class D operate. The dependencies of the THD on the duration of the «dead time» are shown in Fig. 8 for an inductance of 47 μH. The use of GaN transistors in this case provides a switching frequency of 400 kHz and higher.

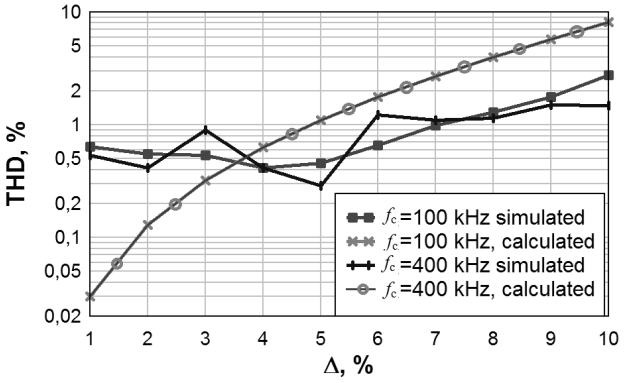

Fig. 8. Dependence of THD on the value of Δ for the inductance of the choke 47 μH

If for the switching frequency of 100 kHz there is an increase in THD with an increase of Δ from 0.5 % to 3 %, then for the switching frequency of 400 kHz the level of distortion at values of Δ > 6 % practically does not increase. Although the effect of inductance of 47 μH should be greater at a frequency of 100 kHz. This result can be explained by the recharging of the output capacitance of the transistors, which compensates for voltage jumps (see Fig. 3,*b*).

Thus, the dependence of THD on the duration of «dead time» as a result of modelling differs from the calculated one.

Conclusions.

The paper evaluates the influence of the load inductance at the output of the class D amplifier on the

level of nonlinear distortions caused by «dead time». As a result, it was found that reducing the value of inductance within certain limits reduces the THD. This is due to the reduction of the number of errors between the input and output signal, which occur at a constant sign of the inductance current during the output pulse. When the inductance decreases, the number of intervals in which there is no error increases. Thus, the change in the value of the load inductance leads to a change in the ratio of the intervals with and without error, and hence to a change in the THD.

At high conversion frequencies, the voltage jumps caused by the current through the built-in diodes during the «dead time» are partially compensated by recharging the output capacitance of the transistors, which also reduces nonlinear distortions.

The next stage of research is to create a mathematical model of the PWM signal at the output of the class D amplifier, which takes into account the effect of load inductance on the THD, and its experimental verification.

Conflict of interest. The authors declare that they have no conflicts of interest.

REFERENCES

1. Koeslag F., du T. Mouton H., Beukes H. J., Midya P. A detailed analysis of the effect of dead time on harmonic distortion in a class D audio amplifier. *AFRICON 2007*, 2007, pp. 1-7. doi: https://doi.org/10.1109/afrcon.2007.4401640.

2. Wu C. M., Lau Wing-Hong, Shu-Hung Chung H. Analytical technique for calculating the output harmonics of an H-bridge inverter with dead time. *IEEE Transactions on Circuits and Systems I: Fundamental Theory and Applications*, 1999, vol. 46, no. 5, pp. 617-627. doi: https://doi.org/10.1109/81.762927.

3. Li C., Gu Y., Li W., He X., Dong Z., Chen G., Ma C., Zhang L. Analysis and compensation of dead-time effect considering parasitic capacitance and ripple current. *2015 IEEE Applied Power Electronics Conference and Exposition (APEC)*, 2015, pp. 1501-1506. doi: https://doi.org/10.1109/apec.2015.7104546.

4. Mauerer M., Tüysüz A., Kolar J. W. Distortion analysis of low-THD/high-bandwidth GaN/SiC class-D amplifier power stages. *2015 IEEE Energy Conversion Congress and Exposition (ECCE)*, 2015, pp. 2563-2571. doi: https://doi.org/10.1109/ecce.2015.7310020.

5. Mauerer M., Kolar J. W. Distortion minimization for ultra-low THD class-D power amplifiers. *CPSS Transactions on Power Electronics and Applications*, 2018, vol. 3, no. 4, pp. 324-338. doi: https://doi.org/10.24295/cpsstpea.2018.00032.

6. Chierchie F., Paolini E. E. Analytical and numerical analysis of dead-time distortion in power inverters. *2010 Argentine School of Micro-Nanoelectronics, Technology and Applications (EAMTA)*, 2010, pp. 6-11. Available at: https://ieeexplore.ieee.org/document/5606373 (accessed 22 June 2020).

7. Chierchie F., Paolini E. E. Quasi-analytical spectrum of PWM signals with dead-time for multiple sinusoidal input. *2011 IEEE International Symposium of Circuits and Systems (ISCAS)*, 2011, pp. 1033-1036. doi: https://doi.org/10.1109/iscas.2011.5937745.

8. Chierchie F., Stefanazzi L., Paolini E. E., Oliva A. R. Frequency analysis of PWM inverters with dead-time for arbitrary modulating signals. *IEEE Transactions on Power Electronics*, 2014, vol. 29, no. 6, pp. 2850-2860. doi: https://doi.org/10.1109/tpel.2013.2276098.

9. Onikienko Y.O., Pilinsky V.V., Popovych P.V., Lazebnyi V.S., Smolenska O.I., Baran V.S. Modelling of operation modes and electromagnetic interferences of GaN-transistor converters. *Electrical Engineering & Electromechanics*, 2020, no. 3, pp. 37-42. doi: https://doi.org/10.20998/2074-272X.2020.3.06.

10. Gedz O., Lazebnyi V., Onikienko Y., Vlasjuk A. EMI simulation of GaN power stage for audio class D amplifiers. *2018 14th International Conference on Advanced Trends in Radioelecrtronics, Telecommunications and Computer Engineering (TCSET)*, 2018, pp. 204-207. doi: https://doi.org/10.1109/tcset.2018.8336187.

Received 03.04.2021
Accepted 10.05.2021
Published 25.06.2021

S.A. Naida[1], *Doctor of Technical Science, Professor,*
Y.O. Onykienko[1], *PhD, Associate Professor,*
O.I. Drozdenko[1], *PhD, Associate Professor,*
O.I. Smolenska[1], *Postgraduate Student,*
V.S. Baran[1], *Postgraduate Student,*
N.O. Iakunina[1], *PhD, Associate Professor,*
[1] National Technical University of Ukraine «Igor Sikorsky Kyiv Polytechnic Institute»,
37, Prospect Peremohy, Kyiv-56, 03056, Ukraine,
e-mail: yurionik@gmail.com (Corresponding author)

How to cite this article:
Naida S.A., Onykienko Y.O., Drozdenko O.I., Smolenska O.I., Baran V.S., Iakunina N.O. Analysis of the influence of load inductance on nonlinear distortions of a class D amplifier caused by «dead time». *Electrical Engineering & Electromechanics*, 2021, no. 3, pp. 32-37. doi: https://doi.org/10.20998/2074-272X.2021.3.05.

UDC 621.3.013 https://doi.org/10.20998/2074-272X.2021.3.06

K.V. Chunikhin, V.S. Grinchenko

NORMALIZATION OF DOUBLE-CIRCUIT OVERHEAD LINE MAGNETIC FIELD INSIDE KHRUSHCHEV BUILDING

This paper deals with the mitigation of 110 kV double-circuit overhead line magnetic field inside five-story Khrushchev buildings. We show that the magnetic field can exceed the reference level 0.5 μT in 90 % part of living space. To mitigate the magnetic field, we propose the inverted L-shaped grid shield with conductors on the wall and in the attic of the building. Using the analytical model of the grid shield and the numerical simulation, we determine the parameters of the L-shaped grid shield which provides the magnetic field normalization in 97 % part of living space. Further improvement of the grid shield profile, in particular, the placement of some conductors in the basement, allows to reduce the quantity of metal of the shield by 15 % while maintaining the shielding efficiency. Also we consider the magnetic field normalization for the overhead line with a rated current of 500 A. In this case, the quantity of metal of the grid shield increases 2.74 times. References 19, table 1, figures 5.
Key words: **magnetic field, overhead line, grid shield, reference level, quantity of metal.**

У роботі показано, що в п'ятиповерхових будинках хрущовської споруди, розташованих на границях охоронних зон двоколових повітряних ліній електропередачі 110 кВ, величина магнітного поля промислової частоти може перевищувати гранично допустимий рівень 0,5 мкТл в 90 % житлового простору. Для зменшення магнітного поля запропоновано використовувати Г-подібний ґратчастий екран, проводи якого розташовуються на стіні та на горищі будинку. Шляхом аналітичного та чисельного моделювання визначено параметри Г-подібного ґратчастого екрана, застосування якого дає змогу нормалізувати рівень магнітного поля в 97 % житлового простору. Подальше вдосконалення профілю ґратчастого екрана, зокрема, розміщення частини проводів у підвалі, дало змогу зменшити металоємність конструкції на 15 % при збереженні ефективності екранування. Також досліджено можливість нормалізації магнітного поля повітряної лінії з номінальним струмом 500 А. У цьому випадку металоємність ґратчастого екрана збільшується у 2,74 рази. Бібл. 19, рис. 5, табл. 1.
Ключові слова: **магнітне поле, повітряна лінія електропередачі, ґратчастий екран, гранично допустимий рівень, металоємність.**

В работе показано, что в пятиэтажных домах хрущевской постройки, расположенных на границах охранных зон двухцепных воздушных линий электропередачи 110 кВ, величина магнитного поля промышленной частоты может превышать предельно допустимый уровень 0,5 мкТл в 90 % жилого пространства. Для уменьшения магнитного поля предложено использовать Г-образный решетчатый экран, провода которого располагаются на стене и чердаке дома. Путем аналитического и численного моделирования определены параметры Г-образного решетчатого экрана, применение которого позволяет нормализовать уровень магнитного поля в 97 % жилого пространства. Дальнейшее совершенствование профиля решетчатого экрана, в частности, размещение части проводов в подвале, позволило уменьшить металлоемкость конструкции на 15 % при сохранении эффективности экранирования. Также исследована возможность нормализации магнитного поля воздушной линии с номинальным током 500 А. В этом случае металлоемкость решетчатого экрана увеличивается в 2,74 раза. Библ. 19, рис. 5, табл. 1.
Ключевые слова: **магнитное поле, воздушная линия электропередачи, решетчатый экран, предельно допустимый уровень, металлоемкость.**

Introduction. The Khrushchev era is known for its housing campaign. A vast number of housing square meters were built in USSR in sixties [1]. Usually these were five-story buildings made of prefabricated concrete blocks. That time the urban residential districts covered with such buildings (so-called Khrushchev buildings) appeared in many Soviet cities, especially industrial ones.

The overhead lines at voltages of 10 to 110 kV are laid to supply both residential districts and adjacent industrial areas. The size of the right-of-way is set up in regulations. For example, in Ukraine the right-of-way is 20 m for 110 kV overhead lines [2]. This corresponds with former Soviet requirements. At the same time, the requirements about the maximum permissible level (so-called reference level) of the power frequency magnetic field have changed significantly. The modern studies, particularly the "The International EMF Project" by the World Health Organization, have identified a high risk of the power frequency magnetic field for human health. It causes the world trend on stricter sanitary standards. Thus, Ukraine has accepted the reference level in 0.5 μT for living spaces [3]. However, most residential buildings found near 110 kV overhead lines do not meet this modern requirement. It is shown theoretically in [4, 5] and experimentally in [6], that the overhead line magnetic field exceeds the reference level. The degree of excess depends on the current flowing in conductors of the overhead line, the type of its tower, the distance from the overhead line to the building, and the height and the width of the building. Moreover, the power frequency magnetic field penetrates inside buildings with almost no attenuation [7, 8].

The purpose of this work is to find a way of the magnetic field normalization inside Khrushchev buildings found near 110 kV double-circuit overhead lines.

The most efficient way of the magnetic field normalization is to move away the source. But changes in overhead line routes are often impossible within the urban residential district. The reconstruction of the overhead line or its replacement by a high-voltage underground cable line requires significant costs. So, the most promising way of the magnetic field normalization inside residential buildings is shielding.

The various shields are used to normalize the magnetic field inside buildings found near overhead lines, namely electromagnetic shields [9, 10], passive loops [11, 12], and active loops [13, 14]. The active loops provide the comparably high shielding efficiency, but their price and expenses for maintenance checkup are relatively high as well. Passive loops are free of both these disadvantages, but their shielding efficiency is several times lower. Electromagnetic shields installed on building walls are most widely used to mitigate the magnetic field inside. However, electromagnetic shields consist of aluminum plates and therefore cannot cover windows. As well the mounting plates to the wall can cause difficulties.

A new type of shield is represented in [15, 16]. So-called grid shields consist of aluminum conductors connected in parallel. The recent research shows that grid shields are efficient for the magnetic field normalization inside high-rise buildings. But the magnetic field normalization inside five-story Khrushchev buildings was not studied.

Overhead line magnetic field inside Khrushchev building. Various series of five-story buildings were used during the Khrushchev housing campaign. However, the height and the width of the building did not change significantly. We assume that the height of the building is 16 m, and the width is 12 m [17]. In figures below the contour of the building is marked by the dotted line.

Within this research we consider the double-circuit overhead line magnetic field. In [16] we analyzed towers and found that geometric sizes of P110-4V tower (transliterated from *П110-4В*) are close to average ones. So, we assume the following values for the distances a_k from the tower to conductors and for the heights h_k of conductors: $a_1=a_6=2.1$ m, $h_1=h_6=19$ m, $a_2=a_5=4.2$ m, $h_2=h_5=23$ m, $a_3=a_4=2.1$ m, $h_3=h_4=27$ m, where subscripts correspond to numbers of overhead line conductors (Fig. 1). As mentioned before, the distance between the conductor no. 2 and the building is 20 m [2].

The overhead line magnetic field strongly depends on the configuration of initial phases of conductor currents and the current amplitude. We consider the case when the magnetic field is the highest. So, the initial phases are the following: $\varphi_1=\varphi_6=-2\pi/3$, $\varphi_2=\varphi_5=0$, $\varphi_3=\varphi_4=2\pi/3$. The RMS value of current in conductors is 262 A, which corresponds to the 110 kV double-circuit overhead line with transmission capacity 100 MW.

To find the overhead line magnetic field distribution, we use traditional assumptions, that conductors are infinitely long, parallel to each other and to the ground. So, we consider the overhead line magnetic field in the plane-parallel approach. This allows applying analytical expressions from [16] to find the magnetic field distribution inside the Khrushchev building. As well we can use the calculation technique from [18]. Fig. 1 shows that the magnetic field exceeds the reference level 0.5 μT in most part of the building. For quantitative assessment we use the normalization index η. It is defined as a ratio of the space, in which the magnetic field does not exceed the reference level, to the entire living space. As the magnetic field is plane-parallel, the normalization index η is the ratio of corresponding cross-sections S and S_0 [16].

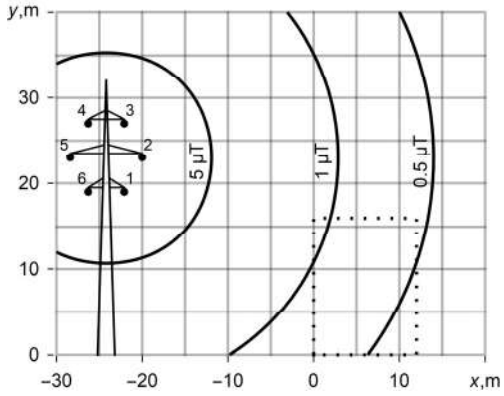

Fig. 1. Double-circuit overhead line magnetic field inside Khrushchev building (its contour is marked by dotted line)

According to [2], the areas closer than 0.5 m to walls are not considered. Also we do not consider the attic and the basement which are 1 m height. So, the cross-section of the building is $S_0=154$ m^2. Fig. 1 shows that the cross-section of space with permissible magnetic field is $S=16.8$ m^2. Correspondently, the normalization index η=10.9%.

Normalization of overhead line magnetic field. It is shown in [15, 16] that U-shaped grid shields are efficient for magnetic field normalization in high-rise buildings. However, the inverted L-shape looks more suitable for the lower Khrushchev building.

In the first step we consider grid shields with conductors on the wall faced to the overhead line and in the attic. The electrical conductivity of the grid shield is equal to $3.5\cdot10^7$ S/m. The distance between conductors is 0.5 m. The axe of the corner conductor has coordinates x=0, y=16 m. We vary the number of conductors on the wall up to 33. In the end case the conductors fill the whole wall and correspondently the extreme conductor has coordinates x=0, y=0. Also we vary the number of conductors in the attic up to 24. In this end case the extreme conductor has coordinates x=12 m, y=16 m. We use the following nomenclature when varying the cross-section of conductors: 5, 6, 8, 10, 16, 25, 35 and 50 mm^2. To analyze shielding efficiency in each case, we use both the finite-element model from [15] and the semi-analytical model from [19].

As the result we obtain the inverted L-shaped grid shield made of conductors with the cross-section of 25 mm^2. The total number of conductors is 53: the attic is covered by 24 conductors, and 29 conductors are on the wall. Correspondently the extreme conductor has coordinates x=0, y=2 m. The profile of conductor placement is shown in Fig. 2 by the solid line.

Fig. 2 shows that the shielded magnetic field exceeds the reference level 0.5 μT only in comparably small corner areas, and the normalization index η becomes 97.2%.

In the second step we use Wolfram Mathematica built-in functions of optimization to find the grid shield with the reduced quantity of metal while keeping the shielding efficiency. The obtained profile of the grid shield is shown in Fig. 3. The optimized grid shield consists of three sections connected in parallel.

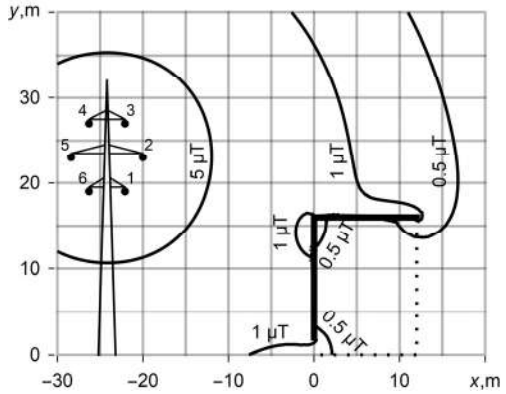

Fig. 2. Magnetic field distribution when using inverted L-shaped grid shield

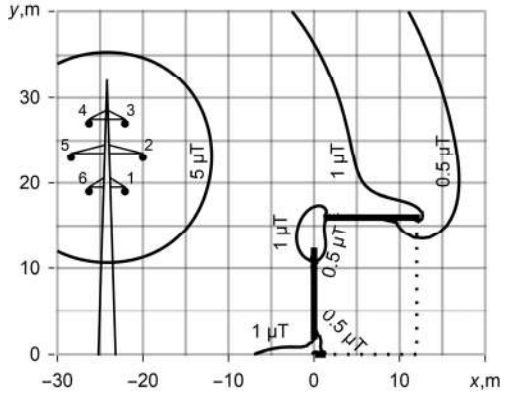

Fig. 3. Magnetic field distribution when using optimized grid shield

The section in the attic has 22 conductors arranged in the interval 1.5 m $\le x \le$ 12 m when y=16 m. The section on the wall has 21 conductors in the interval 2 m $\le y \le$ 12 m when x=0. Also there are two conductors in the basement. Their coordinates are x=0.5 m, y=0 and x=1 m, y=0. The total number of conductors is 45. The cross-section of each conductor is 25 mm^2. The quantity of metal of the optimized grid shield we appoint as V_1. The analysis of the magnetic field distribution from Fig. 3 gives the normalization index η=97.1%. So, the optimized grid shield allows reducing the quantity of metal by 15 percent in comparison with inverted L-shaped grid shield.

We study the efficiency of the optimized grid shield varying its quantity of metal (see column *a* in Table 1). Also we compare it with efficiencies of grid shields having the following profiles (as before the distance between conductors is 0.5 m):

- the inverted L-shaped grid shield (made of 45 conductors) with 16 m height vertical section and 6 m long upper horizontal section (see column *b* in Table 1);
- the inverted L-shaped grid shield (made of 57 conductors) with 16 m height vertical section and 12 m long upper horizontal section (see column *c*);
- the U-shaped grid shield (made of 69 conductors) with 16 m height vertical section, 12 m long upper horizontal section, and 6 m long bottom horizontal section (see column *d*);
- the U-shaped grid shield (made of 81 conductors) with 16 m height vertical section and 12 m long horizontal sections (see column *e*).

Table 1

Normalization index η for Khrushchev building found near double-circuit overhead line when using grid shield with quantity of metal equaled V

V/V_1	η, %				
	a	*b*	*c*	*d*	*e*
0.25	25.4	20.6	21.5	22.2	19.4
0.5	70.7	46.9	54.8	43.7	36.2
0.75	92.8	60.7	85.2	72.6	58.8
1	97.1	68.4	95.2	89.2	82.8
1.25	98.5	73.8	98.1	95.5	92.2

As grid shields *a-e* contain different number of conductors, we consider different conductor cross-sections to achieve the equality of total quantities of metal.

The obtained results show that efficiencies of the optimized shield and the grid shield type *c* are comparable. However, the practical implementation of the grid shield type *c* is difficult as it uses conductors with off-standard cross-section 19.7 mm^2. So, the usage of the optimized grid shield is recommended. Table 1 shows that the increase or the decrease of its quantity of metal is impractical.

Overhead line with increased conductor current. Additionally, we consider the overhead line magnetic field normalization when the conductor current is 500 A [5, 11]. In this case the magnetic field exceeds the reference level 0.5 μT in the whole building (Fig. 4). Moreover, the fourfold magnetic field mitigation is needed in apartments faced to the overhead line. To normalize the magnetic field, we develop the grid shield made of 62 conductors (Fig. 5). The cross-section of each conductor is 50 mm^2. Correspondently the quantity of metal of the shield is 2.74·V_1. The distance between conductors is 0.5 m. The arrangement of conductors is the following:

- 27 conductors cover the wall faced to the overhead line (their coordinates lay within the interval 1 m $\le y \le$ 14 m when x=0);
- 11 conductors are arranged on the back wall (within the interval 11 m $\le y \le$ 16 m when x=12 m);
- 22 conductors cover the attic (within the interval 0.5 m $\le x \le$ 11 m when y=16 m);
- 2 conductors lay in the basement (in x=0.5 m, y=0 and x=1 m, y=0).

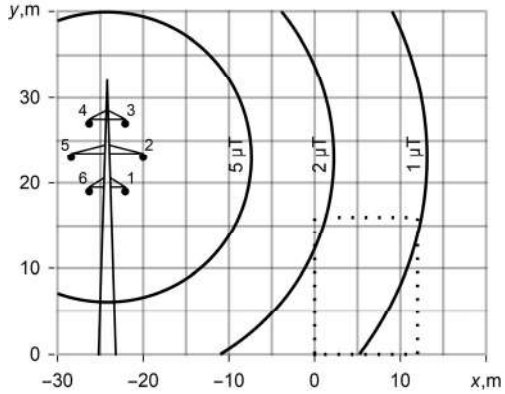

Fig. 4. Double-circuit overhead line magnetic field when conductor current is 500 A

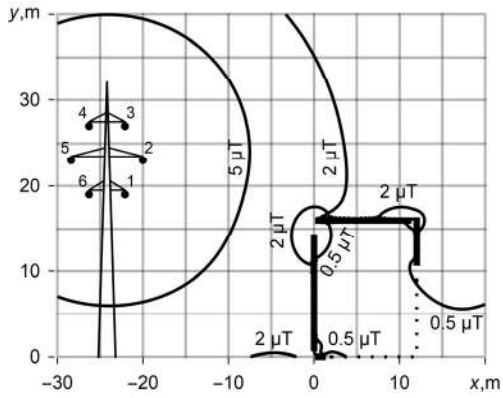

Fig. 5. Normalization of double-circuit overhead line magnetic field when conductor current is 500 A

The usage of this grid shield allows to achieve the normalization index η=97.1%. Fig. 5 shows the distribution of the normalized magnetic field inside the Khrushchev building.

So, the obtained results show that grid shields are efficient in the magnetic field normalization inside Khrushchev buildings found near the overhead lines.

Conclusions.

1. Using the analytical model of the shield and the numerical simulation, we show that the inverted L-shaped grid shield made of aluminum conductors with a cross-section of 25 mm^2 and mounted on the wall and in the attic of the Khrushchev building normalizes inside it the magnetic field produced by the 110 kV double-circuit overhead line.

2. We propose the specific grid shield that provides the shielding efficiency of the L-shaped shield and consumes the quantity of metal reduced by 15 percent. This shield consists of three sections of conductors, namely two sections cover the wall and the attic of the Khrushchev building, and two extra conductors are placed in the basement.

3. To normalize the 110 kV double-circuit overhead line magnetic field with increased conductor current, we modify the arrangement of conductors on the wall faced to the line and in the attic, we add the extra section of conductors to the back wall and increase the cross-section of all conductors to 50 mm^2.

Conflict of interest. The authors declare that they have no conflicts of interest.

REFERENCES

1. Reid S. Khrushchev Modern: Agency and modernization in the Soviet home. *Cahiers du monde russe*, 2006, no. 47, iss. 1, pp. 227-268. doi: https://doi.org/10.4000/monderusse.3800.

2. Decree of the Cabinet of Ministries of Ukraine dated March 4, 1997 No. 209 *«About the statement of Rules of protection of electric networks»*, Edition on April 5, 2017. (Ukr).

3. Electrical installation regulations. Kharkiv, Fort Publ., 2017. 760 p. (Ukr).

4. Rozov V.Yu., Reutskyi S.Yu., Pelevin D.Ye., Pyliugina O.Yu. The magnetic field of power transmission lines and the methods of its mitigation to a safe level. *Technical Electrodynamics*, 2013, no. 2, pp. 3-9. (Rus).

5. Pelevin D.Ye. The methods of reducing of the magnetic fields of overhead power lines outside security zones. *Technical Electrodynamics*, 2014, no. 5, pp. 14-16. (Rus).

6. Krasnozhon A.V., Buinyi R.O., Dihtyaruk I.V., Kvytsynskyi A.O. The investigation of distribution of the magnetic flux density of operating two-circuit power line 110 kV «ChTPP-Chernihiv-330» in the residential area and methods of its decreasing to a safe level. *Electrical Engineering & Electromechanics*, 2020, no. 6, pp. 55-62. doi: https://doi.org/10.20998/2074-272X.2020.6.08.

7. Pelevin D.Ye. Screening magnetic fields of the power frequency by the walls of houses. *Electrical Engineering & Electromechanics*, 2015, no. 4, pp. 53-55. (Rus). doi: https://doi.org/10.20998/2074-272X.2015.4.10.

8. Rozov V., Grinchenko V. Simulation and analysis of power frequency electromagnetic field in buildings closed to overhead lines. *Proc. 2017 IEEE First Ukraine Conference on Electrical and Computer Engineering*, Kyiv, Ukraine, pp. 500-503. doi: https://doi.org/10.1109/UKRCON.2017.8100538.

9. Cardelli E., Faba A., Pirani A. Nonferromagnetic open shields at industrial frequency rate. *IEEE Transactions on Magnetics*, 2010, vol. 46, no. 3, pp. 889-898. doi: https://doi.org/10.1109/TMAG.2009.2031110.

10. Bavastro D., Canova A., Freschi F., Giaccone L., Manca M. Magnetic field mitigation at power frequency: Design principles and case studies. *IEEE Transactions on Industry Applications*, 2015, vol. 51, no. 3, pp. 2009-2016. doi: https://doi.org/10.1109/TIA.2014.2369813.

11. Cruz P., et al. Magnetic field mitigation in power lines with passive and active loops. *Proc. CIGRE Session*, 2002, no. 36-107.

12. Budnik K., Machczynski W. Power line magnetic field mitigation using a passive loop conductor. *Poznan University of Technology Academic Journals. Electrical Engineering*, 2013, vol. 73, pp. 137-145.

13. Canova A., del-Pino-Lopez J.C., Giaccone L., Manca M. Active shielding system for ELF magnetic fields. *IEEE Transactions on Magnetics*, 2015, vol. 51, iss. 3. doi: https://doi.org/10.1109/TMAG.2014.2354515.

14. Kuznetsov B.I., Nikitina T.B., Bovdui I.V. High voltage power lines magnetic field system of active shielding with compensation coil different spatial arrangement. *Electrical Engineering & Electromechanics*, 2019, no. 4, pp. 17-25. doi: https://doi.org/10.20998/2074-272X.2019.4.03.

15. Grinchenko V., Pyrohova U. Mitigation of overhead line magnetic field by U-shaped grid shield. *Proc. 2019 IEEE Second Ukraine Conference on Electrical and Computer Engineering*, Lviv, Ukraine, pp. 345-348. doi: https://doi.org/10.1109/UKRCON.2019.8879834.

16. Grinchenko V.S., Chunikhin K.V. Magnetic field normalization in residential building located near overhead line by grid shield. *Electrical Engineering & Electromechanics*, 2020, no. 5, pp. 38-43. doi: https://doi.org/10.20998/2074-272X.2020.5.06.

17. Koporovskii G.I., et al. *Typical project 111-96-3. Residential buildings series 96*. Kyiv, KyivZNIIEP Publ. (Rus).

18. *SOU-N EE 20.179:2008. Calculation of electric and magnetic fields of power lines. Method (with changes)*. Kyiv, Minenergovugillja Ukrainy Publ., 2016. 37 p. (Ukr).

19. Grinchenko V.S. Development of a semi-analytical model of a grid shield for the magnetic field mitigation of overhead lines. *Proc. VII All-Ukrainian Scientific Conf. of Young Scientists «Information Technologies – 2020»*, pp. 149-151. (Ukr).

Received 08.04.2021
Accepted 14.05.2021
Published 25.06.2021

K.V. Chunikhin[1]*, PhD,*
V.S. Grinchenko[1]*, PhD,*
[1] State Institution "Institute of Technical Problems of Magnetism of the National Academy of Sciences of Ukraine",
19, Industrialna Str., Kharkiv, 61106, Ukraine,
e-mail: kvchunikhin@gmail.com,
vsgrinchenko@gmail.com (Corresponding author)

How to cite this article:
Chunikhin K.V., Grinchenko V.S. Normalization of double-circuit overhead line magnetic field inside Khrushchev building. *Electrical Engineering & Electromechanics*, 2021, no. 3, pp. 38-41. doi: https://doi.org/10.20998/2074-272X.2021.3.06.

UDC 621.3.: 621. 039.667 https://doi.org/10.20998/2074-272X.2021.3.07

L.A. Ljutenko, V.M. Mikhailov

EXPANSION OF CYLINDRICAL TUBULAR WORKPIECES ON HIGH-VOLTAGE MAGNETIC-PULSE INSTALLATION WITH CONTROLLED VACUUM DISCHARGER

Purpose. *An experimental verification of the existence of a range of values for the parameters of the capacitive energy storage of the magnetic-pulse installations with controlled vacuum discharger, in which, with a high probability, there is a «cut» of the discharge current pulses and the expansion of cylindrical thin-walled tubular workpieces using an external coil.* ***Methodology***. *High voltage magnetic-pulse installation of NTU «KhPI» with controlled vacuum discharger, multiturn coil with inside dielectrical die and inside aluminum alloy workpiece are used. The capacitance and charge voltage of capacitive energy storage are changed. Discharge current pulses are measured by Rogowski coil and the oscillograph.* ***Results***. *Parts of complicated shape are made by expansion of cylindrical tubular workpieces with help of external coil. Pressed metallic tubular part is removable from inner dielectric rod.* ***Originality***. *The frequency of «cut» pulse is defined by negative magnetic field pressure amplitude. It is shown that we must coordinate this frequency and charge voltage with capacitive storage parameters by high probability of pulse «cut».* ***Practical value***. *It is shown how to use installations with controlled vacuum dischargers in magnetic forming technology based on «cut» pulses.* References 17, tables 2, figures 5.

Key words: **high-voltage magnetic-pulse installations, capacitive energy storage, controlled vacuum discharger, current pulse «cut», probability of «cut», external coil, expansion of cylindrical tubular workpiece, part of complicated shape.**

Мета. *Метою роботи є експериментальна перевірка існування зони параметрів ємнісного нагромаджувача енергії магнітно-імпульсної устатковини з керованим вакуумним розрядником, в котрій з високою імовірністю відбувається «зріз» імпульсів розрядного струму та розширення циліндричних тонких трубчастих заготівок за допомогою зовнішнього індуктора.* ***Методика***. *Використано високовольтну магнітно-імпульсну устатковину НТУ «ХПІ» з керованим вакуумним розрядником та багатовитковий індуктор, усередині котрого було розміщено діелектричну матрицю і заготівку з алюмінієвого стопу. Змінювали ємність та зарядну напругу нагромаджувача енергії. Імпульси розрядного струму вимірювали за допомогою поясу Роговського та реєстрували осцилографом.* ***Результати***. *Магнітно-імпульсним розширенням циліндричних заготівок за допомогою зовнішнього індуктора отримано деталі складної форми та здійснено зняття металевої деталі, що була напресована на діелектричний стрижень.* ***Наукова новизна***. *Показано, що частоту імпульсу, що «зрізається», при котрій амплітуда від'ємного тиску магнітного поля наближається до максимальної, а також зарядну напругу необхідно узгоджувати з параметрами ємнісного нагромаджувача енергії, при яких з високою імовірністю відбувається «зріз» імпульсу.* ***Практичне значення***. *Результати та рекомендації, що отримано, можуть бути використано у магнітно-імпульсних технологіях на устатковинах з керованими вакуумними розрядниками.* Бібл. 17, табл. 2, рис. 5.

Ключові слова: **високовольтна магнітно-імпульсна устатковина, ємнісний нагромаджувач енергії, керований вакуумний розрядник, «зріз» імпульсу струму, імовірність «зрізу», зовнішній індуктор, розширення циліндричної трубчатої заготівки, деталь складної форми.**

Цель. *Целью работы является экспериментальная проверка существования области значений параметров емкостного накопителя энергии магнитно-импульсной установки с управляемым вакуумным разрядником, в которой с высокой вероятностью происходит «срез» импульсов разрядного тока и расширение цилиндрических тонкостенных трубчатых заготовок при помощи внешнего индуктора.* ***Методика***. *Эксперименты были проведены на высоковольтной магнитно-импульсной установке НТУ «ХПИ», оснащенной управляемым вакуумным разрядником. Использовали многовитковый индуктор, внутрь которого помещалась диэлектрическая матрица и заготовка из алюминиевого сплава. Изменяли емкость и зарядное напряжение накопителя энергии. Импульсы разрядного тока измеряли при помощи пояса Роговского и регистрировали на осциллографе.* ***Результаты***. *Магнитно-импульсным расширением цилиндрических заготовок при помощи внешнего индуктора получены детали сложной формы и осуществлено снятие металлической детали, напрессованной на диэлектрический стержень.* ***Научная новизна***. *Показано, что частоту «срезаемого» импульса, при которой амплитуда отрицательного давления магнитного поля близка к максимальной, а также зарядное напряжение необходимо согласовывать с параметрами емкостного накопителя энергии, при которых с высокой вероятностью происходит «срез» импульса.* ***Практическое значение***. *Получены рекомендации для использования в магнитно-импульсных технологиях, основанных на применении «срезанных» импульсов, установок с управляемыми вакуумными разрядниками.* Библ. 17, табл. 2, рис. 5.

Ключевые слова: **высоковольтная магнитно-импульсная установка, емкостной накопитель энергии, управляемый вакуумный разрядник, «срез» импульса тока, вероятность «среза», внешний индуктор, расширение цилиндрической трубчатой заготовки, деталь сложной формы**.

Introduction. When performing various technological operations on magnetic-pulse installations (MPIs), workpieces in the form of thin-walled cylindrical pipes made of highly conductive metals are used [1-8]. Below, we restrict ourselves to operations based on the expansion of cylindrical workpieces of small diameter, as well as ones inaccessible from the inside. In such cases, the use of an internal coil is difficult or impossible.

In 1965, H. Furth received a patent for devices that allows magnetic-pulse processing of cylindrical and flat-sheet workpieces by the forces of attraction to the coil [9].

The principle of operation of these devices is based on a controlled «cut» of current pulses in the discharge circuit of a capacitive energy storage (CES). In this case, eddy currents are induced in the workpiece, causing it to be attracted to the coil. For the «cut» it is proposed to use a fusible element or an additional capacitive storage, and to enhance the effect – an additional conductor. The «cut» of the current pulses allows the cylindrical workpieces to be expanded by the magnetic field of an external coil. In one of the first works [10], the authors registered the expansion of the workpiece using an external coil. In this case, both the oscillatory and the aperiodic discharge of the CES were used [10, Fig. 4], and compression of the workpiece was prevented by an inner cylindrical mandrel. In the works of recent years, the use of a system of two coils has been proposed, through which various current pulses are passed [6], as well as the effect of two pulses of different durations, passed through one coil [7].

When using in the MPI for switching the CES of controlled vacuum dischargers (CVD), there is a natural (without additional devices [9]) «cut» of the oscillatory pulses of the discharge current (Fig. 1,*a*) [11, 12]. In the experiments that were carried out at NTU «KhPI» [12], attention was drawn out to the probabilistic nature of the appearance of «cut» pulses under the same conditions. In the case of a «cut» of the pulse, the negative half-wave of pressure of the magnetic field expands the workpiece 1 (pos. 1 in Fig. 1,*c*), and at full (not «cut») pulse (Fig. 1,*b*) after that it is compressed (pos. 2 in Fig. 1,*c*). Therefore, the determination of the parameters of the CES, at which the CVD with a high probability «cuts» discharge current pulses is an urgent problem. Some of the first results of our studies of this phenomenon and the corresponding recommendations for obtaining «cut» pulses were presented in [13].

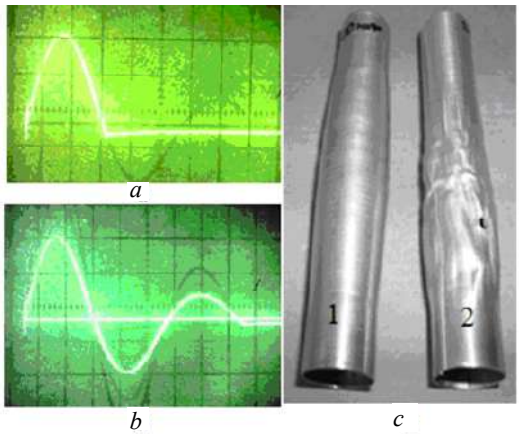

Fig. 1. «Cut» (*a*) and full (*b*) discharge current pulses (50 μs/div), as well as workpieces 1 and 2, respectively (*c*), deformed by them

On the other hand, the parameters of the «cut» pulse significantly affect the amplitude of the negative half-wave of the magnetic field pressure, which expands the workpiece [14-16]. The coordination of the parameters of this pulse with the characteristics of the material and the dimensions of the workpiece has not been sufficiently studied, and the probabilistic nature of the «cut» was not taken into account.

The purpose of this work is an experimental verification of the existence of a range of values for the parameters of the capacitive energy storage of the magnetic-pulse installations with controlled vacuum discharger, in which, with a high probability, there is a «cut» of the discharge current pulses and the expansion of cylindrical thin-walled tubular workpieces using an external coil.

Equipment used in experiments. The CES of the MPI designed at NTU «KhPI» consisted of capacitors IK6-150 and allowed to change the capacitance C = 600–1200 μF. The CES charging voltage U_0 = 1,5–6 kV. The CES was discharged to the coil (Fig. 2) through the RVU–63–20–UHL4 type CVD produced by the Minusinsk Electrotechnical Institute. The winding of the coil 1, which has the shape of a cylindrical spiral made of a copper bus, was connected to the MPI using leads 2 and contact nodes 3. The position of the processed metal workpiece 4 inside the coil was fixed by a dielectric die 5 and a dielectric rod 6, which also prevents compression of the workpiece. Tubular cylindrical billets of AMg2M aluminum alloy with specific electrical conductivity $\gamma = 0.27 \cdot 10^8$ S/m had an inner radius R = 8 mm and a thickness d = 0.5 mm.

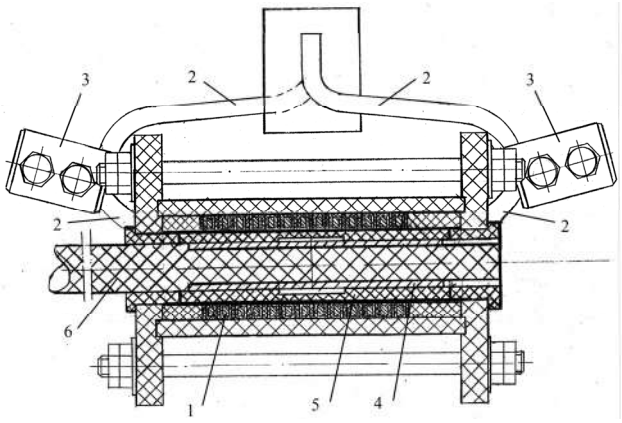

Fig. 2. Coil for magnetic-pulse expansion of cylindrical tubular workpieces

The discharge current pulses were measured using a Rogowski coil with an *RC* integrator and recorded on an S8-13 oscilloscope. The total current pulses had a shape close to an exponentially decaying sinusoid (Fig. 1,*b*).

CES parameters providing a high probability of current pulses «cut». To determine C, U_0, at which there is a «cut» of the discharge current pulses, instead of die 5 (Fig. 2) a dielectric sleeve was used to prevent expansion of the workpiece. The probability of the appearance of «cut» pulses was characterized by the probabilistic frequency N_c/N (N_c is the number of «cut» pulses, N is the total number of pulses). Table 1 shows more detailed than in work [13], the results of tests of the CVD (I_{m1} is the amplitude value of the current). After that these data were used to determine the parameters of the CES when performing technological operations.

Table 1

Amplitude values and probabilistic frequency of the «cut» of the discharge current pulses

U_0, kV	C, μF											
	600			750			900			1200		
	I_{m1}, kA	N	N_c/N	I_{m1}, kA	N	N_c/N	I_{m1}, kA	N	N_c/N	I_{m1}, kA	N	N_c/N
1,5	18	6	1	21	7	1	25	6	1	30	6	1
2	24	6	1	28	6	1	32	6	1	36	6	1
2,34	29	7	1	32	6	1	38	6	1	42	6	1
2,7	32	18	0,94	37	6	1	43	6	0,83	50	6	1
3,4	42	30	0,8	46	6	0,83	50	6	0,83	56	6	0,5
3,8	47	32	0,8	51	6	0,83	54	6	0,83	62	6	0
4,25	52	27	0,78	57	12	0,5	60	6	0,5	67	6	0
4,65	57	10	0,2	61	6	0	64	8	0	–	–	–

Determination of the frequency of the «cut» pulse of the discharge current. The frequency of the «cut» pulse, which can be provided by the MPI, must be matched with the electrophysical characteristics and dimensions of the workpiece. For this we use the generalized similarity criterion $\tau^* = \omega\tau$ [15], where ω is the circular frequency, τ is the time constant of the first approximation, $\tau = \mu_0 \cdot \gamma \cdot R \cdot d/2$, μ_0 is the magnetic constant. The generalized criterion τ^* comprehensively takes into account the electrophysical characteristics (μ_0, γ) and dimensions (R, d) of a thin workpiece, and also replaces two criterions $d^* = d/\Delta$ and $d_R^* = d/R$ (Δ is the penetration depth of the electromagnetic field [17]). In a wide range of values of the damping coefficient of an exponentially damped sinusoid, the optimal value of the generalized criterion τ^*, at which the amplitude of the negative pressure P_{m2}, acting on the workpiece, is maximum, is $\tau_0^* = 0{,}8$. Here, in the range

$$0{,}5 \le \tau^* \le 1{,}4 \qquad (1)$$

the value of P_{m2} changes insignificantly [15, Fig. 4, curves 5–8].

Condition (1) is universal and is valid for thin cylindrical workpieces made of non-magnetic materials. For the workpieces used in the experiments described here (τ = 67,858 μs), from condition (1) we obtain the corresponding ranges of the recommended values of ω (1/s) and frequency f (kHz) of the «cut» pulse

$$7368 \le \omega \le 20631, \qquad (2)$$

$$1{,}173 \le f \le 3{,}284, \qquad (3)$$

and also the criterion d^*

$$0{,}1768 \le d^* \le 0{,}2958. \qquad (4)$$

Values ω, f, d^*, corresponding to τ_0^*, equal to ω_0 = 11789 1/s, f_0 = 1,876 kHz, d_0^* = 0,2236.

Table 2 shows the values of the half-period duration $T/2$, ω, f obtained from the oscillograms of the current in the discharge circuit of the MPI, as well as of the criteria τ^* and d^*.

Analysis of data of Table 2, taking into account conditions (2)–(4), allows us to conclude that the MPI with a CES capacity C = 900 or 1200 μF provides the recommended frequencies of the «cut» pulse, at which the amplitude of the negative pressure of the pulsed magnetic field expanding the workpiece with the help of an external coil, is close to the maximum value.

Table 2

Time and frequency parameters of the «cut» pulses of the discharge current and the values of the criteria τ^*, d^*

C, μF	$T/2$, μs	$\omega/10^3$, 1/s	f, kHz	τ^*	d^*
600	130	24,17	3,846	1,638	0,32
750	150	20,94	3,333	1,44	0,30
900	160	19,63	3,124	1,346	0,29
1200	200	15,71	2,500	1,082	0,26

Technological operations based on the expansion of tubular workpieces by «cut» pulses. When performing the described technological operations, it was taken C = 900 μF, U_0 = 3.2 kV. The value of U_0 was selected experimentally from the condition of achieving sufficient deformation of the workpiece. These parameters of the CES provide both a high probability of «cut» pulses (Table 1), and the recommended frequency of the «cut» pulse (Table 2, conditions (2), (3)).

Manufacturing of parts with complex shapes. Figure 3 shows drawings of a part with one cylindrical protrusion (*a*) and a corresponding collapsible dielectric die (*b*) (see also pos. 5 in Fig. 2), and Fig. 4,*a* shows parts made from a tubular workpiece using «cut» pulses. The part can have a more complex shape, which is determined by the shape of the dielectric die, for example, it can have two cylindrical protrusions (Fig. 4,*b*).

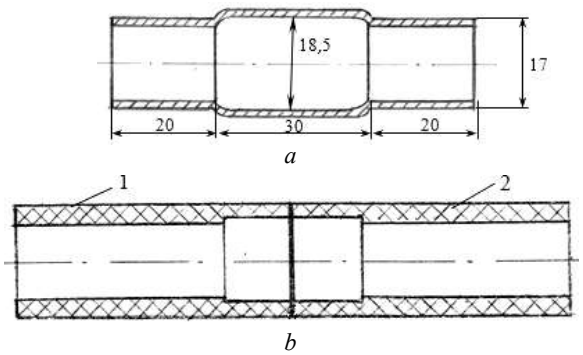

Fig. 3. Drawings of a part with one cylindrical protrusion (*a*) and a collapsible dielectric die (*b*, where 1, 2 – symmetrical parts of the die)

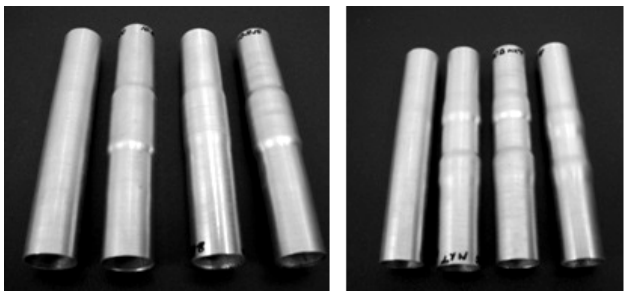

a *b*

Fig. 4. Parts with one (*a*) and two (*b*) cylindrical protrusions, made using «cut» pulses

Removing the metal tubular part from a dielectric rod. A tubular part made of aluminum alloy was pressed onto a dielectric rod of circular cross-section using a pre-machined groove by magnetic-pulse compression (Fig. 5,*a*). To remove this part (for the purpose of replacement), a «cut» pulse of the discharge current was used, and instead of die 5 (Fig. 2) – a dielectric sleeve allowing sufficient radial expansion of the removed part (~ 0.5 mm). Figure 5,*b* shows workpiece 1 before pressing on the rod and parts removed in the described way (2, 3).

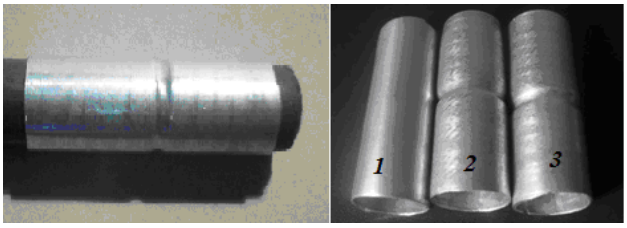

a *b*

Fig. 5. Permanent joint of a dielectric rod and a tubular metal part (*a*), a workpiece and parts removed by «cut» pulses (*b*)

The need to remove the outer technological conductive shells arises after the magnetic-pulse pressing of parts made of powder materials. If the part has a tubular shape and is accessible from the inside, then this operation can be carried out using an internal coil. The experimental results presented in this article confirm the possibility of removing the technological shell from tubular and solid cylindrical parts made of powder materials using an external coil and «cut» pulses. Note that in [16], it was noted that such an operation can be performed in the case of a cylinder made of a powder material by the second pulse of the magnetic field.

The studies carried out show that one «cut» pulse is enough: in this case, with the help of the first, positive, half-wave of pressure, the part is pressed, and with the help of the second, negative one, the technological shell is removed.

Conclusions.

1. With the help of technological operations based on the magnetic-pulse expansion of cylindrical tubular workpieces with an external coil, the existence of a range of values of the parameters of the capacitive energy storage with controlled vacuum discharger was confirmed, in which the discharge current pulses are «cut» with a high probability.

2. Before performing technological operations based on expanding workpieces using an external coil, it is necessary to test the controlled vacuum discharger and determine the values of the capacitance and charging voltage of the energy storage, at which the relative probability of the «cut» of the discharge current pulses is close to 1.

3. The recommended frequency of the «cut « pulse of the discharge current, at which a close to optimal amplitude of negative pressure expanding the workpiece is achieved, can be determined from the conditions obtained using the generalized similarity criterion.

4. The charging voltage of the storage capacity is selected experimentally from the condition of achieving the required deformation of the workpiece and is coordinated with the test data of the controlled vacuum discharger.

5. Magnetic-pulse pressing of tubular and solid cylindrical parts made of powder materials and then removing the technological conductive shell can be carried out with one «cut» current pulse.

Conflict of interest. The authors declare that they have no conflicts of interest.

REFERENCES

1. Bely I.V., Fertik S.M., Khimenko L.T. *Spravochnik po magnitno-impulsnoj obrabotke metallov* [Handbook on magnetic-pulse processing of metals]. Kharkiv, Vishcha shkola Publ., 1977, 168 p. (Rus).

2. Psyk V., Risch D., Kinsey B.L., Tekkaya A.E., Kleiner M. Electromagnetic forming – A review. *Journal of Materials Processing Technology*, 2011, vol. 211, no. 5, pp. 787-829. doi: https://doi.org/10.1016/j.jmatprotec.2010.12.012.

3. Qiu L., Yu Y., Yang Y., Nie X., Xiao Y., Ning Y., Wang F., Cao C. Analysis of electromagnetic force and experiments in electromagnetic forming with local loading. *International Journal of Applied Electromagnetics and Mechanics*, 2018, vol. 57, no. 1, pp. 29-37. doi: https://doi.org/10.3233/jae-170038.

4. Zhang X., Li C., Wang X., Zhao Y., Li L. Improvement of deformation behavior of tube in electromagnetic forming with a triple-coil system. *International Journal of Applied Electromagnetics and Mechanics*, 2019, vol. 61, no. 2, pp. 263-272. doi: https://doi.org/10.3233/jae-180122.

5. Prokofiev A.B., Beliaeva I.A., Glushchenkov V.A., Karpukhin V.F., Chernikov D.G., Iusupov R.Iu. *Magnitno-impul'snaia obrabotka materialov* [Magnetic-pulse processing of materials]. Samara, SNTs Publ., 2019. 140 p, Available at: http://repo.ssau.ru/handle/Monografii/Magnitnoimpulsnaya-obrabotka-materialov-MIOM-Elektronnyi-resurs-monografiya-81514 (accessed 15 May 2020). (Rus).

6. Li X., Cao Q., Lai Z., Ouyang S., Liu N., Li M., Han X., Li L. Bulging behavior of metallic tubes during the electromagnetic forming process in the presence of a background magnetic field. *Journal of Materials Processing Technology*, 2020, vol. 276, p. 116411. doi: https://doi.org/10.1016/j.jmatprotec.2019.116411.

7. Xiong Q., Yang M., Tang H., Huang H., Song X., Qiu L., Yu K., Cao Q. Flaring Forming of Small Tube Based on Electromagnetic Attraction. *IEEE Access*, 2020, vol. 8, pp. 104753-104761. doi: https://doi.org/10.1109/access.2020.2999125.

8. Chernikov D.G., Glushchenkov V.A., Gusev D.V., Pfetzer I.A., Alyokhina V.K. Evaluation of the efficiency of the process of electromagnetic forming of small-diameter tubes. *Izvestiya of Samara Scientific Center of the Russian Academy of Sciences*, 2020, vol. 22, no. 4, pp. 21-28. (Rus). doi: https://doi.org/10.37313/1990-5378-2020-22-4-21-28.

9. Furth Harold P. *Devices for metal-forming by magnetic tension*. Patent USA no. 3,196,649, July, 27, 1965.

10. Shcheglov B.A., Esin A.A. Distribution of thin-walled tubular workpieces by the forces of attraction of a pulsed magnetic field. *Forging and Stamping Production. Material Working by Pressure*, 1971, no. 4, pp. 15-17. (Rus).
11. Yusupov R.Yu. Magnetic-pulse installations of a new generation for industrial and educational-scientific purposes. *Proceedings of the International Scientific and Technical Conference MIOM-2007*, 2007, pp. 251-259. (Rus).
12. Bondina N.N., Konovalov O. Ya., Legeza A.V., Makeev V.G., Mikhailov V.M., Shovkoplyas A.V. Magnetic-pulse expansion of a cylindrical conducting shell and creation of a given distribution fields using an external coil. *Technical electrodynamics. Thematic issue «Problems of modern electrical engineering»*, 2008, chapter 5, pp. 84-89. (Rus).
13. Ljutenko L.A., Mikhailov V.M. The probability of interruption current pulses in circuit of capacitor bank with vacuum discharger. *Technical electrodynamics*, 2012, no. 3, pp. 121-122. (Rus).
14. Ljutenko L.A., Mikhailov V.M. Influence of the shape of an external magnetic field pulse on electrodynamic forces deforming a cylindrical shell. *Technical electrodynamics*, 2007, no. 6, pp. 15-19. (Rus).
15. Bondina N.N., Kramchanin E.G., Ljutenko L.A., Mikhailov V.M. Electrodynamic forces acting on a cylindrical shell under oscillating discharge of a magnetic pulse forming machine. *Electrical Engineering & Electromechanics*, 2007, no. 5, pp. 66-70. (Rus).
16. Boltachev G.Sh., Volkov N.B., Paranin S.N., Spirin A.V. Dynamics of cylindrical conducting shells in a pulsed longitudinal magnetic field. *Technical Physics*, 2010, vol. 55, no. 6, pp. 753-761. doi: https://doi.org/10.1134/S1063784210060010.
17. Neyman L.R., Demirchyan K.S. *Teoreticheskie osnovy elektrotechniki. V 2-h tomah. Tom 2* [Theoretical bases of the Electrical Engineering. In 2 vols. Vol. 2]. Leningrad, Energoizdat Publ., 1981. 416 p. (Rus).

Received 15.04.2021
Accepted 24.05.2021
Published 25.06.2021

L.A. Ljutenko[1],
V.M. Mikhailov[1], *Doctor of Technical Science, Professor,*
[1] National Technical University «Kharkiv Polytechnic Institute», 2, Kyrpychova Str., Kharkiv, 61002, Ukraine,
e-mail: lutenkola@gmail.com,
valery.m.mikhailov@gmail.com (Corresponding author)

How to cite this article:
Ljutenko L.A., Mikhailov V.M. Expansion of cylindrical tubular workpieces on high-voltage magnetic-pulse installation with controlled vacuum discharger. *Electrical Engineering & Electromechanics*, 2021, no. 3, pp. 42-46. doi: https://doi.org/10.20998/2074-272X.2021.3.07.

UDC 621.319 https://doi.org/10.20998/2074-272X.2021.3.08

G.V. Bezprozvannych, I.A. Kostiukov

A CALCULATION MODEL FOR DETERMINATION OF IMPEDANCE OF POWER HIGH VOLTAGE SINGLE-CORE CABLES WITH POLYMER INSULATION

Introduction. *The wave parameters of power cables with polymer insulation differ significantly from the parameters of overhead lines and power transformers. As a result, there are more and more objects in electrical networks for which the occurrence of complex multi frequency transients, accompanied by dangerous overvoltages, should be expected.* ***Purpose.*** *To develop a computational model of the complex impedance of high-voltage single-core power cables of coaxial design required to determine the frequency dependencies of the active resistance and inductance of the conductive core and metal shield, taking into account the surface effect and proximity effect.* ***Methodology.*** *The method is based on solving a system of linear algebraic Kirchhoff equations (SLAE) for magnetically coupled contours. SLAE can be used to calculate conductors taking into account the skin effect and proximity effect.* ***Practical value.*** *The developed model is the basis for determining the characteristic impedance of high-voltage single-core power cables in a wide range of frequencies required to establish adequate criteria for evaluating the parameters of high-frequency effects critical for cross linked polyethylene insulation.* References 16, table 1, figures 7.

Key words: **power cables, complex resistance, magnetically coupled circuits, system of linear algebraic equations, conductor, screen, coefficient of irregularity of current distribution.**

Запропонована чисельна розрахункова модель визначення активного опору та індуктивності струмопровідної жили й металевого екрану силових одножильних кабелів коаксіальної конструкції з урахуванням поверхневого ефекту та ефекту близькості в широкому діапазоні частоти. Виконано в залежності від частоти порівняння коефіцієнтів нерівномірності розподілу струму по перетину струмопровідної жили кабелю. Показано, що збільшення товщини мідного екрану призводить до збільшення коефіцієнта нерівномірності розподілу струму по перерізу екрану та активного опору кабелю для частоти 100 кГц при незмінному перерізі струмопровідної жили. Розроблена модель є основою для визначення характеристичного імпедансу силових високовольтних одножильних кабелів в широкому діапазоні частоти, необхідного для встановлення адекватних критеріїв оцінки параметрів високочастотних впливів, критичних для зшитої поліетиленової ізоляції. Бібл. 16, табл. 1, рис. 7.

Ключові слова: **силові кабелі, комплексний опір, магнітозв'язані контури, система лінійних алгебраїчних рівнянь, струмопровід, екран, коефіцієнт нерівності розподілу струму.**

Предложена численная расчетная модель определения активного сопротивления и индуктивности токопроводящей жилы и экрана силовых одножильных кабелей коаксиальной конструкции с учетом поверхностного эффекта и эффекта близости в широком диапазоне частоты. Выполнено в зависимости от частоты сравнение коэффициентов неравномерности распределения тока по сечению токопровода. Показано, что увеличение толщины медного экрана приводит к увеличению коэффициента неравномерности распределения тока по сечению экрана и активного сопротивления кабеля для частоты 100 кГц при неизменном сечении токопроводящей жилы. Разработанная модель является основой для определения характеристического импеданса силовых высоковольтных одножильных кабелей в широком диапазоне частоты, необходимого для установления адекватных критериев оценки параметров высокочастотных воздействий, критичных для сшитой полиэтиленовой изоляции. Библ. 16, табл. 1, рис. 7.

Ключевые слова: **силовые кабели, комплексное сопротивление, магнитосвязанные контуры, система линейных алгебраических уравнений, токопровод, экран, коэффициент неравномерности распределения тока.**

Introduction. High-voltage power cables with thermosetting polyethylene insulation are critical components of power systems. Many investments are made in their production to ensure reliable operation [1-3]. Power high-voltage cables with insulation based on cross-linked polyethylene with voltage of 6-500 kV are characterized by increased values of electrical capacitance and reduced values of impedance (characteristic impedance) compared to cables with paper-impregnated insulation [4-8]. As a result, there are more and more objects in electrical networks for which complex multi-frequency transients should be expected, which are accompanied by dangerous overvoltages and currents [5-8]. The values of overvoltage and the duration of the transient are determined by the length of the cable line and the impedance of the high-voltage power cable. The duration of transients is tens and hundreds of microseconds, which corresponds to the frequency of such processes from units to tens and hundreds of kilohertz [9]. High-frequency components of current and voltage accelerate, in particular, the development of water treeings in polymer insulation and can cause the development of electrical treeings, i.e. loss of electrical insulation strength of high-voltage power cables [10, 11]. The development of adequate criteria for assessing the parameters of high-frequency effects critical for cross-linked polyethylene insulation of high-voltage cables is based on monitoring of the electrical insulation state during operation, including the results of temporal reflectometry, which requires data on the complex resistance of conductive core and screen to determine the characteristic impedance of the power cable [12].

The normative and technical documentation gives the values of the resistance of the current-carrying core at DC at temperature of 20 °C and the inductance of the power single-core high-voltage cable of coaxial design depending on the spatial location in a three-phase cable line (triangle or plane) [2]. To determine the active resistance of the core during the flow of AC with frequency of 50 Hz, mathematical expressions are given

that approximate the dependence of resistance due to the skin effect and the proximity effect of adjacent single-core cables [2, 13].

In [14] the analytical model of calculation of longitudinal complex resistance taking into account the proximity effect for a current-carrying core and inductance of a core and the metal screen without taking into account influence of frequency of a single-core power cable is presented. In [15], the intrinsic inductance of the metal screen is determined under the assumption of uniform distribution of the induced current in the screen of a single-core power cable.

Thus, obtaining the frequency dependencies of the active resistance and inductance of current-carrying cores and metal shields of high-voltage single-core power cables, taking into account the skin effect and proximity effect is an important and urgent problem, which until recently is insufficiently developed.

The goal of the research is to develop a computational model of complex resistance of high-voltage single-core power cables of coaxial design, necessary to determine the frequency dependencies of active resistance and inductance of conductive core and metal screen taking into account the skin effect and the proximity effect.

Numerical determination of the active resistance and inductance of the current line, taking into account the skin effect and the proximity effect. Divide the conductor into a number of parallel branches (Fig. 1) – current filaments. Each *i*-th branch has an active resistance R_i and an inductance L_i, and due to the magnetic field is connected to the *j*-th branch. The mutual inductance between the *i*-th and the *j*-th branches is denoted as M_{ij}.

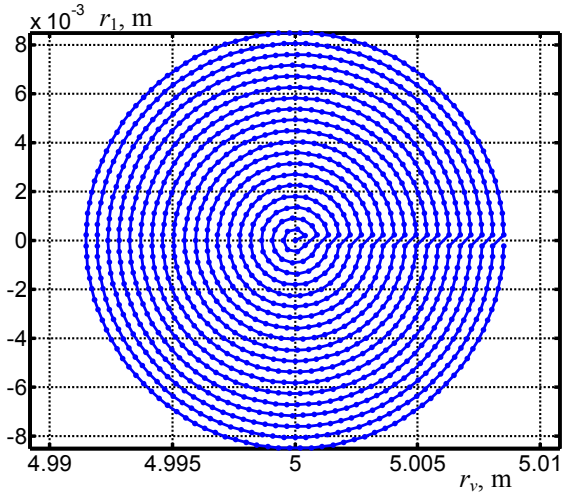

Fig. 1. Layout of nodes along the cross section of the current line. The first node is in the center of the current line, the others are located radially. The line connecting the nodes determines the numbering order – counterclockwise

Suppose that in the *i*-th branch there is a source of variable electromotive force EMF E_i of frequency *f*. Then for the closed contour of this branch we write the Kirchhoff equation:

$$\left(R_i + j\omega L_i\right)\cdot \dot{I}_i + \sum_{j\neq i}^{N_1}\left(j\omega M_{ij}\cdot \dot{I}_j\right) = \dot{E}_i\,, \qquad (1)$$

where the first term $\left(R_i + j\omega L_i\right)\cdot \dot{I}_i$ determines the voltage drop on the active resistance and the intrinsic inductance of the *i*-th branch, and all other components $\sum_{j\neq i}^{N_1}\left(j\omega M_{ij}\cdot \dot{I}_j\right)$ are the voltage drops on the mutual inductance of the *i*-th branch with all other branches.

Equation (1) contains N_1 terms with unknown currents of parallel branches: I_1, I_2, ... I_i, ... I_j, ... I_N. For each of N_1 branches we write an equation similar to (1). We obtain a system of linear algebraic Kirchhoff equations (SLAE):

$$\begin{cases} \left(R_1 + j\omega L_1\right)\cdot \dot{I}_1 + \sum_{j\neq 1}^{N_1}\left(j\omega M_{ij}\cdot \dot{I}_j\right) = \dot{E}_1; \\ \left(R_2 + j\omega L_2\right)\cdot \dot{I}_2 + \sum_{j\neq 2}^{N_1}\left(j\omega M_{ij}\cdot \dot{I}_j\right) = \dot{E}_2; \\ \cdots \\ \left(R_{N1} + j\omega L_{N1}\right)\cdot \dot{I}_{N1} + \sum_{j\neq N1}^{N_1}\left(j\omega M_{ij}\cdot \dot{I}_j\right) = \dot{E}_{N1}. \end{cases} \qquad (2)$$

Write SLAE (2) in matrix form:

$$\begin{pmatrix} \left(R_1 + j\omega L_1\right) & j\omega M_{12} & \cdots & j\omega M_{1,N} \\ j\omega M_{21} & \left(R_2 + j\omega L_2\right) & \cdots & j\omega M_{2,N} \\ \cdots & & & \cdots \\ j\omega M_{N,1} & j\omega M_{N,2} & \cdots & \left(R_N + j\omega L_N\right) \end{pmatrix} \cdot \begin{pmatrix} \dot{I}_1 \\ \dot{I}_2 \\ \cdots \\ \dot{I}_N \end{pmatrix} = \begin{pmatrix} \dot{E}_1 \\ \dot{E}_2 \\ \cdots \\ \dot{E}_N \end{pmatrix}. \qquad (3)$$

On the diagonal of the matrix of SLAE coefficients (3) there are the intrinsic resistances of the branches (active and inductive), outside the diagonal – the mutual inductive resistances of the branches.

In some cases, the values of EMF acting in the branches of the current line are the same – $\dot{E}_S$. Then SLAE (3) takes the form:

$$\begin{pmatrix} \left(R_1 + j\omega L_1\right) & j\omega M_{12} & \cdots & j\omega M_{1,N} \\ j\omega M_{21} & \left(R_2 + j\omega L_2\right) & \cdots & j\omega M_{2,N} \\ \cdots & & & \cdots \\ j\omega M_{N,1} & j\omega M_{N,2} & \cdots & \left(R_N + j\omega L_N\right) \end{pmatrix} \cdot \begin{pmatrix} \dot{I}_1 \\ \dot{I}_2 \\ \cdots \\ \dot{I}_N \end{pmatrix} = \begin{pmatrix} \dot{E}_S \\ \dot{E}_S \\ \cdots \\ \dot{E}_S \end{pmatrix}. \qquad (4)$$

SLAE (4) allows to determine the parameters of the complex resistance of current lines, taking into account the skin effect and the proximity effect.

The mutual inductance M_{12} between two coaxial ring contours with currents is calculated based on the analytical formula [16]:

$$M_{12} = 2\mu\mu_0\sqrt{r_1\cdot r_2}\cdot\frac{1}{k}\cdot\left[\left(1-\frac{k^2}{2}\right)K(k) - E(k)\right], \qquad (5)$$

where r_1, r_2 are the radii of the current lines (for single-phase power cable of coaxial design r_1 is the radius of the current-carrying core; r_2 is the inner radius of the metal cable screen, respectively); $k = \sqrt{\frac{4r_1r_2}{(r_1+r_2)^2+G^2}}$; where *G*

is the distance between the planes of the current lines along the axis of symmetry; $K(k)$ and $E(k)$ are functions of complete elliptic integrals of the first and second kind:

$$K(k)=\int_0^{\pi/2}\frac{d\beta}{\sqrt{1-k^2\sin^2\beta}};\ E(k)=\int_0^{\pi/2}\sqrt{1-k^2\sin^2\beta}\cdot d\beta.$$

The intrinsic inductance of a circular conductor of massive cross-section is calculated as the mutual inductance between two filamentary conductors of the same radius, located at a distance G from each other.

For a circular section of radius r, the geometric mean distance of the area of the circle from itself G is equal to:

$$G=\frac{r}{\sqrt[4]{e}}, \qquad (6)$$

where e = 2.71828... is the basis of natural logarithms.

As a result of solution (4), the currents in the branches I and the total current I_Σ of all parallel branches of the current line are determined.

After finding the total current of all parallel branches, the total complex resistance, its active R and reactive X_L components, the equivalent inductance L of the current line are determined:

$$\dot{Z}=\frac{\dot{E}_s}{\dot{I}_\Sigma\cdot 2\pi r_v},\quad R=\mathrm{Re}(\dot{Z}),\quad X_L=\mathrm{Im}(\dot{Z}),\quad L=\frac{X_L}{\omega}, \qquad (7)$$

where r_v is the bending radius of the current line.

Results of numerical modelling. The axis of symmetry of the annular current line (Fig. 1) is on the left at a distance Z from the center of the current line. Passing the nodes in each layer begins on the outside of the annular current line, then passes on the inside and returns to the outside. The current tends to pass along the path of the smallest length (on the inner side of the current line), due to which its density is higher there (Fig. 1).

Figures 2–4 show the effect of frequency on the distribution of currents I in branches N (Fig. 2), active resistance R_c (Fig. 3), equivalent inductance L_c (Fig. 4) of a copper conductive core of a power cable with a cross section of 240 mm^2 (Fig. 2,*a*; curves 1 in Fig. 3, 4) and 800 mm^2 (Fig. 2,*b*; curves 2 in Fig. 3, 4), respectively.

With increasing frequency, the displacement of current on the surface of the current line increases. As a result, the effective resistance of the current line increases (Fig. 3).

Figure 5 shows a layout of the location of the nodes at the intersection of the conductive core and the screen of the power single-core cable of coaxial structure. The results of numerical calculation of frequency-dependent active resistance and inductance L of the power cable with voltage of 110 kV with a cross section of a copper conductive core of 240 mm^2 and a copper screen with thickness of 1 mm are shown in Fig. 6, 7, respectively. The active resistance of the cable R consists of the resistance of the conductive core R_c and the metal screen R_s: $R = R_c + R_s$. The equivalent inductance of the cable L includes the equivalent inductance of the conductive core L_c, the equivalent screen inductance L_s and the mutual inductance between core and screen.

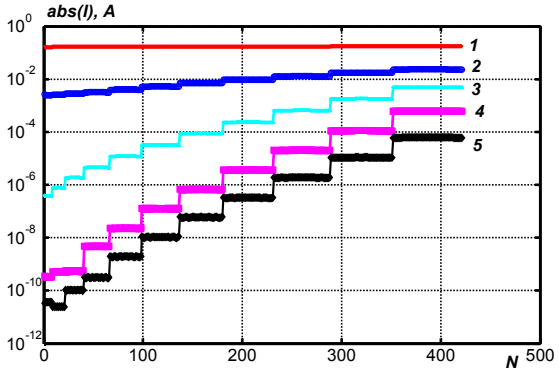

a

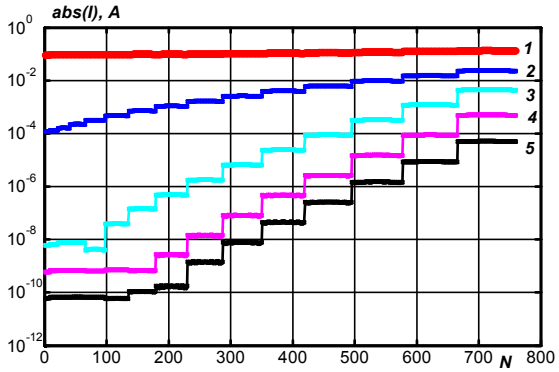

b

Fig. 2. Influence of frequency on current distribution on branches N of the power current line (curve 1 – frequency 50 Hz, curve 2 – 1 kHz, curve 3 – 10 kHz, curve 4 – 100 kHz, curve 5 – 1 MHz)

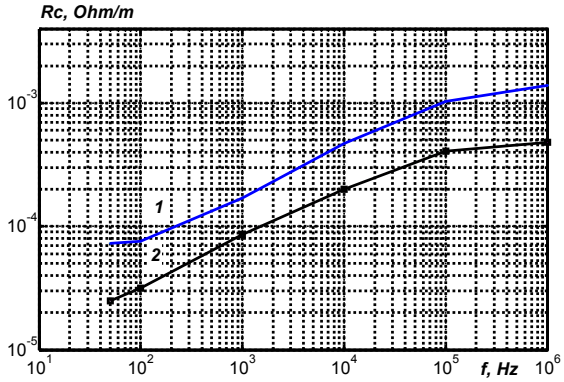

Fig. 3. Frequency dependencies of active resistance of copper power current line

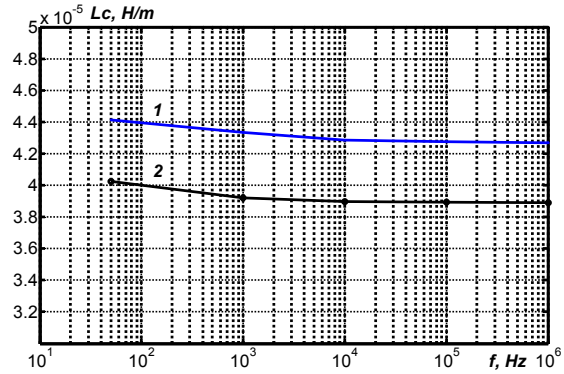

Fig. 4. Frequency dependencies of equivalent inductance of copper power current line

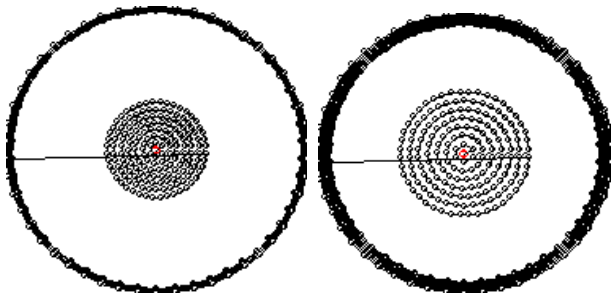

a *b*

Fig. 5. Layout of the nodes at the intersection of the conductive core and the screen with thickness of 1 mm (*a*) and 3 mm (*b*)

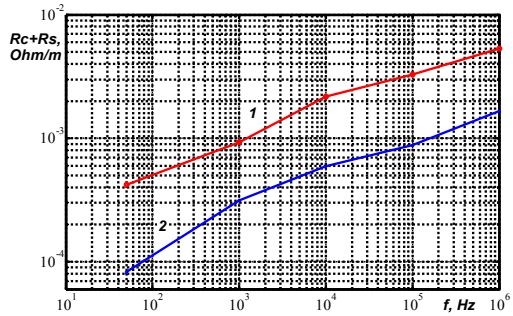

Fig. 6. Frequency dependence of the active resistance of a power cable of single-core design of voltage of 110 kV

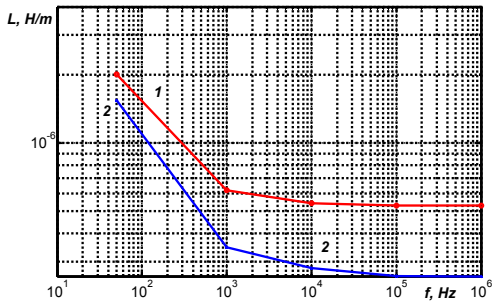

Fig. 7. Frequency dependence of the equivalent inductance of a power cable of single-core design of voltage of 110 kV

Increase the thickness of the copper screen 3 times (from 1 to 3 mm) leads to an increase in the coefficient of non-uniformity of current distribution across the screen by 1.25 and 4.48 times with constant value of the coefficient of non-uniformity of current distribution across the copper core section for frequency of 1 kHz and 100 kHz, respectively. For frequency of 1 kHz, the active resistance of a cable with a screen of smaller thickness is 1.4 times the active resistance of a cable with a screen of thicker thickness.

Checking the reliability of the results of numerical calculations is performed on the basis of comparing the coefficients of non-uniformity of the current distribution due to the skin effect and the proximity effect, along the cross section of the current line.

The first coefficient K_f is calculated through the ratio of heat output at AC and DC. The power of heat dissipation at AC is determined by the total power of heat dissipation of parallel branches taking into account the redistribution of current along the cross section of the conductive core. The power of heat dissipation at DC is determined by the uniform distribution of current across the cross section of the conductive core.

The second coefficient K_R is calculated through the ratio of the resistance of the current line at AC and DC.

Table 1 shows a comparative analysis of the coefficients of non-uniformity of current distribution at the intersection of conductive copper cores. The results of the calculations are identical.

Table 1

Comparative analysis of the coefficients of non-uniformity of current distribution across the current line section

Frequency, Hz	Cross section of the copper current line 240 mm^2		Cross section of the copper current line 800 mm^2	
	K_f	K_R	K_f	K_R
50	1,0156	1,0156	1,1546	1,1545
100	1,0605	1,0605	1,4598	1,4598
1000	2,3581	2,3581	3,9658	3,9655
10000	6,5865	6,5865	9,2692	9,2686
100000	14,3079	14,3079	19,4337	19,4337
1000000	19,4332	19,4332	22,2853	22,2836

Conclusions.

For the first time, a computational numerical model for determining the complex resistance of high-voltage single-core power cables with polymer insulation is proposed, which allows to determine the active resistance and inductance of both conductive core and copper screen, taking into account the skin effect and proximity effect.

The developed model is the basis for determining the characteristic impedance of high-voltage single-core power cables in a wide range of frequencies required to establish adequate criteria for evaluating the parameters of high-frequency effects critical for cross-linked polyethylene insulation.

Based on the proposed computational numerical model, an appropriate technique can be developed to determine the frequency dependencies of the active resistance and inductance of a single-core power cable of coaxial design, which can be the basis for improving the accuracy of mathematical modelling of transients in cable lines arising at single-phase short circuits to the earth and other switchings in electric networks at bilateral grounding of the screen.

Conflict of interest. The authors declare that they have no conflicts of interest.

REFERENCES

1. Shidlovsky A.K., Shcherba A.A., Zolotarev V.M., Podoltsev A.D., Kucheryavaya I.N. *Kabeli s polimernoi izoliatsiei na sverkhvysokie napriazheniia* [EHV cables with polymer insulation]. Kyiv, Institute of Electrodynamics of the NAS of Ukraine Publ., 2013. 552 p. (Rus).

2. XLPE-insulated power cables for voltages from 45 kV up to 330 kV. PJSC Yuzhcable Works, Kharkiv. Available at: https://yuzhcable.com.ua/wp-content/uploads/2018/03/Catalogue-XLPE-cables-45-330-kV.pdf (accessed 13 May 2020).

3. Bezprozvannych G.V. Zolotaryov V.M., Antonets Y.A. High voltage cable systems with integrated optical fiber for monitoring cable lines. *2020 IEEE KhPI Week on Advanced Technology (KhPIWeek)*, 2020, pp. 407-410. doi: https://doi.org/10.1109/KhPIWeek51551.2020.9250174.

4. Wang H., Cao J., He Z., Yang J., Han Z., Chen G. Research on Overvoltage for XLPE Cable in a Modular Multilevel Converter HVDC Transmission System. *IEEE Transactions on Power Delivery*, 2016, vol. 31, no. 2, pp. 683-692. doi: https://doi.org/10.1109/TPWRD.2015.2469595.
5. Li J., Xu L., Chen X., Zhao A., Liu J., Zhao X., Deng J., Zhang G. Analysis of statistical and frequency characteristics of transient overvoltage of hybrid cable-OHL lines. *2018 China International Conference on Electricity Distribution (CICED)*, 2018, pp. 2650-2654. doi: https://doi.org/10.1109/CICED.2018.8592463.
6. Olsen R.G. Propagation along overhead transmission lines with multiply grounded shield wires. *IEEE Transactions on Power Delivery*, 2017, vol. 32, no. 2, pp. 789-798. doi: https://doi.org/10.1109/TPWRD.2016.2561977.
7. Zhao H., Zhang W., Wang Y. Characteristic Impedance Analysis of Medium-Voltage Underground Cables with Grounded Shields and Armors for Power Line Communication. *Electronics*, 2019, vol. 8, no. 5, p. 571. doi: https://doi.org/10.3390/electronics8050571.
8. Meng J., Wang W., Tang X., Xu X. Zero-sequence voltage trajectory analysis for unbalanced distribution networks on single-line-to-ground fault condition. *Electric Power Systems Research*, 2018, vol. 161, pp. 17-25. doi: https://doi.org/10.1016/j.epsr.2018.03.024.
9. Varetsky Y. Overvoltages in MV industrial grid under ground faults. *Energy Engineering and Control Systems*, 2019, vol. 5, no. 2, pp. 75-80. doi: https://doi.org/10.23939/jeecs2019.02.075.
10. Bezprozvannych A.V., Kessaev A.G., Shcherba M.A. Frequency dependence of dielectric loss tangent on the degree of humidification of polyethylene cable insulation. *Technical Electrodynamics*, 2016, no. 3, pp. 18-24. (Rus). doi: https://doi.org/10.15407/techned2016.03.018.
11. Zhu G., Zhou K., Gong W., He M., Kong J., Li K. Inhibition of rejuvenation liquid on trees in XLPE cables under switching impulse voltages. *Energies*, 2019, vol. 12, no. 11, p. 2133. doi: https://doi.org/10.3390/en12112133.
12. Papazyan R. Concepts for market-based MV cable operations and maintenance using insulation parameters measurements. *2020 12th Electrical Engineering Faculty Conference (BulEF)*, 2020, pp. 1-5, doi: https://doi.org/10.1109/BulEF51036.2020.9326055.
13. *IEC 60287-1-1. 2006. Electric cables – Calculation of the current rating - Part 1-1: Current rating equations (100 % load factor) and calculation of losses – General*. – 65 p.
14. Aloui T., Amar F.B., Abdallah H.H. Fault prelocalization of underground single-phase cables: Modeling and simulation. *International Journal of Electrical Power & Energy Systems*, 2019, vol. 44, no. 1, pp. 514-519. doi: https://doi.org/10.1016/j.ijepes.2012.07.067.
15. Rozov V.Y., Tkachenko O.O., Yerisov A.V., Grinchenko V.S. Analytical calculation of magnetic field of three-phase cable lines with two-point bonded shields. *Technical Electrodynamics*, 2017, no. 2, pp. 13-18. (Rus). doi: http://doi.org/10.15407/techned2017.02.013.
16. Kalantarov P.L., Tseytlin L.A. *Raschet induktivnostei* [Inductance calculations]. Leningrad, Energoatomizdat Publ., 1986. 487 p. (Rus).

Received 14.04.2021
Accepted 22.05.2021
Published 25.06.2021

G.V. Bezprozvannych[1], *Doctor of Technical Science, Professor,*
I.A. Kostiukov[1], *PhD, Doctoral Student,*
[1] National Technical University «Kharkiv Polytechnic Institute», 2, Kyrpychova Str., Kharkiv, 61002, Ukraine,
e-mail: bezprozvannych@kpi.kharkov.ua (Corresponding author),
iakostiukow@gmail.com

How to cite this article:
Bezprozvannych G.V., Kostiukov I.A. A calculation model for determination of impedance of power high voltage single-core cables with polymer insulation. *Electrical Engineering & Electromechanics*, 2021, no. 3, pp. 47-51. doi: https://doi.org/10.20998/2074-272X.2021.3.08.

UDC 621.3 https://doi.org/10.20998/2074-272X.2021.3.09

N. Belbachir, M. Zellagui, S. Settoul, C. Z. El-Bayeh, B. Bekkouche

SIMULTANEOUS OPTIMAL INTEGRATION OF PHOTOVOLTAIC DISTRIBUTED GENERATION AND BATTERY ENERGY STORAGE SYSTEM IN ACTIVE DISTRIBUTION NETWORK USING CHAOTIC GREY WOLF OPTIMIZATION

Goal. *The integration of photovoltaic distributed generations in the active distribution network has raised quickly due to their importance in delivering clean energy, hence, participating in solving various problems as climate change and pollution. Adding the battery energy storage systems would be considered as one of the best choices in giving solutions to the mentioned issues due to its characteristics of quick charging and discharging, managing the quality of power, and fulfilling the peak of energy demand.* ***The novelty*** *of the proposed work is the development of new multi-objective functions based on the sum of the three technical parameters of total active power loss, total voltage deviation, and total operation time of the overcurrent protection relay.* ***Purpose.*** *This paper is dedicated for solving the allocation problem of hybrid photovoltaic distributed generation and battery energy storage systems integration in the standard IEEE 33-bus and IEEE 69-bus active distribution networks.* ***Methodology.*** *The optimal integration of the hybrid systems is formulated as minimizing the proposed multi-objective functions by applying a newly developed metaheuristic technique based on various chaotic grey wolf optimization algorithms. The applied optimization algorithms are becoming increasingly popular due to their simplicity, lack of gradient information needed, ability to bypass local optima, and versatility in power system applications.* ***Results****. The simulation results of both test systems confirm the robustness and efficiency of the chaotic logistic grey wolf optimization algorithm compared to the rest of the algorithms in terms of convergence to the global optimal solution and in terms of providing the best and minimum multi-objective functions-based power losses, voltage deviation and relay operation time values.* ***Practical significance****. Recommendations have been developed for the use of optimal allocation of hybrid systems for practical industrial distribution power systems with the renewable energy sources presence.* References 32, tables 4, figures 9.

Key words: **photovoltaic distributed generation, battery energy storage system, active distribution network, optimal integration, multi-objective functions, chaotic grey wolf optimization algorithm.**

Мета. *Інтеграція фотоелектричної розподіленої генерації в активну розподільчу мережу швидко зросла завдяки її важливості для доставки чистої енергії, отже, участі у вирішенні різних проблем, таких як зміна клімату та забруднення. Додавання акумуляторних систем накопичення енергії може бути розглянуто як один з найкращих варіантів вирішення зазначених питань завдяки своїм характеристикам швидкої зарядки та розрядки, управління якістю енергії та задоволення піку енергетичних потреб.* ***Новизна*** *запропонованої роботи полягає у розробці нових багатоцільових функцій на основі суми трьох технічних параметрів сумарних втрат активної потужності, загальних відхилень напруги та загального часу спрацьовування реле захисту від перевантаження по струму.* ***Мета.*** *Стаття присвячена вирішенню проблеми розподілу гібридних фотоелектричних розподілених систем генерації та інтеграції систем накопичення енергії в стандартні активні розподільчі мережі з 33-шинами IEEE та 69-шинами IEEE.* ***Методологія.*** *Оптимальна інтеграція гібридних систем сформульована як мінімізація запропонованих багатоцільових функцій шляхом застосування нещодавно розробленої метаевристичної методики, заснованої на різних хаотичних алгоритмах оптимізації сірого вовка. Застосовані алгоритми оптимізації стають дедалі популярнішими завдяки своїй простоті, відсутності необхідної інформації щодо градієнту, можливості обходу локальних оптимумів та універсальності в застосуваннях щодо енергосистеми.* ***Результати.*** *Результати моделювання обох тестових систем підтверджують надійність та ефективність хаотичного логістичного алгоритму оптимізації сірого вовка в порівнянні з іншими алгоритмами з точки зору збіжності до глобального оптимального розв'язання та з точки зору забезпечення найкращих і мінімальних багатоцільових функцій на основі втрат потужності, відхилення напруги та значень часу спрацювання реле.* ***Практичне значення.*** *Розроблено рекомендації щодо використання оптимального розподілу гібридних систем для реальних промислових розподільчих енергосистем із наявністю відновлюваних джерел енергії.* Бібл. 32, табл. 4, рис. 9.

Ключові слова: **фотоелектрична розподілена генерація, акумуляторна система накопичення енергії, активна розподільна мережа, оптимальна інтеграція, багатоцільові функції, хаотичний алгоритм оптимізації сірого вовка.**

1. Introduction. In the last years, the penetration of Renewable Energy Sources (RES) in the Active Distribution Network (ADN) has rapidly increased to address the problems of climate change and pollution. Photovoltaic Distributed Generation (PVDG) often uses ADN to access many RESs for their benefits in pollution reduction, voltage profile enhancement, and power loss reduction. However, large-scale PVDG sources in the ADN variations, on the other hand, may cause voltage fluctuations in power supply systems, resulting in a loss of the quality of power and some other issues that have sparked widespread concern. Additionally, increasing PV penetration in the future could pose a serious threat to the utility ADN reliability and stability.

The Battery Energy Storage Systems (BESS) has emerged as one of most successful solutions for dealing with these issues [1]. The BESS has become a popular method of smoothing active power variations of distribution grid connected PVDG sources at the common coupling point in recent years. The BESS enables quick charging and discharging, enhancing the versatility of ADN, especially those with multiple PVDG sources. In practice, the BESS provides ADN with a variety of services in several countries [2].

Recently, various researchers have been dedicated to develop an advanced solution that identifies the best locations and sizes for PVDGs and BESSs units to improve ADN operation and planning problems, as applying the Mixed Integer Linear Programming (MILP) to reduce the total cost of energy in ADN [3, 4], and MILP algorithm while considering the environmental and

economic aspects [5]. Stochastic Mixed Integer Linear Programming (SMILP) for overall network cost minimization with ADN reconfiguration [6], and the Mixed-Integer Second-Order Cone Program (MISOCP) to minimize real-time energy gap with uncertainties [7], and also using MISOCP to reduce the total cost's operation and BESS cost's investment considering soft open points of ADN [8]. Dynamic programming optimization algorithm to maximize the renewable DG consumption and BESS benefits [9]. Applying Genetic Algorithm (GA) for active power losses minimization [10], and applying GA for minimizing the BESS total cost, also the yearly cost of voltage-sag events [11], also GA for reducing the total net present value from BESS deployment over a specified planning horizon [12], and applied multi-player distributed optimization game algorithm to maximize the cost and benefits of BESS [13].

Applied Differential Evolutionary (DE) algorithm for minimizing the investment and maintenance costs considering time-varying load model [14]. Implantation of the Group Search Optimizer (GSO) algorithm to minimize the system stability index of ADN [15], Modified Bat Algorithm (MBA) for minimizing the system's total cost with various irradiances at different days [16], Hybrid Gravity Search Algorithm (HGSA) for reducing the BESS daily cost of maintenance and operation also its initial investment [17], used Teaching–Learning-Based Optimization (TLBO) algorithm for minimization of life cycle cost and gas emissions [18], Whale Optimization Algorithm (WOA) for reducing the ADN's power losses [19], Particle Swarm Optimization (PSO) algorithm for reducing the active power loss and the node voltages deviation indices with the dynamic hourly reconfiguration of ADN [20], Natural Aggregation Algorithm (NAA) for minimizing the investment and operation cost of the system, and the BESS's residual value [21], Harris Hawks Optimization (HHO) algorithm to minimize the sum of the bus voltage deviation and active power losses [22]. Recently in 2021, applied Simulated Annealing (SA) algorithm for utility profit maximization from energy arbitrage [23].

This paper has applied a new recent meta-heuristic which called the Grey Wolf Optimizer (GWO); an optimization algorithm inspired based on the hunting behavior of grey wolves that lives in wild nature [24]. The principal defies of GWO that it is easy to fall into the local optimum. Owing to the ergodicity of chaos, in this paper is included the theory of chaos into the GWO algorithm to strengthen its performance [25].

Practically, the operational objectives are conflicting in nature. Hence, the problem of allocating PVDG and BESS becomes a complex multi-objective function problem that optimizes multiple conflicting objectives. In this paper, an allocation problem of hybrid PVDG–BESS systems is formulated to minimize the Multi-Objective Functions (MOF) which can be solved by the various versions of Chaotic Grey Wolf Optimization (CGWO) algorithms.

2. Mathematical problem formulation.

2.1. Multi-objective functions. In this paper, aim to optimally locate and size the hybrid PVDG and BESS sources into ADN, by minimizing simultaneously the technical parameters of Total Active Power Loss (TAPL), Total Voltage Deviation (TVD), and Total Operation Time (TOT) of Non-Standard Overcurrent Relay (NS-OCR), which is based on new time-current-voltage tripping characteristic

$$MOF = Minimize \sum_{i=1}^{N_{bus}} \sum_{j=2}^{N_{bus}} \sum_{i=1}^{N_R} \left[TAPL_{i,j} + TVD_j + TOT_i \right]. \quad (1)$$

Starting by, the TAPL of the distribution line, that can be expressed by [26, 27]

$$TAPL_{i,j} = \sum_{i=1}^{N_{bus}} \sum_{j=2}^{N_{bus}} APL_{i,j}, \quad (2)$$

$$APL_{i,j} = \alpha_{ij} \left(P_i P_j + Q_i Q_j \right) + \beta_{ij} \left(Q_i P_j + P_i Q_j \right), \quad (3)$$

$$\alpha_{ij} = \frac{R_{ij}}{V_i V_j} \cos\left(\delta_i - \delta_j \right), \quad (4)$$

$$\beta_{ij} = \frac{R_{ij}}{V_i V_j} \sin\left(\delta_i + \delta_j \right), \quad (5)$$

where R_{ij} is the line resistance; N_{bus} is the bus number; (δ_i, δ_j) and (V_i, V_j) are angles and voltages, respectively; (P_i, P_j) and (Q_i, Q_j) demonstrate active and reactive powers, respectively.

The second term is the TVD, which is defined as [28, 29]

$$TVD_j = \sum_{j=2}^{N_{bus}} \left| 1 - V_j \right|. \quad (6)$$

The final term, the TOT of NS-OCR, which is defined as [30]

$$TOT_i = \sum_{i=1}^{N_R} T_i, \quad (7)$$

$$T_i = \left(\frac{1}{e^{(1-V_{FM})}} \right)^K TDS_i \left(\frac{A}{M_i^B - 1} \right), \quad (8)$$

$$M_i = \frac{I_F}{I_P}, \quad (9)$$

where T_i is the operation time of relay; TDS is the time dial setting; M is the multiple of pickup current and V_{FM} represent the fault voltage magnitude; I_F and I_P represent the fault and the pickup current, respectively; A, B, and K are the constants of relay, set to 0.14, 0.02, and 1.5, respectively; N_R is the number of overcurrent relays.

2.2. Equality constraints can be expressed by the balanced powers equations

$$P_G + P_{PVDG} + P_{BESS} = P_D + APL, \quad (10)$$

$$Q_G = Q_D + RPL, \quad (11)$$

where (Q_G, P_G) represent the total reactive and active power from the generator; (Q_D, P_D) represent the total reactive and active power of the load; (RPL, APL) are the reactive and active power loss, respectively; P_{PVDG} and P_{BESS} are the output powers generated from PVDG and BESS, respectively.

2.3. Distribution line constraints would be given as inequality constraints

$$V_{\min} \le \left| V_i \right| \le V_{\max}, \quad (12)$$

$$\left| 1 - V_j \right| \le \Delta V_{\max}, \quad (13)$$

$$\left| S_{ij} \right| \le S_{\max}, \quad (14)$$

where $V_{\min}$, $V_{\max}$ are minimum and maximum of bus voltage limits; $\Delta V_{\max}$ is the maximum of voltage drop limits; S_{ij} is the apparent power in the distribution line and $S_{\max}$ is the maximum of apparent power.

2.4. PVDG-BESS units constraints can be expressed as follow

$$P_{PVDG}^{\min} \le P_{PVDG} \le P_{PVDG}^{\max}, \quad (15)$$

$$P_{BESS}^{\min} \le P_{BESS} \le P_{BESS}^{\max}, \quad (16)$$

$$\sum_{i=1}^{N_{PVDG}} P_{PVDG}(i) \le \sum_{i=1}^{N_{bus}} P_D(i), \quad (17)$$

$$\sum_{i=1}^{N_{BESS}} P_{BESS}(i) \le \sum_{i=1}^{N_{bus}} P_D(i), \quad (18)$$

$$2 \le PVDG_{Position} \le N_{bus}, \quad (19)$$

$$2 \le BESS_{Position} \le N_{bus}, \quad (20)$$

$$N_{PVDG} \le N_{PVDG.\max}, \quad (21)$$

$$N_{BESS} \le N_{BESS.\max}, \quad (22)$$

$$n_{PVDG,i} / Location \le 1, \quad (23)$$

$$n_{BESS,i} / Location \le 1, \quad (24)$$

where $P_{PVDG}^{\min}$, $P_{BESS}^{\min}$ are the minimum of output power injected by PVDG and BESS, respectively; $P_{PVDG}^{\max}$, $P_{BESS}^{\max}$ are the maximum of output power injected by PVDG, and BESS, respectively; N_{PVDG}, N_{BESS} are the PVDG and BESS units' number, respectively; n_{BESS}, n_{PVDG} are the locations of PVDG and BESS units at bus i.

3. Chaotic grey wolf optimization. As long as the GWO algorithm could not always perform that well in identifying global optimal results, CGWO algorithm was developed basing on introducing chaos (chaotic maps) in GWO algorithm itself in order to improve its efficiency by generating random numbers.

3.1. Grey wolf optimizer. The GWO is an algorithm evolved by Mirjalili [24], basing on the inspiration from the leadership hierarchy behaviours and the grey wolves hunt mechanism in wild nature, where it begins the process of optimization by initiating a plant of candidate solutions randomly.

The three best candidate solutions in each iteration, are assumed as alpha, beta, and delta wolves, who take the lead toward to promising search space regions. The rest of grey wolves are considered as omega and need to encircle alpha, beta, and delta to find better solutions. The mathematical formulation of omega wolves is expressed as [24, 31].

Encircling prey: grey wolves encircle prey during the hunt. The mathematical model expressed as follows:

$$\vec{D} = \left| \vec{C}.\vec{X}_p(t) - \vec{X}(t) \right|, \quad (25)$$

$$\vec{X}(t+1) = \vec{X}_p(t) - \vec{A}.\vec{D}, \quad (26)$$

where $\vec{A}$ and $\vec{C}$ designate the coefficient vectors; t designates the current iteration; $\vec{X}_p$ is the best solution's position vector obtained so far; $\vec{X}$ is the vector of position.

The vectors $\vec{A}$ and $\vec{C}$ can be calculated using these equations

$$\vec{A} = 2.\vec{a}.\vec{r} - \vec{a}, \quad (27)$$

$$\vec{C} = 2.\vec{r}, \quad (28)$$

where a is the decreased linearly from 2 to 0 over the iterations course (in exploration and exploitation phases); $\vec{r}$ is the vector randomly initiated with uniform distribution between 0 and 1.

Hunting: in GWO, it is supposed that alpha (α), beta (β), and gamma (δ) have better knowledge about the prey's potential location, the three best solutions obtained firstly so far are saved and obligate the other search agents (including the omegas) to update their positions according to the best search agent's position

$$\vec{D}_\alpha = \left| \vec{C}_1.\vec{X}_\alpha - \vec{X} \right|, \quad (29)$$

$$\vec{D}_\beta = \left| \vec{C}_2.\vec{X}_\beta - \vec{X} \right|, \quad (30)$$

$$\vec{D}_\delta = \left| \vec{C}_3.\vec{X}_\delta - \vec{X} \right|, \quad (31)$$

$$\vec{X}_1 = \vec{X}_\alpha - \vec{A}_1.(\vec{D}_\alpha), \quad (32)$$

$$\vec{X}_2 = \vec{X}_\beta - \vec{A}_2.(\vec{D}_\beta), \quad (33)$$

$$\vec{X}_3 = \vec{X}_\delta - \vec{A}_3.(\vec{D}_\delta), \quad (34)$$

$$\vec{X}(t+1) = \frac{\vec{X}_1 + \vec{X}_2 + \vec{X}_3}{3}. \quad (35)$$

3.2. Chaotic maps. The various chaotic maps [32] used are represented by their mathematical equations:

a. Chaotic Gauss:

$$x_{k+1} = \begin{cases} 1 & x_k = 0 \\ \dfrac{1}{\mathrm{mod}(x_k, 1)} & otherwise \end{cases}. \quad (36)$$

b. Chaotic Singer:

$$x_{k+1} = 1.07\left(7.86x_k - 23.31x_k^2 + 28.75x_k^3 - 13.302875x_k^4\right). \quad (37)$$

c. Chaotic Tent:

$$x_{k+1} = \begin{cases} \dfrac{x_k}{0.7}, & x_k < 0.7 \\ \dfrac{10}{3}(1 - x_k), & x_k \ge 0.7 \end{cases}. \quad (38)$$

d. Chaotic Sine:

$$x_{k+1} = \frac{a}{4}\sin(\pi x_k), \quad a = 4. \quad (39)$$

e. Chaotic Logistic:

$$x_{k+1} = a x_k (1 - x_k), \quad a = 4. \quad (40)$$

4. Simulation and analysis results. The various algorithms were tested on the standards test system IEEE 33-bus and 69-bus ADNs represented in Fig. 1, which comprised active and reactive powers of 3715 kW and 2300 kVar for the first system, 3790 kW and 2690 kVar for the second system. Also, under a nominal voltage equal to 12.66 kV for both systems. Where every one of systems' buses, would be protected by a NS-OCR. In general, it is calculated 32 NS-OCRs for the first system and 68 NS-OCRs for the second system.

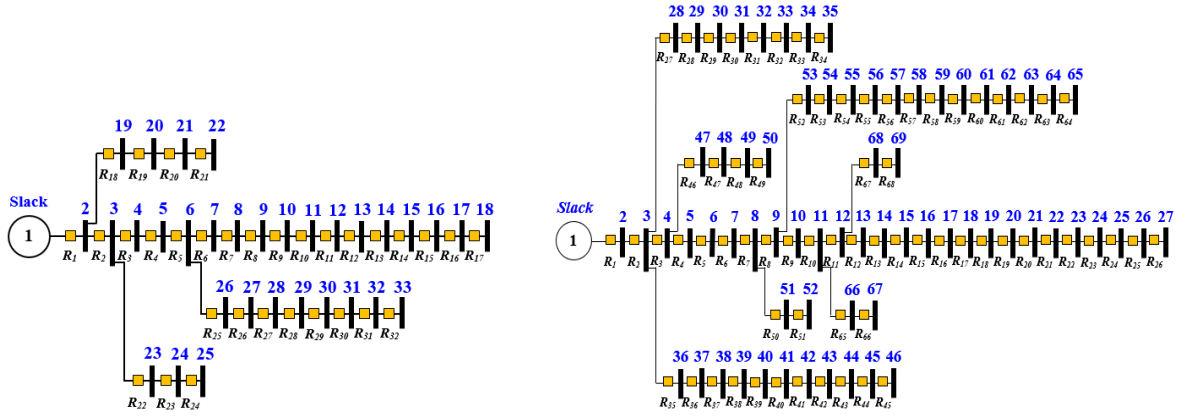

a *b*

Fig. 1. Single diagram of test systems: *a* – IEEE 33-bus; *b* – IEEE 69-bus

Figures 2, 3 demonstrate the curves of convergence of the applied CGWO algorithms for both cases of optimal PVDG and hybrid PVDG-BESS installation in both test systems ADNs.

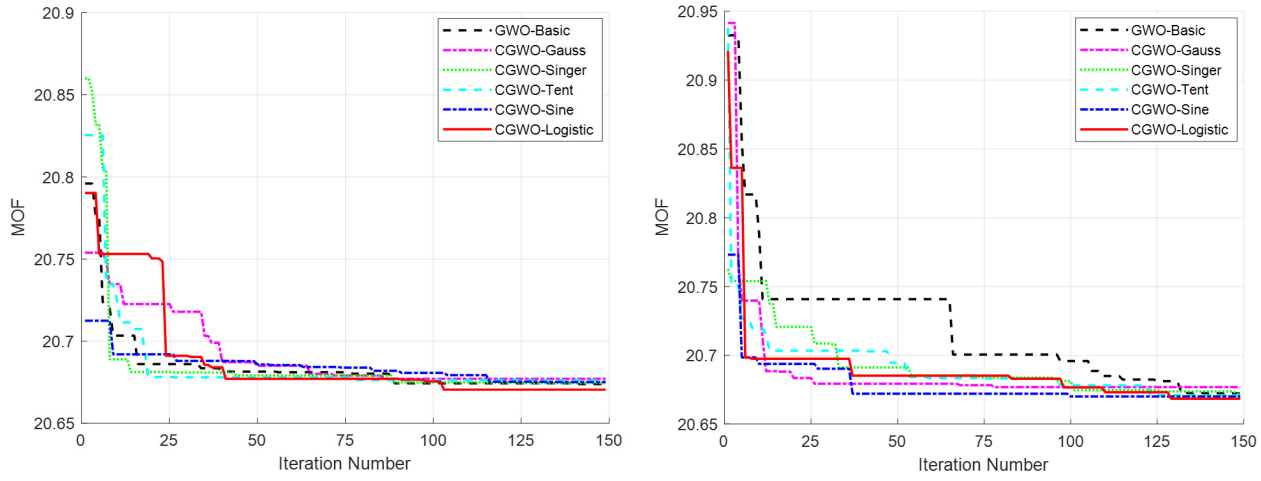

a *b*

Fig. 2. Convergence curves of different CGWO algorithms for the IEEE 33-bus: *a* – PVDG; *b* – PVDG-BESS

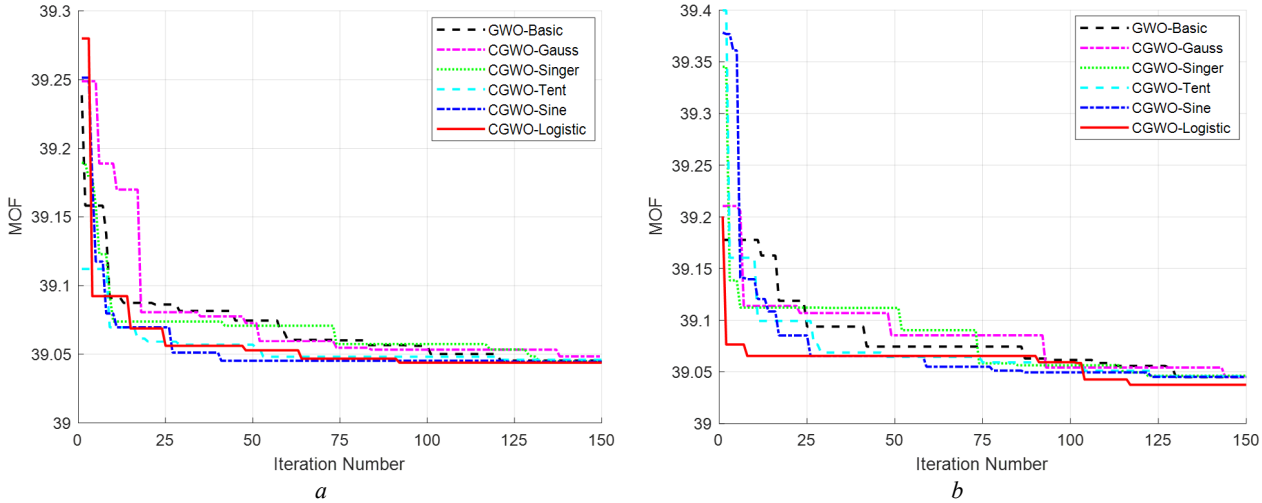

a *b*

Fig. 3. Convergence curves of different CGWO algorithms for the IEEE 69-bus: *a* – PVDG; *b* – PVDG-BESS

By doing the analysis of both convergence curves, also for a maximum iterations' number equal to 150, it can be noted that the CGWO_Logistic delivered the best minimization of MOF results for both cases of PVDG and hybrid PVDG-BESS presence in both test system ADNs, comparing to the other algorithms.

For the case of only PVDG integration, the MOF got minimized by the CGWO_Logistic algorithm until 20.670 for the first test system ADN, and until 39.043 for the second system ADN.

For the case of hybrid PVDG-BESS, the MOF got minimized by the CGWO_Logistic algorithm until 20.668 for the first system, while for the second system it got minimized until 39.037, with noticing a late convergence characteristic in both cases studies for the two test systems which were in general, more than 100 iterations for all cases studies, except for the case of PVDG integration in second test system, where the CGWO_Logistic algorithm converges around 85 iterations to attain the best solution.

Figures 4, 5 illustrate the MOF boxplot results of the different applied CGWO algorithms after 20 runs in each of them, for both cases studies of optimal PVDG and hybrid PVDG-BESS integration, respectively in the two test systems ADNs.

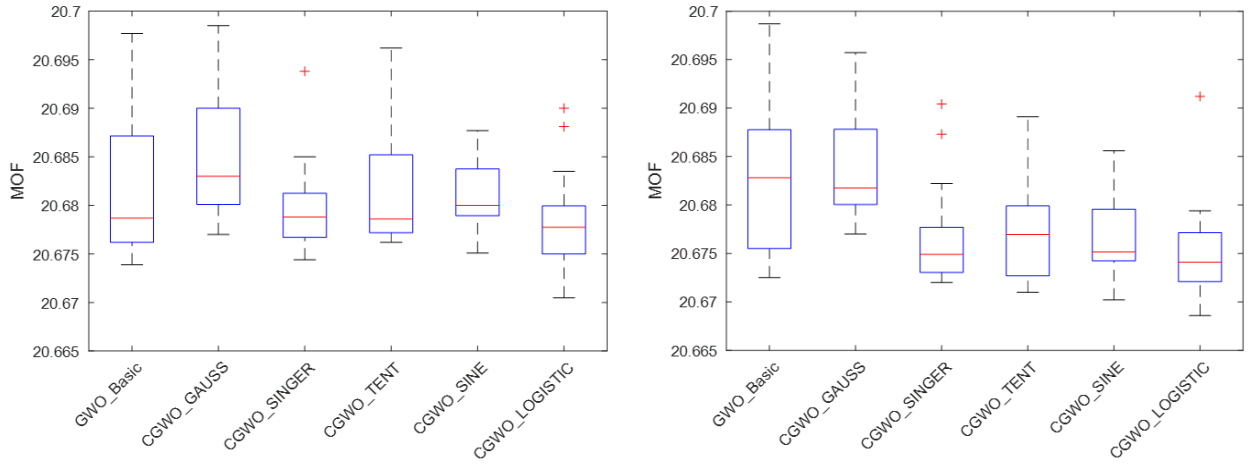

a *b*

Fig. 4. Boxplot of CGWO algorithms for the IEEE 33-bus:
a – PVDG; *b* – PVDG-BESS

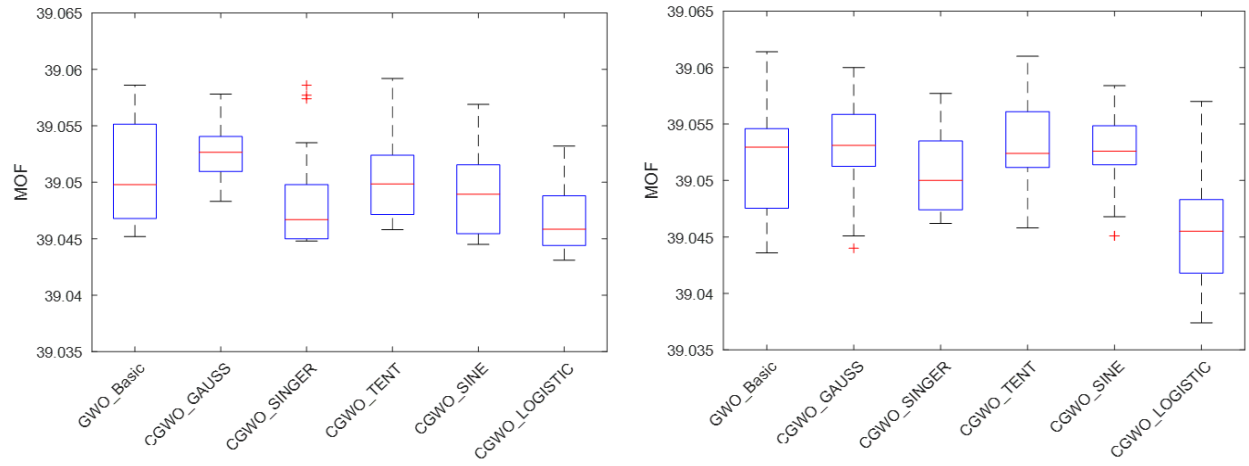

a *b*

Fig. 5. Boxplot of CGWO algorithms for the IEEE 69-bus:
a – PVDG; *b* – PVDG-BESS

For the purpose of improving the comparison and better evaluating of the utilized CGWO algorithms, a boxplot is presented as shown in Fig. 4, 5. The results were obtained while taking into account 20 runs for each applied algorithm. It can be noted for all the CGWO algorithms that the results are too close to their best and minimum MOF for all cases studies of optimal PVDG and hybrid PVDG-BESS integration in both test systems ADNs.

Besides, it is clear that the CGWO_Logistic algorithm showed efficiency and reliability when providing the lowest median and delivering the best and the minimum value of MOF in the two test systems for all cases studies.

Tables 1 and 3 show the optimal locations and sizes of both case studies (PVDG and hybrid PVDG-BESS) when applying the various CGWO algorithms on the two test systems ADNs.

Tables 2, 4 show the optimized parameters and the results obtained when optimally locate and size all cases studies (PVDG and hybrid PVDG-BESS) by various CGWO algorithms in both test systems ADNs.

From Tables 1–4 also when based on the comparison, it is clear among all the applied CGWO algorithms, that the best results and the minimum of MOF, was obtained by the CGWO_Logistic algorithm which provided the best values for the first test system ADN until 20.670 for the case of PVDG and until 20.668 for the case of hybrid PVDG-BESS. Meanwhile, for the IEEE 69-bus ADN the CGWO_Logistic algorithm provided the best MOF value of 39.043 for the case of PVDG and a value until 39.037 for the case of hybrid PVDG-BESS.

Table 1

Optimal location and sizing of all cases for the IEEE 33-bus

Algorithms applied	Cases	Optimal buses	Sizes (kW)
GWO Basic	PVDG	5-16-30	1446, 388.2, 405.4
	PVDG BESS	5-14-24 20-21-31	327.8, 492.4, 1001 -498.1, 516.8, 570.1
CGWO Gauss	PVDG	5-15-33	1242, 430.7, 408.7
	PVDG BESS	5-13-27 13-21-31	2091, 300.0, 458.1 5.7, 58.8, 477.6
CGWO Singer	PVDG	5-14-32	1579, 401.6, 421.8
	PVDG BESS	3-5-33 13-21-22	1140, 859.9, 480.7 457.7, -190.7, 239.7
CGWO Tent	PVDG	4-13-32	1935, 470.4, 406.1
	PVDG BESS	13-24-30 2-5-10	585.0, 761.7, 601.8 196.7, 5.5, 4.3
CGWO Sine	PVDG	5-15-33	1605, 392.6, 350.1
	PVDG BESS	3-25-33 5-16-25	361.2, 300.0, 405.4 1300.3, 372.2, 319.8
CGWO Logistic	PVDG	5-16-30	1503, 370.4, 400.2
	PVDG BESS	5-24-30 3-15-26	1346, 882.3, 488.9 -270, 477.5, -353.6

Table 2

Optimal results of all cases integration for the IEEE 33-bus

Algorithms applied	Cases	TAPL (kW)	TVD (p.u.)	TOT (sec)	MOF
Basic Case		210.987	1.812	20.574	–
GWO Basic	PVDG	95.612	1.088	19.495	20.674
	PVDG BESS	83.020	1.077	19.516	20.673
CGWO Gauss	PVDG	128.474	1.364	19.257	20.677
	PVDG BESS	104.813	1.079	19.524	20.677
CGWO Singer	PVDG	92.112	1.062	19.523	20.674
	PVDG BESS	87.252	1.046	19.541	20.672
CGWO Tent	PVDG	93.014	1.060	19.525	20.676
	PVDG BESS	87.510	1.103	19.491	20.671
CGWO Sine	PVDG	124.961	1.318	19.293	20.675
	PVDG BESS	86.372	1.058	19.525	20.670
CGWO Logistic	PVDG	96.115	1.090	19.493	20.670
	PVDG BESS	87.397	1.066	19.521	20.668

Table 3

Optimal location and sizing of all cases for the IEEE 69-bus

Algorithms applied	Cases	Optimal buses	Sizes (kW)
GWO Basic	PVDG	47-63-69	448.8, 946.4, 389.2
	PVDG BESS	4-12-61 13-64-68	1755, 581.5, 691.5 -143.0, 225.6, 151.0
CGWO Gauss	PVDG	4-60-69	1410, 1073, 459.7
	PVDG BESS	5-63-69 3-5-62	670.5, 433.5, 300.0 272.1, -1301, 540.2
CGWO Singer	PVDG	12-38-62	388.8, 408.6, 974.4
	PVDG BESS	14-49-61 4-8-56	315.3, 477.4, 1192 241.5, 69.8, -444.3
CGWO Tent	PVDG	57-61-69	349.4, 772.7, 381.9
	PVDG BESS	12-56-69 2-52-61	453.0, 444.8, 326.9 -550.1, -1200, 959.6
CGWO Sine	PVDG	5-61-69	443.2, 982.9, 355.6
	PVDG BESS	49-61-69 8-53-69	434.1, 1097, 326.9 2.7, -690.6, 704.7
CGWO Logistic	PVDG	4-61-69	707.2, 996.8, 348.9
	PVDG BESS	16-50-61 10-36-59	320.5, 349.3,1256 -147.0, 228.8, 280.4

Table 4

Optimal results of all cases integration for the IEEE 69-bus

Algorithms applied	Cases	TAPL (kW)	TVD (p.u.)	TOT (sec)	MOF
Basic case		224.945	1.870	38.772	---
GWO Basic	PVDG	104.063	1.304	37.647	39.045
	PVDG BESS	100.870	1.263	37.690	39.044
CGWO Gauss	PVDG	102.901	1.257	37.697	39.048
	PVDG BESS	104.972	1.330	37.620	39.045
CGWO Singer	PVDG	101.424	1.296	37.657	39.045
	PVDG BESS	98.993	1.280	37.667	39.047
CGWO Tent	PVDG	100.252	1.274	37.681	39.046
	PVDG BESS	108.550	1.271	37.675	39.046
CGWO Sine	PVDG	101.633	1.304	37.648	39.045
	PVDG BESS	102.082	1.264	37.678	39.045
CGWO Logistic	PVDG	101.078	1.303	37.649	39.043
	PVDG BESS	78.497	1.137	37.821	39.037

The rest of the applied algorithms also reveal a good efficiency in delivering the best results, but in terms of each parameter on its own, where, as example for the IEEE 33-bus ADN, the CGWO_Singer algorithm delivered the minimum TAPL's value of 92.112 kW, while the CGWO_Tent algorithm delivered the minimum TVD's value of 1.060 p.u. for the case of PVDG, also the GWO_Basic algorithm delivered the minimum TAPL's value of 83.020 kW for the case of hybrid PVDG-BESS. Meanwhile, for the second test system ADN, as example, the GWO_Tent provided the minimum TAPL's value of 100.252 kW and the GWO_Basic algorithm provided the minimum TOT's value of 37.647 seconds for the case of PVDG, while the GWO_Gauss algorithm delivered the minimum TOT's value of 37.620 seconds for the case of hybrid PVDG-BESS.

Figure 6 demonstrates the comparison of active power losses between the basic case and both cases of optimal PVDG and hybrid PVDG-BESS presence in both test systems ADNs.

From Fig. 6, and the previous results, it is noted that the optimal allocation of PVDG and hybrid PVDG-BESS using the CGWO_Logistic algorithm in the two test systems, contributed excellently and directly to the minimizing of the active power losses in almost all branches of both ADNs, especially in branches which situated near to the optimally located buses of both cases integration in the two test systems, with superior and much better results for the second case study with the integration of hybrid PVDG-BESS.

Also, this comparison could be improved when basing on the TAPL value, where it is reduced at the first system IEEE 33-bus ADN, from value of 210.987 kW at the basic case to 96.115 kW for the case of PVDG, and until 87.397 kW for the case of hybrid PVDG-BESS.

For the second system ADN, the TAPL got reduced from 224.947 kW to 101.078 kW for the case of PVDG and reduced until 78.497 kW for the case of hybrid PVDG-BESS installation.

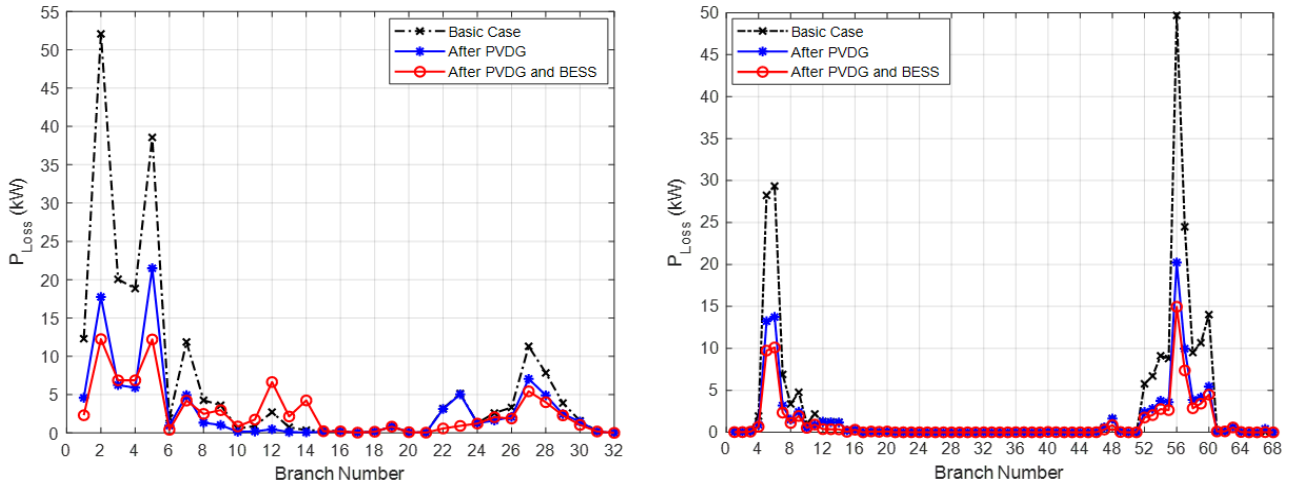

a *b*

Fig. 6. Active power losses in branches:
a – IEEE 33-bus; *b* – IEEE 69-bus

Figure 7 represents the voltage deviation for all cases studies of the optimal integration of PVDG and hybrid PVDG-BESS units in the two standards test systems ADNs.

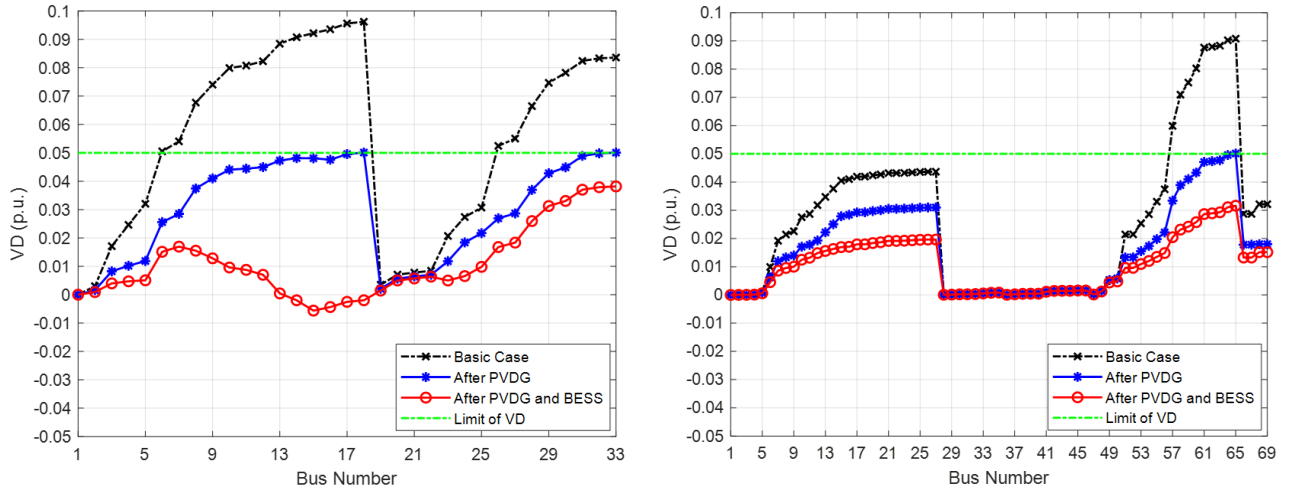

a *b*

Fig. 7. Bus voltage deviation:
a – IEEE 33-bus; *b* – IEEE 69-bus

When analyzing Fig. 7, it may be noticed that the voltage deviation at the basic case was above the limited value of 0.05 p.u. in most buses of the two test systems ADNs. Moreover, it may be observed after the optimal integration of PVDG and the hybrid PVDG-BESS into ADNs by the CGWO_Logistic algorithm, that the voltage deviation got minimized under the allowed range in all test systems' buses with superior and better results provided by the second case with the integration of hybrid PVDG-BESS systems.

Also, by checking the value of TVD, it is seen for the first system, the TVD minimized from 1.812 p.u. to 1.090 p.u. for the case of PVDG and until 1.066 p.u. for the case of hybrid PVDG-BESS. For the second system, TVD reduced from 1.870 p.u. to 1.303 p.u. for the case of PVDG and until 1.137 p.u. for the case of hybrid PVDG-BESS.

Figure 8 represents the bus voltage profiles for all cases studies of the optimal integration of PVDG and hybrid PVDG-BESS units in the two standard test systems ADNs.

From Fig. 8, it may note that the voltage profiles have improved in all buses of both standards test systems ADNs after the optimal integration of both cases studies of PVDG and hybrid PVDG-BESS units, with much better and superior results for the second case of hybrid PVDG-BESS. Also, this voltage profiles' ameliorating was especially in the buses which situated close to the optimally located buses of both cases studies integration into test systems ADNs.

As mentioned previously in Fig. 7, the minimization of the voltage deviation, consequently led to the enhancement of the voltage profiles, due to the fact that the voltage deviation is represented as the difference between the nominal voltage of 1 p.u., and the voltage value at the basic case.

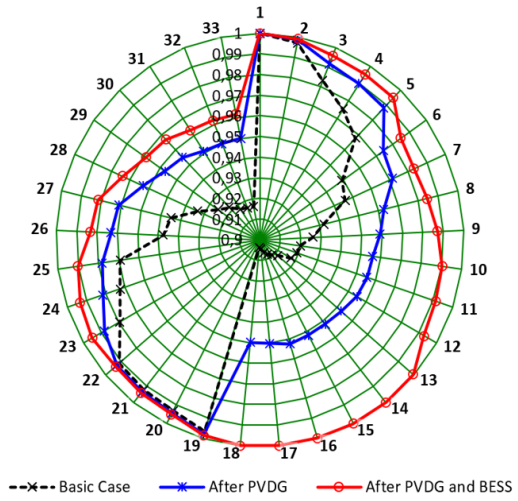

a

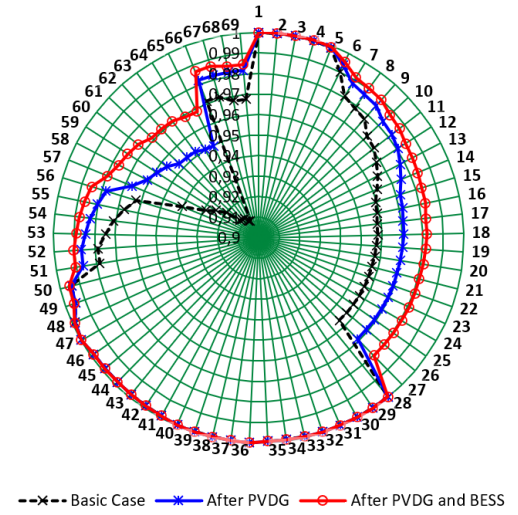

b

Fig. 8. Voltage profiles of buses:
a – IEEE 33-bus; *b* – IEEE 69-bus

Figure 9 illustrates the primary overcurrent relays' operation time with two different zones of zoom for the basic case and after all cases studies integration of PVDG and hybrid PVDG-BESS into both standards test systems ADNs.

When comparing to the basic case, it is clear that the operation time in most of the primary NS-OCRs had considerably minimized after the optimal integration of PVDG and hybrid PVDG-BESS into both test systems ADNs by the CGWO_Logistic algorithm. Besides, the TOT was decreased at the first system IEEE 33-bus ADN from 20.574 seconds to 19.493 seconds for the case of PVDG and until 19.521 seconds for the case of hybrid PVDG-BESS. Also, it is mentioned a clear impact of operation time's minimization in both zones of zoom in Fig. 9,*a*, between NS-OCRs from 12 to 14 and from 23 to 25, for both cases studies.

For the IEEE 69-bus ADN, the TOT decreased from 38.772 seconds to 37.649 seconds for the case of PVDG and until 37.821 seconds for the case of hybrid PVDG-BESS, where that impact of operation time's minimization is obvious in both zones of zoom in Fig. 9,*b* between NS-OCRs from 10 to 13 and from 50 to 54, for both cases studies. Hence, according to equation (8), this

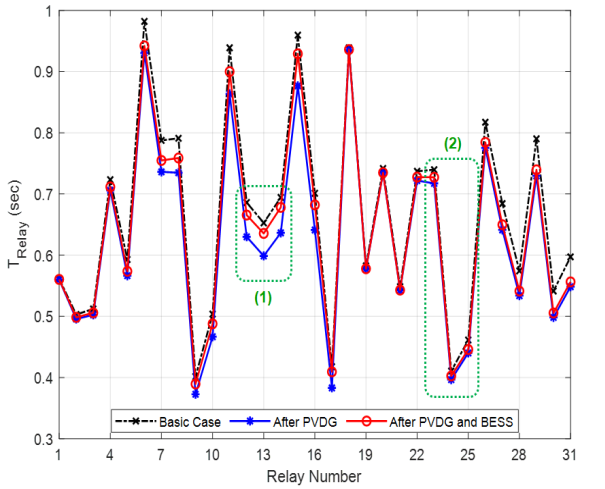

a

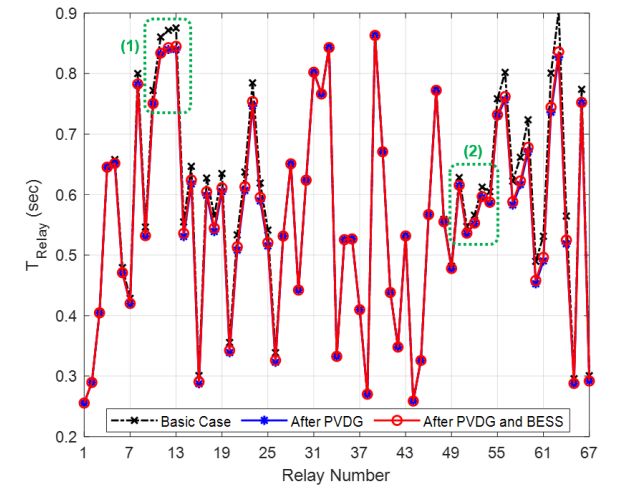

b

Fig. 9. Overcurrent relay operation time:
a – IEEE 33-bus; *b* – IEEE 69-bus

minimization was due to the inverse function between the fault current and the fault voltage magnitude covered by the NS-OCR and its operation time, where the more I_F and V_{FM} increased, the NS-OCR will operate quickly to clear the faults.

5. Conclusion.

In this paper, a study of comparison was carried out between the various chaotic grey wolf optimization

algorithms to identify the optimal allocation of multiple photovoltaic distributed generation and hybrid photovoltaic distributed generation and battery energy storage systems, into the active distribution networks based on solving the multi-objective function which represented as reducing simultaneously the three technically parameters: total voltage deviation, total active power losses and the overcurrent relays' total operation time.

The simulation results confirm the robustness and efficiency of the chaotic logistic grey wolf optimization algorithm, compared to the rest of the applied algorithms, in terms of providing the best and minimum multi-objective functions-based power losses, voltage deviation, and overcurrent relay operation time's values, but including a late convergence characteristic. The comparison between the attained results of simulation for various cases studied led toward the conclusion that best results were achieved when the photovoltaic distributed generation and battery energy storage systems were simultaneously optimally allocated, which drove to a significant minimization of power losses, ameliorating of the voltage profiles, and improvement of the overcurrent protection system in the active distribution networks studies.

Based on the previous discussion, the future work will focus on implementing the Distributed Static Var Compensator in addition to the battery energy storage systems to improve the performance of the studies systems, while considering new technical indices, also the distributed generation power outputs and the load demand variation at the different sessions of the year.

Conflict of interest. The authors declare that they have no conflicts of interest.

REFERENCES

1. Lai C.S., Jia Y., Lai L.L. A comprehensive review on large-scale photovoltaic system with applications of electrical energy storage. *Renewable and Sustainable Energy Reviews*, 2017, vol. 78, pp. 439-451. doi: https://doi.org/10.1016/j.rser.2017.04.078.

2. Wong L.A., Ramachandaramurthy V.K., Taylor P., Ekanayake J.B., Walker S.L., Padmanaban S. Review on the optimal placement, sizing and control of an energy storage system in the distribution network. *Journal of Energy Storage*, 2019, vol. 21, pp. 489-504. doi: https://doi.org/10.1016/j.est.2018.12.015.

3. Macedo L.H., Franco J.F., Rider M.J., Romero R. Optimal operation of distribution networks considering energy storage devices. *IEEE Transactions on Smart Grid*, 2015, vol. 6, no. 6, pp. 2825-2836. doi: https://doi.org/10.1109/tsg.2015.2419134.

4. Hemmati R. Mobile model for distributed generations and battery energy storage systems in radial grids. *Journal of Renewable and Sustainable Energy*, 2019, vol. 11, no. 2, p. 025301. doi: https://doi.org/10.1063/1.5079698.

5. Home-Ortiz J.M., Pourakbari-Kasmaei M., Lehtonen M., Sanches Mantovani J.R. Optimal location-allocation of storage devices and renewable-based DG in distribution systems. *Electric Power Systems Research*, 2019, vol. 172, pp. 11-21. doi: https://doi.org/10.1016/j.epsr.2019.02.013.

6. Santos S.F., Fitiwi D.Z., Cruz M.R.M., Cabrita C.M.P., Catalão J.P.S. Impacts of optimal energy storage deployment and network reconfiguration on renewable integration level in distribution systems. *Applied Energy*, 2017, vol. 185, pp. 44-55. doi: https://doi.org/10.1016/j.apenergy.2016.10.053.

7. Zafar R., Ravishankar J., Fletcher J.E., Pota H.R. Multi-timescale model predictive control of battery energy storage system using conic relaxation in smart distribution grids. *IEEE Transactions on Power Systems*, 2018, vol. 33, no. 6, pp. 7152-7161. doi: https://doi.org/10.1109/tpwrs.2018.2847400.

8. Bai L., Jiang T., Li F., Chen H., Li X. Distributed energy storage planning in soft open point based active distribution networks incorporating network reconfiguration and DG reactive power capability. *Applied Energy*, 2018, vol. 210, pp. 1082-1091. doi: https://doi.org/10.1016/j.apenergy.2017.07.004.

9. Lei J., Gong Q. Operating strategy and optimal allocation of large-scale VRB energy storage system in active distribution networks for solar/wind power applications. *IET Generation, Transmission & Distribution*, 2017, vol. 11, no. 9, pp. 2403-2411. doi: https://doi.org/10.1049/iet-gtd.2016.2076.

10. Alharthi H., Alzahrani A., Shafiq S., Khalid M. Optimal allocation of batteries to facilitate high solar photovoltaic penetration. *9th International Conference on Power and Energy Systems (ICPES 2019),* Perth, Australia, 2019. doi: https://doi.org/10.1109/icpes47639.2019.9105479.

11. Ahmed H.M.A., Awad A.S.A., Ahmed M.H., Salama M.M.A. Mitigating voltage-sag and voltage-deviation problems in distribution networks using battery energy storage systems. *Electric Power Systems Research*, 2020, vol. 184, art. no. 106294. doi: https://doi.org/10.1016/j.epsr.2020.106294.

12. Sardi J., Mithulananthan N., Gallagher M., Hung D.Q. Multiple community energy storage planning in distribution networks using a cost-benefit analysis. *Applied Energy*, 2017, vol. 190, pp. 453-463. doi: https://doi.org/10.1016/j.apenergy.2016.12.144.

13. Zheng Y., Hill D.J., Dong Z.Y. Multi-agent optimal allocation of energy storage systems in distribution systems. *IEEE Transactions on Sustainable Energy,* 2017, vol. 8, no. 4, pp. 1715-1725. doi: https://doi.org/10.1109/tste.2017.2705838.

14. Zhang Y., Xu Y., Yang H., Dong Z.Y. Voltage regulation-oriented co-planning of distributed generation and battery storage in active distribution networks. *International Journal of Electrical Power and Energy Systems*, 2019, vol. 105, pp. 79-88. doi: https://doi.org/10.1016/j.ijepes.2018.07.036.

15. Gao J., Chen J.-J., Cai Y., Zeng S.-Q., Peng K. A two-stage Microgrid cost optimization considering distribution network loss and voltage deviation. *Energy Reports*, 2020, vol. 6, no. 2, pp. 263-267. doi: https://doi.org/10.1016/j.egyr.2019.11.072.

16. Luo L., Abdulkareem S.S., Rezvani A., Miveh M.R., Samad S., Aljojo N., Pazhoohesh M. Optimal scheduling of a renewable based microgrid considering photovoltaic system and battery energy storage under uncertainty. *Journal of Energy Storage*, 2020, vol. 28, art. no. 101306. doi: https://doi.org/10.1016/j.est.2020.101306.

17. Chen J., Jiang X., Li J., Wu Q., Zhang Y., Song G., Lin D. Multi-stage dynamic optimal allocation for battery energy storage system in distribution networks with photovoltaic system. *International Transactions on Electrical Energy Systems*, 2020, vol. 30, no. 12, art. no. e12644. doi: https://doi.org/10.1002/2050-7038.12644.

18. Khalid M., Akram U., Shafiq S. Optimal planning of multiple distributed generating units and storage in active distribution networks. *IEEE Access*, 2018, vol. 6, pp. 55234-55244. doi: https://doi.org/10.1109/access.2018.2872788.

19. Wong L.A., Ramachandaramurthy V.K., Walker S.L., Taylor P., Sanjari M.J. Optimal placement and sizing of battery energy storage system for losses reduction using whale optimization algorithm. *Journal of Energy Storage*, 2019, vol. 26, art. no. 100892. doi: https://doi.org/10.1016/j.est.2019.100892.

20. Mukhopadhyay B., Das D. Multi-objective dynamic and static reconfiguration with optimized allocation of PV-DG and battery energy storage system. *Renewable and Sustainable Energy Reviews*, 2020, vol. 124, art. no. 109777. doi: https://doi.org/10.1016/j.rser.2020.109777.

21. Qian X., Zhang S., Liu J., Zheng Y., Liu W. Hierarchical optimal planning of battery energy storage systems in radial distribution networks. *3rd IEEE Conference on Energy Internet*

and Energy System Integration (EI2 2019), Changsha, China 2019. doi: https://doi.org/10.1109/EI247390.2019.9061757.
22. Ahmadi B., Ceylan O., Ozdemir A. Voltage profile improving and peak shaving using multi-type distributed generators and battery energy storage systems in distribution networks. *55th International Universities Power Engineering Conference (UPEC 2020)*, Italy, 2020. doi: https://doi.org/10.1109/upec49904.2020.9209880.
23. Valencia A., Hincapie R.A., Gallego R.A. Optimal location, selection, and operation of battery energy storage systems and renewable distributed generation in medium–low voltage distribution networks. *Journal of Energy Storage*, 2021, vol. 34, art. no. 102158. doi: https://doi.org/10.1016/j.est.2020.102158.
24. Mirjalili S., Mirjalili S.M., Lewis A. Grey wolf optimizer. *Advances in Engineering Software*, 2014, vol. 69, pp. 46-61. doi: https://doi.org/10.1016/j.advengsoft.2013.12.007.
25. Lu C., Gao L., Li X., Hu C., Yan X., Gong W. Chaotic-based grey wolf optimizer for numerical and engineering optimization problems. *Memetic Computing*, 2020, vol. 12, no. 4, pp. 371-398. doi: https://doi.org/10.1007/s12293-020-00313-6.
26. Settoul S., Chenni R., Hassan H.A., Zellagui M., Kraimia M.N. MFO Algorithm for optimal location and sizing of multiple photovoltaic distributed generations units for loss reduction in distribution systems. *7th International Renewable and Sustainable Energy Conference (IRSEC 2019)*. Morocco, 2019. doi: https://doi.org/10.1109/irsec48032.2019.9078241.
27. Zellagui M., Settoul S., Lasmari A., El-Bayeh C.Z., Chenni R., Hassan H.A. Optimal allocation of renewable energy source integrated-smart distribution systems based on technical-economic analysis considering load demand and DG uncertainties. *Lecture Notes in Networks and Systems*. 2021, vol. 174, pp. 391-404. doi: https://doi.org/10.1007/978-3-030-63846-7_37.
28. Belbachir N., Zellagui M., Lasmari A., El-Bayeh C.Z., Bekkouche B. Optimal PV sources integration in distribution system and its impacts on overcurrent relay based time-current-voltage tripping characteristic. *12th International Symposium on Advanced Topics in Electrical Engineering (ATEE 2021),* Romania, 2021. doi: https://doi.org/10.1109/atee52255.2021.9425155.
29. Lasmari A., Zellagui M., Hassan H.A., Settoul S., Abdelaziz A.Y., Chenni R. Optimal energy-efficient integration of photovoltaic DG in radial distribution systems for various load models. *11th International Renewable Energy Congress, (IREC 2020),* Tunisia, 2020. doi: https://doi.org/10.1109/irec48820.2020.9310429.
30. Saleh K.A., Zeineldin H.H., Al-Hinai A., El-Saadany E.F. Optimal coordination of directional overcurrent relays using a new time-current-voltage characteristic. *IEEE Transactions on Power Delivery.* 2015, vol. 30, pp. 537-544. doi: https://doi.org/10.1109/TPWRD.2014.2341666.
31. Saremi S., Mirjalili S.Z., Mirjalili S.M. Evolutionary population dynamics and grey wolf optimizer. *Neural Computing and Applications*, 2015, vol. 26, no. 5, pp. 1257-1263. doi: https://doi.org/10.1007/s00521-014-1806-7.
32. Saremi S., Mirjalili S., Lewis A. Biogeography-based optimization with chaos. *Neural Computing and Applications*, 2014, vol. 25, no. 5, pp. 1077-1097. doi: https://doi.org/10.1007/s00521-014-1597-x.

Received 12.05.2021
Accepted 14.06.2021
Published 25.06.2021

Nasreddine Belbachir[1], *PhD Student,*
Mohamed Zellagui[2], *PhD, Associate Professor,*
Samir Settoul[3], *PhD Student,*
Claude Ziad El-Bayeh[4], *PhD, Postdoctoral Research,*
Benaissa Bekkouche[1], *PhD, Professor,*
[1] Department of Electrical Engineering,
University of Mostaganem, Mostaganem, 27000, Algeria,
e-mail: n.belbachir@ieee.org (Corresponding author),
benaissa.bekkouche@univ-mosta.dz
[2] Department of Electrical Engineering,
University of Batna 2, Fesdis, Batna, 05078, Algeria,
e-mail: m.zellagui@ieee.org, m.zellagui@univ-batna2.dz
[3] Department of Electrotechnic,
Mentouri University of Constantine 1,
Constantine, 25000, Algeria,
e-mail: samir.settoul@umc.edu.dz
[4] Canada Excellence Research Chairs Team,
Concordia University,
Montreal, Quebec, H3G 1M8, Canada,
e-mail: c.bayeh@hotmail.com

How to cite this article:
Belbachir N., Zellagui M., Settoul S., El-Bayeh C.Z., Bekkouche B. Simultaneous optimal integration of photovoltaic distributed generation and battery energy storage system in active distribution network using chaotic grey wolf optimization. *Electrical Engineering & Electromechanics*, 2021, no. 3, pp. 52-61. doi: https://doi.org/10.20998/2074-272X.2021.3.09.

UDC 662.997+697.7 https://doi.org/10.20998/2074-272X.2021.3.10

V.V. Wysochin, V.R. Nikulshin, A.E. Denysova

INVESTIGATION OF ORIENTATION IMPACT ON ELECTRICAL POWER OF BIFACIAL SOLAR ELEMENTS

Purpose. *To develop the integrated mathematical model for definition of bifacial solar element rational power operation in the various operation conditions caused by orientation of solar panels and power influence.* ***Methodology.*** *We have proposed the method of definition of bifacial solar elements irradiation and temperature mode and also electric power production at various orientation of panels.* ***Results****. We have made analytical investigations of temperature operation conditions of solar elements and their influence on electrical power for various panels orientation in space. Features of irradiation of the forward and back parts of solar panels, conditions of a temperature operating mode and its influence on electric power production are shown. Possibilities of rational conditions of spatial panels orientation are considered.* ***Originality****. We have suggested and proved the model of definition bifacial irradiation solar panels and thermal conditions of electric power production and also rational conditions of spatial orientation of panels.* ***Practical value****. The developed by us methodology as well as results of its application, allows to choose rational architecture of a solar power station with high efficiency.* References 13, figures 5.
Key words: **bifacial solar photo panels, irradiation of solar panels, orientation of solar cells, power generation.**

Розроблений метод аналітичного визначення опромінення, температурного режиму, а також вироблення електроенергії двосторонніх сонячних елементів при різній орієнтації панелей. Створено інтегральну математичну модель для оцінки енергетичного режиму роботи сонячних елементів при змінних кліматичних умовах і просторових настановних характеристик. Проведені аналітичні дослідження роботи сонячних елементів. Показані особливості опромінення передньої й тильної сторін сонячних панелей, умови формування температурного режиму роботи і його впливу на вироблення електроенергії. Розглянуто можливості формування раціональних умов просторової орієнтації панелей за фактором електричної продуктивності. Використання запропонованої методики й результатів аналізу, проведених на її основі, дозволяє вибрати раціональну архітектуру сонячної електростанції високої ефективності. Бібл. 13, рис. 5.
Ключові слова: **двосторонні сонячні фотопанелі, опромінення сонячних панелей, орієнтація сонячних елементів, виробництво електроенергії**.

Разработан метод аналитического определения облучения, температурного режима, а также выработки электроэнергии двухсторонних солнечных элементов при различной ориентации панелей. Создана интегральная математическая модель для оценки энергетического режима работы солнечных элементов при переменных климатических условиях и пространственных установочных характеристиках. Проведены аналитические исследования работы солнечных элементов. Показаны особенности облучения передней и тыльной сторон солнечных панелей, условия формирования температурного режима работы и его влияния на выработку электроэнергии. Рассмотрены возможности формирования рациональных условий пространственной ориентации панелей по фактору электрической производительности. Использование предложенной методики и результатов анализа, проведенных на ее основе, позволяет выбрать рациональную архитектуру солнечной электростанции высокой эффективности. Библ. 13, рис. 5.
Ключевые слова: **двухсторонние солнечные фотопанели, облучение солнечных панелей, ориентация солнечных элементов, производство электроэнергии**.

Introduction. Bifacial solar cells (SEs) have emerged as a result of the search for methods for the most efficient use of a valuable semiconductor layer that absorbs solar radiation for power generation [1-4]. Their advantage is the additional irradiation of the absorber from the back of the SE, which is not carried out in conventional one-acial devices. Obviously, the radiation is related to the orientation of the SE relative to its radiation source. Bifacial irradiation affects the energy balance by changing the operating parameters of SE: operating temperature and power generation, which are known to be interdependent [4, 5].

Stimulation of radiation intensity leads to a change in energy balance – not always in the direction of increasing efficiency. This fact imposes restrictions on the applicability of such devices, causing the need for additional measures to change the way the organization of the SE operation.

Analysis of recent research and publications. Considerable attention is paid to the study of temperature conditions of solar elements [3-7]. Existing models for determining the energy performance of solar elements are based on the idea of one-facial frontal irradiation of the device. However, the back side, perceiving the radiant energy, has a corresponding effect on the overall energy balance [3, 4]. Among the various factors influencing the radiation, from the point of view of operating mode control, the geometric, i.e. the spatial location of the solar elements is important. Different options are offered to choose the orientation of bifacial solar panels [8, 9], but they do not have sufficient justification, in particular, the impact of the radiation component on the back of the panel is not taken into account. Therefore, the analysis of the real operating conditions of the solar elements requires a model that describes the features of the absorber irradiation and the influence of the orientation of the SE on energy processes.

Mathematical models used for research include radiation [3, 4, 7, 10, 11] and convective components as external conditions. The latter is usually associated with wind interaction [5, 8]. Both components depend on the

orientation of the panel. The description of the influence of the radiation component on the frontal surface can be based on sufficiently reliable model representations [6-8, 11-13].

For the back side, in [4] studies of the effect of reflectivity of different surfaces were conducted. In [3], a dynamic three-layer model of the solar element is proposed, which includes the radiation component of the interaction with the back side. The results showed an increase in temperature in the bifacial panels, taking into account the radiation. But the effect of irradiation in the dynamics of diurnal and seasonal changes in orientation relative to the source is not shown.

The method [10] developed for the conditions of Ukraine can be used for the analytical description of surface irradiation. According to it, the intensity of the radiation flux is determined for the horizontal surface as a function of geographical parameters, seasonality and time of day. Correction R, which specifies the slope and orientation of the surface, which is represented as the ratio of the flux of direct solar radiation, which flows normally on the inclined surface, to the radiation flux on the horizontal surface, is defined as:

$$R = \left(1 - \frac{H_d}{H}\right) R_b + \frac{H_d}{H} \cdot \frac{1+\cos\beta}{2} + \frac{1-\cos\beta}{2} \cdot \rho, \quad (1)$$

where H_d is the arrival of diffusion radiation on the horizontal surface as part of the integrated radiation on the horizontal surface H; R_b is the ratio of direct solar radiation on the inclined and horizontal surface; β is the angle of inclination of the surface; ρ is the reflectivity of the soil.

This dependence can be applied to the surface on the south side. It takes into account the direct solar radiation (the first term), scattered in the atmosphere one (the second term, which shows which part of the sky is visible from the surface), and reflected from the earth's surface (the third term, which shows the proportion of reflected total radiation). There are no similar methodological provisions for the back side of the surface.

The goal of the work is to develop a method for determining the radiation and energy performance of bifacial solar elements; creation on its basis of the integrated mathematical model concerning studying of an energy mode of operation of SE in various climatic and installation conditions of operation; study of energy modes of SE operation.

A mathematical model. The following terminology is used to formalize the problem of the location of the solar panel. Orientation along the «south-north» (S-N) is realized when the normal to the front (obverse) surface of the solar panel is directed to the south with an azimuth of 0 degrees. Orientation «east-west» (E-W) determines the direction of the normal of the obverse surface to the east.

For the back side of the receiver oriented on the S-N axis, the direct component is absent, respectively, the component of the reflected radiation for the reverse side should not include direct radiation. Thus, for the back side of the surface oriented along the S-N axis, the ratio of radiation fluxes R_r is determined as

$$R_r = \frac{H_d}{H}\left(\frac{1-\cos\beta}{2} + \frac{1+\cos\beta}{2}\rho\right). \quad (2)$$

For surfaces oriented along the E-W axis, the calculation method is the same, but for the surface «east» orientation the azimuth angle γ = + 90°, for «west» γ = –90°. The straight component for the back side appears after noon at the zenith angle $\theta_Z \geq 90 - \beta$.

The energy balance of the bifacial SE has its own peculiarities. Irradiation of external surfaces is the same as for a one-facial battery. Radiant energy is absorbed by both the front and back sides of the SE. However, in one-facial SE, the active beam-absorbing surface (absorber) is irradiated only on one side – the front one. The energy supplied to the back side is not involved in the process of electricity production – it is spent on heating the device, including the absorber. In the bifacial SE, the absorber is irradiated on two sides. But the irradiation of the absorber from the back side is characterized by the fact that this side has a special translucent coating to reduce electron-hole recombination of charge carriers. Therefore, the radiation transmission from the back side is less than from the front side. Accordingly, the optical characteristics ($\tau\alpha$), which determine the transmission of the transparent coating and the absorption of the absorber, for the front and back sides are different.

The energy balance equation for bifacial SE can be represented as

$$[H \cdot R \cdot (\tau\alpha) \cdot (1-\eta_{ph})]_a + [H \cdot R \cdot (\tau\alpha) \cdot (1-\eta_{ph})]_r = \\ = U \cdot (T_{ab} - T_a), \quad (3)$$

where η_{ph} is the coefficient of efficiency of conversion of solar energy into electricity (efficiency); U is the heat loss coefficient; T_{ab} is the absorber temperature; T_a is the outside air temperature; indices: a – the obverse side of the SE; r – the reverse side of the CE.

Usually they try by adjusting to maintain the value of the efficiency η_{ph} on the maximum level of $\eta_{ph} = \eta_{ph.\max}$. The coefficient $\eta_{ph.\max}$ depends on various factors and, in particular, on temperature. The dependence of $\eta_{ph.\max}$ on the temperature in the region of positive temperatures can be described as follows [12]

$$\eta_{ph.\max} = \eta_{\max ST} \cdot [1 + \alpha_p \cdot (T_{ab} - T_{ST})], \quad (4)$$

where $\eta_{\max ST}$ is the efficiency of the solar element at the point of maximum power under standard conditions; α_p is the temperature power factor of the SE, K^{-1}; T_{ST} is the temperature of the solar element under standard conditions.

Under standard conditions they understand the following: the flux density of solar radiation H_{ST} = 1 kW/m^2, the surface temperature of the SE T_{ST} = 25 °C.

For the bifacial element, the efficiency is determined for each of the sides under the same irradiation conditions. At one-facial irradiation of the absorber the equation of energy balance will differ by the absence for the reverse side of the factor of conversion of solar energy into electric energy: $(1 - \eta_{ph})_r$.

The solution of the energy equation taking into account the presented dependencies on the temperature of the absorber of bifacial radiation has the form

$$T_{ab} = \frac{[H \cdot R \cdot (\tau\alpha)]_a + [H \cdot R \cdot (\tau\alpha)]_r - (1 - \alpha_p T_{ST}) \cdot \{K\} + U \cdot T_a}{U + \alpha_p \cdot \{K\}}, \quad (5)$$

where $\{K\} = \sum_{a,r} [H \cdot R \cdot (\tau\alpha) \cdot \eta_{\max ST}]_i$.

The electric power of the SE should be found taking into account its temperature [12]

$$P = P_{rat} \cdot k_{r.e} \frac{H}{H_{ST}} [1 + \alpha_p \cdot (T_{ab} - T_{ST})], \quad (6)$$

where P_{rat} is the rated power of the SE under standard conditions; $k_{r.e}$ is the coefficient of reduction of efficiency of the SE.

At one-facial irradiation of the absorber $H = H_a$. At bifacial irradiation, electricity generation is not a linear function of the joint irradiation of the front and rear sides [13]. This factor is taken into account by the coefficient of bifacial efficiency η_e. Therefore, effective irradiation can be represented as

$$H = H_a + H_r \cdot \eta_e = H \cdot R_a + H \cdot R_r \cdot \eta_e . \quad (7)$$

Analysis of the energy mode in different ways of orientation. The research was conducted for the conditions of Ukraine at latitude 46°.

Features of electricity production are due to two factors. The first one is the radiation intensity of the panel. Intensity correlates well with electricity production. Therefore, such a factor can be considered the main one. The second factor is the heating temperature of the absorber, the growth of which reduces the efficiency of the battery and reduces its service life.

Heating of the absorber is characterized by a significantly variable nature of the temperature versus time of day (Fig. 1). With the S-N orientation, the temperature rises smoothly in the morning and decreases in the afternoon. The view of the dependence curves throughout the year and for different angles of inclination is symmetrical with respect to noon time. The temperature of the absorber in summer, as well as performance, largely depends on the angle of inclination, and in winter there is almost no such effect.

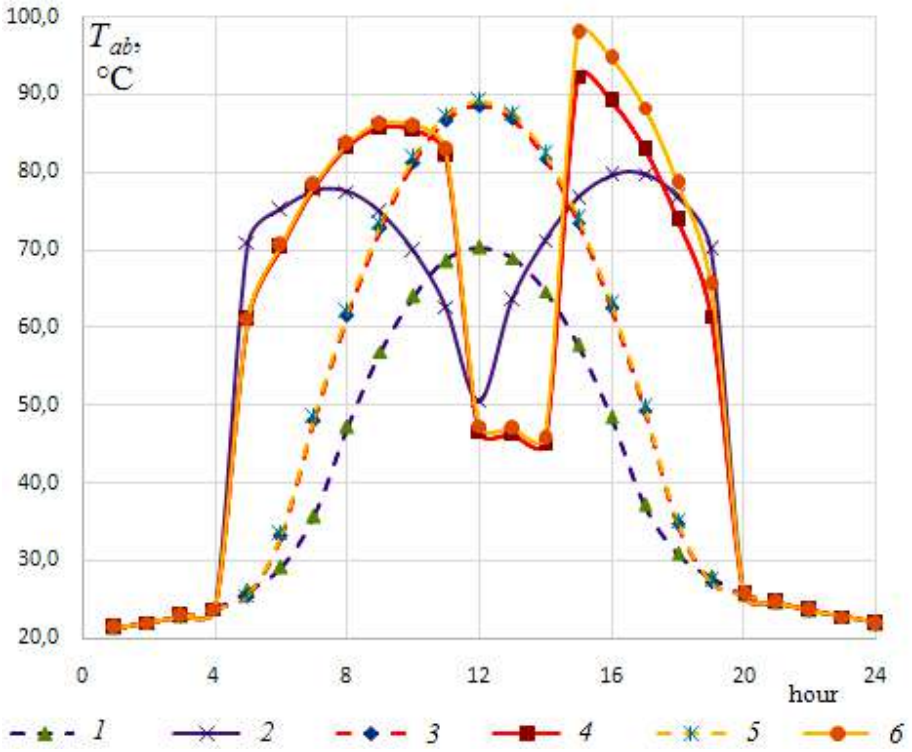

Fig. 1. Daytime thermogram of the absorber in the summer for various orientations, angles of inclination and types of the SE (one-facial – 1s, bifacial – 2s):
1 – S-N,90°,2s; 2 – E-W,90°,2s; 3 – S-N,45°,2s; 4 – E-W,45°,2s; 5 – S-N, 45°,1s; 6 – E-W,45°,1s

At E-W orientation change of temperature during the day is more difficult. Symmetry relative to noon is observed only in summer – for the vertical location of the panel. The type of temperature curves differs by a much larger integral filling of the graphical field in the morning and evening periods and the presence of a failure at noon, compared with the S-N orientation. This is due to the features of the panel irradiation.

The general trend determined by the analysis results is an increase in temperature with decreasing angle of inclination. In summer, when the temperature of the absorber is highest, its level exceeds that normally recommended for the SE (45-50 °C), and reaches a high value (in our example 94 °C).

Comparison of temperature modes of bifacial and one-acial panels shows (Fig. 1) that the heating levels of the absorber in the most heat-stressed period (summer) in both versions are almost the same. However, with the E-W orientation in the afternoon, the one-facial SE heats up more. This is due to the presence of excess heat with limited use of solar energy to generate electricity.

The similar heating temperatures of the absorber in the considered variants are explained by a small share of irradiation of the side of the SE, which is in the shade

(Fig. 2). Therefore, the front surface is decisive in the formation of the temperature of the absorber, both for one-facial and bifacial panels. The patterns of irradiation change are similar for angles of 90° and 45°, but the maximum value in the latter case is greater, although the irradiation intensity of the back panel is less.

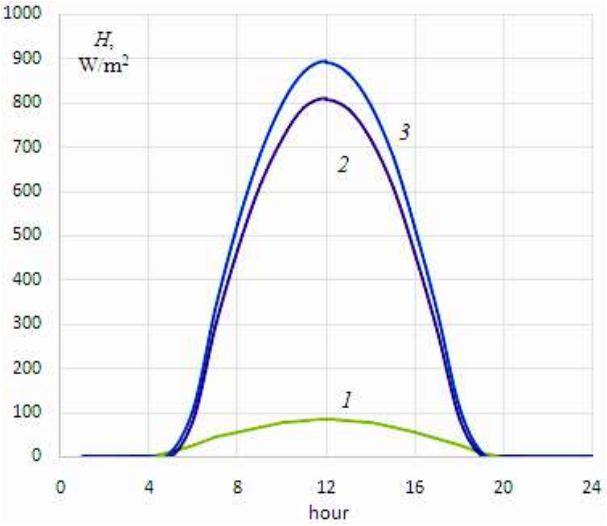

Fig. 2. Radiation flux density on the SE at S-N orientation and angle of inclination 45°
(direction of the sides: *1* – north; *2* – south; *3* – total)

Irradiation of the eastern side at the E-W orientation at the beginning of the day, from 4am to 12am, changes dramatically: there is an increase and subsequent decline with a significant rate (Fig. 3). After noon, the rate of decline decreases. In this part of the day, the irradiation of the reverse side is much less. The picture of the change in the irradiation of the sides at the E-W orientation is a mirror image of the noon time. In the afternoon, for some time the solar radiation does not fall on the back side of the inclined panel, so its total exposure during this period is less. When the zenith angle reaches the value $\theta_Z \geq 90 - \beta$, a straight component appears. For the vertical panel $\theta_Z = 0$ and this transition is almost imperceptible.

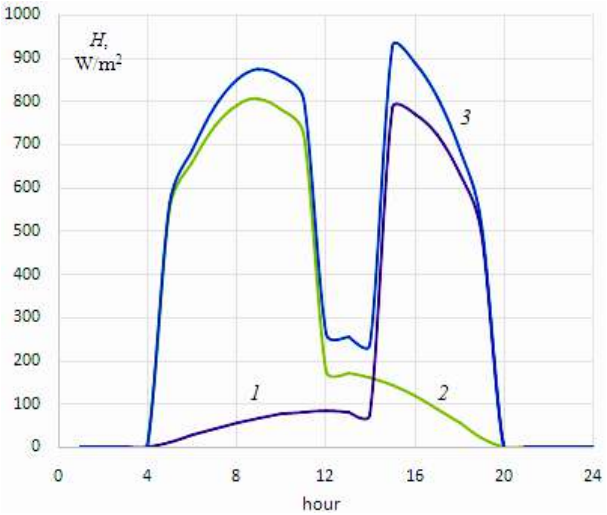

Fig. 3. Radiation flux density on the SE at E-W orientation and angle of inclination 45°
(direction of the sides: *1* – east; *2* – west; *3* – total)

Thus, in the first half of the day the intensity of radiation prevails on the obverse side, in the second one – on the reverse one, which determines the predominant influence of one of the sides on the heating. The total radiation, in contrast to that which falls on each side, is more smoothed, although with a decline in the afternoon.

Figure 4 presents data on the daily development of panel performance in the two considered orientations in the summer. At the direction along the S-N axis, the main time of electricity production is the middle of the day, for E-W – the beginning and end of the day. The same dependencies are characteristic of other periods of the year. The integrated amount of power generation that can be produced in daylight at the S-N orientation is less than at the E-W. Regarding the data in Fig. 4, then in July its level is 1534 W·h/m^2 and 1864 W·h/m^2, respectively.

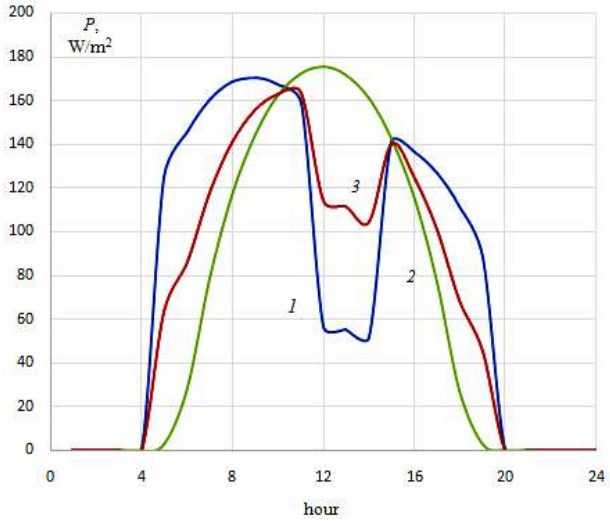

Fig. 4. Power of electric generation of the SE in the development of the day for the summer period at an angle of 45° and orientation:
1 – S-N; *2* – E-W; *3* – (S-N) + (E-W)

The nature of the curves of power change of electric generation of the SE during daylight hours correlates with the irradiation and temperature of the panel (Fig. 2-4).

These features can be opportunistically attractive in practice, and for some consumers this situation may be favorable. However, presented in Fig. 4 data allow to draw an important conclusion for practical application. The alignment of curves 1 and 2 shows that the simultaneous operation of panels with different orientations equalizes the performance of the station during daylight. The total production of electricity by panels of different orientation (curve 3) is characterized by increased uniformity and controlled integrated filling of the daily schedule. For example, the amount of daily total electricity production at the same ratio of the sizes of multidirectional panels for the data in Fig. 4 is 1699 W·h/m^2. Changing the ratio of the number of panels with different orientations allows to increase or decrease daily productivity in the range of levels of components of orientation and manage the noon decline in production. In this way, it is possible to adjust the schedules of production and consumption of energy.

From the analysis of the influence of the SE orientation on productivity it follows that the worst conditions of electricity generation are observed at the direction along the S-N axis and the angle of inclination of 90°. The E-W orientation is best at different angles. The effect of the slope on productivity in the summer is manifested to a large extent only for the installation of the SE on the S-N axis. Electrical performance increases with decreasing slope. In the period from September to April, the efficiency of the SE depends little on the installation angle. During this period, the main influence is the orientation of the SE.

Given the different degree of dependence of the SE productivity on the main parameters and the seasonality of the determinants, the most informative is the consideration of the SE productivity on the total annual indicator.

Figure 5 presents data on electricity generation during the year for the considered four options for installation of the SE. As it can be see, the best option is with the orientation on the E-W axis, the worst one – on the S-N axis. Variants with orientations on the E-W axis, an angle of inclination of 90°, and on the S-N axis, an angle of inclination of 45° are close in efficiency.

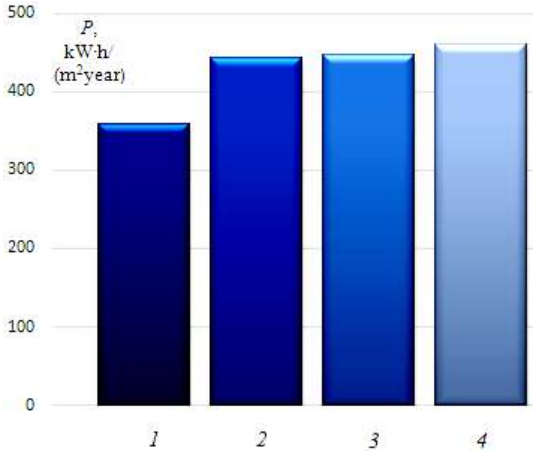

Fig. 5. Annual electricity production depending on the orientation and angle of inclination of the SE:
1 – S-N, 90°; *2* – E-W, 90°; *3* – S-N, 45°; *4* – E-W, 45°

Conclusions.

A method for determining the bifacial irradiation of solar elements has been developed, which has been used to create an integrated mathematical model of the energy mode of SE operation depending on its spatial location. The model allows to carry out more exact, in comparison with existing methods, the analysis of efficiency of operation of the SE at various ways of orientation and to create rational architecture of power plant.

According to the results of the analytical study it is shown that:

1. In summer, the temperature of the SE is almost twice that of the usually recommended (45-50 °C). The heating levels of the absorber of bifacial and one-facial panels are almost the same. However, at the E-W orientation in the afternoon, the one-facial SE heats up more. This is due to the presence of excess heat with limited use of solar energy to generate electricity.

2. The use of bifacial photo panel for all ways of orientation is positive for electrical performance. The greatest effect from the bifacial irradiation of the solar panel can be obtained by directing on the E-W axis. As the angle of inclination decreases beginning from the level of 90°, the total exposure of the panel increases. The dependence of the annual production of electricity on the angle of inclination is most pronounced for the S-N orientation, and for angles of 90° and 45° the difference reaches 26 %. The difference in annual production between the E-W and S-N orientations at the angle of inclination of 45° is small and is about 3 %.

At the angle of 90° and at the E-W direction, the annual production is 24 % higher than at the S-N orientation. Meanwhile, at the E-W orientation, the performance of the vertical panel is only 2.6 % worse compared to panels inclined at the angle of 45°. Therefore, such an arrangement is justified if used, for example, for fencing or facade cladding.

3. Combining photo panels with different methods of spatial placement allows to manage the level of electricity production during daylight hours, adjusting the schedules of production and energy consumption. Changing the ratio of the number of panels with different orientations allows to increase or decrease the daily productivity in the range of levels of components of orientation and to manage the level of the noon decline in electricity production.

Conflict of interest. The authors declare no conflict of interest.

REFERENCES

1. Gu W., Ma T., Ahmed S., Zhang Y., Peng J. A comprehensive review and outlook of bifacial photovoltaic (bPV) technology. *Energy Conversion and Management*, 2020, vol. 223, art. no. 113283. doi: https://doi.org/10.1016/j.enconman.2020.113283.

2. Guerrero-Lemus R., Vega R., Kim T., Kimm A., Shephard L.E. Bifacial solar photovoltaics – A technology review. *Renewable and Sustainable Energy Reviews*, 2016, vol. 60, pp. 1533-1549. doi: https://doi.org/10.1016/j.rser.2016.03.041.

3. Tina G.M., Scavo F.B., Gagliano A. Multilayer thermal model for evaluating the performances of monofacial and bifacial photovoltaic modules. *IEEE Journal of Photovoltaics*, 2020, vol. 10, no. 4, pp. 1035-1043. doi: https://doi.org/10.1109/jphotov.2020.2982117.

4. Zhang Z., Wu M., Lu Y., Xu C., Wang L., Hu Y., Zhang F. The mathematical and experimental analysis on the steady-state operating temperature of bifacial photovoltaic modules. *Renewable Energy*, 2020, vol. 155, pp. 658-668. doi: https://doi.org/10.1016/j.renene.2020.03.121.

5. Jaszczur M., Hassan Q., Teneta J., Majewska E., Zych M. An analysis of temperature distribution in solar photovoltaic module under various environmental conditions. *MATEC Web of Conferences, 2018, 11th International Conference on Computational Heat, Mass and Momentum Transfer (ICCHMT 2018)*, vol. 240, art. no. 04004. doi: https://doi.org/10.1051/matecconf/201824004004.

6. Bryan J.L., Silverman T.J., Deceglie M.G., Holman Z.C. Thermal model to quantify the impact of sub-bandgap reflectance on operating temperature of fielded PV modules. *Solar Energy*, 2021, vol. 220, pp. 246-250. doi: https://doi.org/10.1016/j.solener.2021.03.045.

7. Zhou J., Zhang Z., Ke H. PV module temperature distribution with a novel segmented solar cell absorbance model. *Renewable Energy*, 2019, vol. 134, pp. 1071-1080. doi: https://doi.org/10.1016/j.renene.2018.09.014.

8. Wu S.-Y., Guo H.-T., Xiao L., Chen Z.-L. Experimental investigation on thermal characteristics and output performance of PV panel under linear light source and windy conditions. *Sustainable Energy Technologies and Assessments*, 2021, vol. 43, art. no. 100918. doi: https://doi.org/10.1016/j.seta.2020.100918.
9. Ruzaimi A., Shafie S., Hassan W.Z.W., Azis N., Effendy Ya'acob M., Elianddy E. Temperature distribution analysis of monocrystalline photovoltaic-thermoelectric generator (PV-TEG) hybrid application. *Indonesian Journal of Electrical Engineering and Computer Science*, 2020, vol. 17, no. 2, pp. 858-876. doi: http://doi.org/10.11591/ijeecs.v17.i2.pp858-867.
10. Wysochin V.V. Mathematical model of a solar-plant system with the seasonal heat accumulator. *Proceedings of Odessa Polytechnic University*, 2011, iss. 2(36), pp. 125-129. (Rus). Available at: https://pratsi.opu.ua/articles/show/695 (accessed 21 June 2020).
11. Gong Y., Wang Z., Lai Z., Jiang M. TVACPSO-assisted analysis of the effects of temperature and irradiance on the PV module performances. *Energy*, 2021, vol. 227, art. no. 120390. doi: https://doi.org/10.1016/j.energy.2021.120390.
12. Wysochin V., Verstak N. Efficiency of use of a hybrid solar collector. *Proceedings of Odessa Polytechnic University*, 2018, iss. 2(55), pp. 66-71. doi: https://doi.org/10.15276/opu.2.55.2018.07.
13. Pan A.C., Del Canizo C., Luque A. Effect of thickness on bifacial silicon solar cells. *2007 Spanish Conference on Electron Devices*, 2007, pp. 234-237. doi: https://doi.org/10.1109/sced.2007.384035.

Received 03.04.2021
Accepted 12.05.2021
Published 25.06.2021

V.V. Wysochin[1], *PhD, Associate Professor,*
V.R. Nikulshin[1], *Doctor of Technical Science, Professor,*
A.E. Denysova[1], *Doctor of Technical Science, Professor,*
[1] Odessa Polytechnic State University,
1, Shevchenko Ave., Odessa, Ukraine, 65044,
e-mail: vvwin.od@gmail.com (Corresponding author),
vnikul@paco.net, alladenysova@gmail.com

How to cite this article:
Wysochin V.V., Nikulshin V.R., Denysova A.E. Investigation of orientation impact on electrical power of bifacial solar elements. *Electrical Engineering & Electromechanics*, 2021, no. 3, pp. 62-67. doi: https://doi.org/10.20998/2074-272X.2021.3.10.

UDC 621.3 https://doi.org/10.20998/2074-272X.2021.3.11

D. Sengupta, A. Datta

VALIDATION OF OPTIMAL ELECTRIC VEHICLE CHARGING STATION ALLOTMENT ON IEEE 15-BUS SYSTEM

Introduction. *The diminishing conventional energy resources and their adverse environmental impacts compelled the researchers and industries to move towards the nonconventional energy resources. Consequently, a drastic paradigm shift is observed in the power and transportation sectors from the traditional fossil fuel based to the renewable energy-based technologies. Considering the proliferation of electric vehicles, the energy companies have been working continuously to extend electric vehicle charging facilities.* ***Problem****. Down the line, the inclusion of electric vehicle charging stations to the electric grid upsurges the complication as charging demands are random in nature all over the grid, and in turn, an unplanned electric vehicle charging station installation may cause for the system profile degradation.* ***Purpose.*** *To mitigate the problem, optimum allocation of the charging stations in existing power distribution system in a strategic manner is a matter of pronounced importance in maintaining the system stability and power quality. In this paper, optimum allocation of electric vehicle charging stations in IEEE 15-bus system is studied in order to minimize the highest over and under voltage deviations.* ***Methodology.*** *Primarily, voltage stability analysis is carried out for identification of the suitable system nodes for the integration. Voltage sensitivity indices of all the system nodes are calculated by introducing an incremental change in reactive power injection and noting down the corresponding change in node voltage for all nodes. Henceforth, dynamic load-flow analysis is performed using a fast and efficient power flow analysis technique while using particle swarm optimization method in finding the optimal locations.* ***Results****. The results obtained by the application of the mentioned techniques on IEEE 15-bus system not only give the optimum feasible locations of the electric vehicle charging stations, but also provide the maximum number of such charging stations of stipulated sizes which can be incorporated while maintaining the voltage profile.* ***Originality.*** *The originality of the proposed work is the development of the objective function; voltage stability analysis; power flow analysis and optimization algorithms.* ***Practical value.*** *The proposed work demonstrates the detailed procedure of optimum electric vehicle charging station allotment. The experimental results can be used for the subsequent execution in real field.* References 15, table 1, figures 4.

Key words: **electric vehicle charging station, optimal allotment, IEEE 15-bus system, voltage stability analysis, load-flow analysis, particle swarm optimization.**

Вступ. *Зменшення традиційних енергетичних ресурсів та їх несприятливий вплив на навколишнє середовище змусили дослідників і галузі промисловості перейти до нетрадиційних енергетичних ресурсів. Отже, в енергетичному та транспортному секторах спостерігається кардинальна зміна парадигми від традиційного викопного палива до технологій, що базуються на відновлюваних джерелах енергії. Беручи до уваги розповсюдження електромобілів, енергетичні компанії постійно працюють над розширенням потужностей для зарядки електромобілів.* ***Проблема.*** *Включення зарядних станцій для електромобілів до електричної мережі викликає ускладнення, оскільки вимоги до зарядки мають випадковий характер по всій електромережі, і, в свою чергу, незапланована установка зарядної станції для електромобілів може призвести до погіршення профілю системи.* ***Мета.*** *Щоб полегшити проблему, оптимальне розміщення зарядних станцій в існуючій системі розподілу електроенергії стратегічним чином є питанням надзвичайно важливого значення для підтримки стабільності системи та якості електроенергії. У цій роботі вивчається оптимальне розміщення зарядних станцій для електричних транспортних засобів в 15-шинній системі IEEE з метою мінімізації найвищих відхилень напруги вгору та донизу.* ***Методологія.*** *В першу чергу, проводиться аналіз стабільності напруги для ідентифікації відповідних вузлів системи для інтеграції. Показники чутливості до напруги всіх вузлів системи обчислюються шляхом введення поступової зміни подачі реактивної потужності та відмітки відповідної зміни вузлової напруги для всіх вузлів. Надалі динамічний аналіз потоку навантаження виконується за допомогою швидкого та ефективного методу аналізу потоку потужності, використовуючи метод оптимізації рою частинок для пошуку оптимальних місць розташування.* ***Результати.*** *Результати, отримані при застосуванні зазначених методів на 15-шинній системі IEEE, не тільки дають оптимально можливе розташування зарядних станцій електромобілів, але також забезпечують максимальну кількість таких зарядних станцій встановлених розмірів, які можна включити, зберігаючи профіль напруги.* ***Оригінальність.*** *Оригінальність запропонованої роботи полягає у розвитку цільової функції; у аналізі стабільності напруги; у алгоритмах аналізу та оптимізації потоку потужності.* ***Практичне значення.*** *Запропонована робота демонструє детальну процедуру оптимального розподілу станцій зарядки електромобілів. Результати експериментів можуть бути використані для подальшої реалізації в реальних умовах.* Бібл. 15, табл. 1, рис. 4.

Ключові слова: **зарядна станція для електромобілів, оптимальний розподіл, 15-шинна система IEEE, аналіз стабільності напруги, аналіз потоку навантаження, оптимізація рою частинок.**

1. Introduction. Presently, the transportation sector is being transformed rapidly to adopt electric vehicles (EVs) as it is an important revolution to circumvent the depletion of conventional energy resources and their detrimental environmental impacts like global warming, public health hazards, etc. [1]. With the proliferation of EVs, there is an equivalent obligation to meet the EV charging needs. In this perspective, a massive infrastructure planning is required towards the installation of electric vehicle charging stations (EVCSs) [2]. Expansion of generation and energy storage planning is the concern to accommodate many EVCSs. The generation extension may be combined with energy storage systems. However, the generation expansion is constrained by several factors like renewable energy integration, rating of existing transmission/distribution lines, investment cost, risk assessment, long-term planning, etc. [3].

Optimal allocation of EVCSs can comfort to accommodate a substantial number of EVCSs in existing power system while sinking power losses and functioning cost in tandem with voltage stability. In recent years, several studies have been carried out in the domain of optimal sizing and allocation of the EVCSs in power distribution networks. In [4], greedy algorithm along with

three other optimization techniques was presented for maximizing the accessibility of EVCS to the EV owners. In [5], a stochastic collaborative planning for EVCS integrated distribution network was performed by utilizing a realistic traffic assignment model in conjunction with conical congestion function. Optimal placement of fast charging EVCSs for charging cost minimization using game theory was proposed in [6]. A multi-objective bi-layer Pareto optimization technique for maximizing EV parking garage profit and minimizing line loss as well as voltage deviation was pronounced in [7]. A multi-agent system (MAS) simulation framework along with evidential reasoning (ER) approach was used for minimizing the charging cost, charging waiting time and charging travel time [8].Optimal allocation of EVCSs for sharing charging level improvement and total charging distance minimization was presented [9]. In [10], a collaborative multi-aggregator EV charging scheduling for PV powered EVCSs for aggregator total profit maximization was accomplished. An optimum distributed energy trading strategy was proposed using game theory on an EVCS incorporated integrated energy system (IES) [11]. A geographic information system (GIS) based technique for PV based EVCS location analysis and evaluation was presented in [12].

Literature review reveals that less amount of work is performed in the domain of EVCS allocation in view of voltage profile retention. Another general shortfall of all these researches is the absence of voltage stability analysis which is vital to check the suitability of the nodes for power injection/absorption while retaining the system stability.

In the present work, an effective strategy for optimal allocation of EVCSs to maintain the voltage profile of a distribution network is presented. Among the different optimization techniques, the particle swarm optimization (PSO) is an easy and distinct convergence technique [13]. Thus, PSO technique is adopted in compliance with an efficient dynamic power flow analysis method. IEEE 15-bus system is taken for optimal allocation of EVCSs with respect to minimization of node voltage deviation. The optimum results obtained from the case study are substantiated with the voltage stability analysis results. A comparison of the system voltage profile with EVCS and without EVCS is presented to show the effectiveness of the optimal allocation of EVCSs.

The rest portion of this paper is structured as follows: problem formulation is included in Section 2. Voltage stability analysis is discussed in Section 3. Power flow analysis and PSO technique are described in Sections 4 and 5, respectively, whereas Section 6 presents the proposed power flow analysis collaborated PSO technique in detail. Results and discussion are placed in Section 7, and finally Section 8 concludes the paper.

The aim of the paper is to optimally allocate the maximum number of electric vehicle charging stations of specific sizes while retaining the voltage profile. In turn the system stability, power balance and power quality will be maintained.

2. Problem formulation. ***Objective function.*** The integration of several EVCSs into a distribution network can introduce severe voltage deviations in different feeders depending on the power flow. Therefore, optimal sizing and allocation of such EVCSs are very essential in maintaining the voltage deviation within the standard limit. In view of this, an objective function is formulated to minimize the highest voltage rise and drop with respect to the reference voltage.

To objective function is defined as

$$\begin{aligned} &Minimize\, E_{devihighest} = \\ &= Minimize|(\{V_{ref} - V[FN(i,1)]\},\{V_{ref} - V[FN(i,j+1)]\})| = \\ &= Minimize\,(\{|V_{ref}| - |V[FN(i,1)]|\},\{|V_{ref}| - \\ &- \{|V[FN(i,j)]| - \frac{\sqrt{(P_S[FB(i,j)])^2 + (Q_S[FB(i,j)])^2}}{|V[FN(i,j)]|} \times \\ &\times |Z[FB(i,j)]|\}\}). \end{aligned} \quad (1)$$

The voltage of the $(j + 1)^{th}$ node of the i^{th} path is

$$|V[FN(i,j+1)]| = |V[FN(i,j)]| - \frac{\sqrt{(P_S[FB(i,j)])^2 + (Q_S[FB(i,j)])^2}}{|V[FN(i,j)]|} \cdot |Z[FB(i,j)]|, \quad (2)$$

where $i = 1, ..., TN$ and $j = 1, ..., N(i) - 1$; i represents the main feeder, lateral or sublateral number of the distribution network; i^{th} path signifies the paths associated with main feeder, laterals, and sub-laterals; TN is the total number of paths of the network; j is the index for representing the nodes and branches of the i^{th} path; $N(i)$ is the maximum number of nodes present in the i^{th} path. As number of branches present in a path is exactly 1 less than the number of nodes, the total number of branches of the i^{th} path is $N(i) - 1$. Henceforth, $[FB\ (i, j)]$ presents the branches of the i^{th} path and for $j = N(i) - 1$, $[FB\ (i, j)]$ denotes the last branch of the associated i^{th} path. $[FN(i, j)]$ indicates the nodes of the allied i^{th} path. For $j = N(i) - 1$, $[FN\ (i, j)]$ presents the node just before the last node. $[FN(i, j+1)]$ presents the last node of the i^{th} path. $E_{devihighest}$ is the highest voltage (over and under voltage) errors among the node voltages of the distribution system; V_{ref} is the reference bus voltage, which is taken as $(1 + j\cdot0)$ pu. The voltage of main feeder first node $V\ [FN\ (1,1)] = (1 + + j\cdot0)$ pu. $V[FN(i,1)]$ denotes the first node voltage of the i^{th} path. $V[FN(i, j)]$ is the j^{th} node voltage of the i^{th} path. $Z[FB(i, j)]$ represents the j^{th} branch impedance of the i^{th} path. $P_S[FB(i, j)]$ and $Q_S[FB(i, j)]$ are the active and reactive power flows of the $[FB(i, j)]$ branch.

Decision variables. EVCS locations.

An array named *EVCSLOCS* is assigned to store the decision variables of the proposed optimization problem, i.e., the randomly generated EVCS locations

$$EVCSLOCS = [EVCSLOCS_1,...,EVCSLOCS_i,..., ,...,EVCSLOCS_n], \quad (3)$$

where $EVCSLOCS_i$ denotes the i^{th} EVCS location among total n number of EVCS locations.

The operating range of $EVCSLOCS_i$ is restricted to $[FN(i, j)]$; for $i = 1$, $j = 2,...,N(i)$ and for $i = 2,...,TN$, $j = 1,...,N(i)$. The total number of EVCSs (n) varies based on the requirements of different case studies.

Maximum powers of the EVCSs.

Two arrays named P_{EVstn} and Q_{EVstn} are assigned to hold the active and reactive power capacities of the EVCSs

$$P_{EVstn} = [P_{EVstn1}, ..., P_{EVstni}, ..., P_{EVstnn}]; \quad (4)$$

$$Q_{EVstn} = [Q_{EVstn1}, ..., Q_{EVstni}, ..., Q_{EVstnn}], \quad (5)$$

where n is the numbers of EVCSs are to be allocated; P_{EVstni} and Q_{EVstni} are an active and reactive power capacities of i^{th} EVCS (EVCS$_i$) respectively.

Bus voltage constraints.

$$V_{\min} \le V[FN(i,j)] \le V_{\max} \quad (6)$$

where $V[FN(i, j)]$ represents the node voltages of the distribution network.

The $V_{\min}$ and $V_{\max}$ are taken as 0.9 pu and 1.1 pu respectively for primary distribution.

3. Voltage stability analysis. Voltage stability analysis is a mandate to identify the suitable nodes appropriate for load point integration [14] in view of retaining the overall system stability. For checking the stability of the network due to integration of EVCS at different nodes accept the swing bus, the voltage sensitivity analysis of all these nodes is essential. For a decoupled network, the voltage sensitivity is dominantly reliant on its reactive power sensitivity ($\delta Q_n/\delta V_n$). The voltage sensitivity index (VSI) for n^{th} node is defined as

$$VSI\,|_n = \frac{\delta V_n}{\delta Q_n}. \quad (7)$$

where δQ_n and δV_n represent the incremental changes in n^{th} node reactive power Q_n and voltage V_n respectively. The term ($\delta Q_n/\delta V_n$) represents the ratio of the two incremental changes. $\delta V_n/\delta Q_n$ is the reciprocal of the aforesaid ratio. It denotes the incremental change in node voltage δV_n subjected to a corresponding incremental change in reactive power Q_n and is called the VSI of the n^{th} node.

Positive value of VSI indicates a suitable node for load point inclusion, whereas, negative VSI implies an unstable node. The less value of positive VSI infers a more stable node and vice versa.

4. Power flow analysis. An efficient power flow analysis method [15] is utilized along with the PSO optimization technique for dynamic power flow and node voltage calculation. The governing equations of this method are

$$|I[FB(i,j)]_{new}| = \frac{|V[FN(i,j)]_{old}| - |V[FN(i,j+1)]_{old}|}{|Z[FB(i,j)]|}; \quad (8)$$

$$LP[FB(i,j)]_{new} = |I[FB(i,j)]_{new}|^2 \cdot R[FB(i,j)]; \quad (9)$$

$$LQ[FB(i,j)]_{new} = |I[FB(i,j)]_{new}|^2 \cdot X[FB(i,j)]; \quad (10)$$

$$|V[FN(i,j+1)]_{new}| = |V[FN(i,j)]_{new}| - \frac{\sqrt{(P_S[FB(i,j)])_{new}^2 + (Q_S[FB(i,j)])_{new}^2}}{|V[FN(i,j)]_{new}|} \times |Z[FB(i,j)]|, \quad (11)$$

where, i = 1, ..., TN and j = 1, ..., $N(i) - 1$. The notations used in this section are like the notations mentioned in «*objective function*» section. $V[FN(i, j)]$, $I[FB(i, j)]$, $LP[FB(i, j)]$ and $LQ[FB(i, j)]$ are the relevant node voltage, line current, line active and reactive power losses respectively. The active and reactive power flows from the branch $[FB(i, j)]$ are $P_S[FB(i, j)]$ and $Q_S[FB(i, j)]$ respectively, which are dependent upon the values of $LP[FB(i, j)]$, $LQ[FB(i, j)]$, $P_L[FN(i, j)]$, $Q_L[FN(i, j)]$ and the system configuration. $P_L[FN(i, j)]$ and $Q_L[FN(i, j)]$ are the load active and reactive powers connected to the $[FN(i, j)]$ node. The subscript «*new*» represents the running iteration of power flow, whereas subscript «*old*» denotes the previous iteration.

5. PSO algorithm. PSO [13] is a population-driven algorithm which shows a good resemblance with the flock of birds searching for food in a search space. The entire population is called the swarm and individual members of the swarm are called particles. In contrast to the conventional optimization techniques, PSO gives faster convergence, identification of global optima in presence of local optima along with the features of simplicity in programming and adaptability for the constrained problems.

The governing equations for PSO algorithm are

$$V_i(t) = \omega(t) \cdot V_i(t-1) + c_1 \cdot r_1 \cdot (P_i(t-1) - X_i(t-1)) + c_2 \cdot r_2 \cdot (G(t-1) - X_i(t-1)); \quad (12)$$

and

$$X_i(t) = X_i(t-1) + V_i(t), \quad (13)$$

where X_i and V_i symbolize the position and velocity of the i^{th} particle, and are denoted by X_i = [x_{i1}, ..., x_{in}] and V_i = [v_{i1}, ..., v_{in}]. These are the arrays, which contain the position and velocity of the i^{th} particle. P_i and G are the arrays containing the local best position of the i^{th} particle and global best position of all the particles of the swarm ever visited in each iteration. Symbol «*t*» represents the current iteration number and (t – 1) signifies the previous iteration number, 1 ≤ t ≤ $IT_{\max}$, where $IT_{\max}$ is the maximum iteration number.

When t = 1 the $V_i(t - 1)$, $X_i(t - 1)$, $P_i(t - 1)$ and $G(t - 1)$ present $V_i(0)$, $X_i(0)$, $P_i(0)$ and $G(0)$ respectively. These are the 0^{th} iteration (initial) values of velocity, position, best position of i^{th} particle and global best position of the entire swarm. Before starting the iteration process, initialization of all the particles' position, velocity, particles' best position and global best position of the entire swarm is accomplished. The entire swarm size or population of all the particles is denoted by n_{pop}. Therefore, 1 ≤ i ≤ n_{pop}. At first, x_{i1} to x_{in} (the positions of n numbers of decision variables) of all the particles are initialized by generating random values in n dimensional search space. Velocities (V_i) of all the particles are initialized by storing zeros. After initialization of particles' position and velocity arrays, the objective function is calculated. Particle's best position P_i is initialized by assigning the same initial random values stored inside the X_i array for all particles. Particle's initial objective function value is stored inside the particle's best objective function array for initialization. Global best objective function is initialized by taking (0) or (inf) for the maximization and minimization problems respectively. Gradually, with the initialization of each particle's best values; continuous updating of global best values (global best position G along with global best objective function value) for the entire swarm is completed to achieve the final initialized global best values. ω is the inertia coefficient. At first iteration, usually its value is taken as 1 for the entire swarm and gradually at successive iterations, its value decreases to

almost zero if damping inertia coefficient, ω_{damp} is introduced. $\omega(t) = \omega(T-1)\cdot\omega_{damp}$. c_1, c_2 are the cognitive and social parameters respectively, and r_1, r_2 denote random numbers.

6. Power flow coordinated PSO technique. To attain minimum values of highest over and under voltage deviations ($E_{overvol-h}$ and $E_{undervol-h}$) in accommodating multiple numbers of EVCSs in a distribution network, PSO is exploited with power flow method. The maximum power handling capacities of EVCSs are selected considering different relevant factors. After selection of the EVCS capacities, the next step is to generate random EVCS locations within the lower and upper bounds of distribution feeder to initialize the entire swarm. These random EVCS locations generated inside the PSO algorithm for each particle are sent chronologically inside the power flow analysis function as input arguments. System data along with the EVCS capacities are encumbered inside the power flow algorithm. The distribution network data is updated inside the power flow algorithm based on these random EVCS locations. The power flow algorithm executes concurrently with the PSO method. Figure 1 shows the flow chart of the proposed power flow coordinated PSO technique.

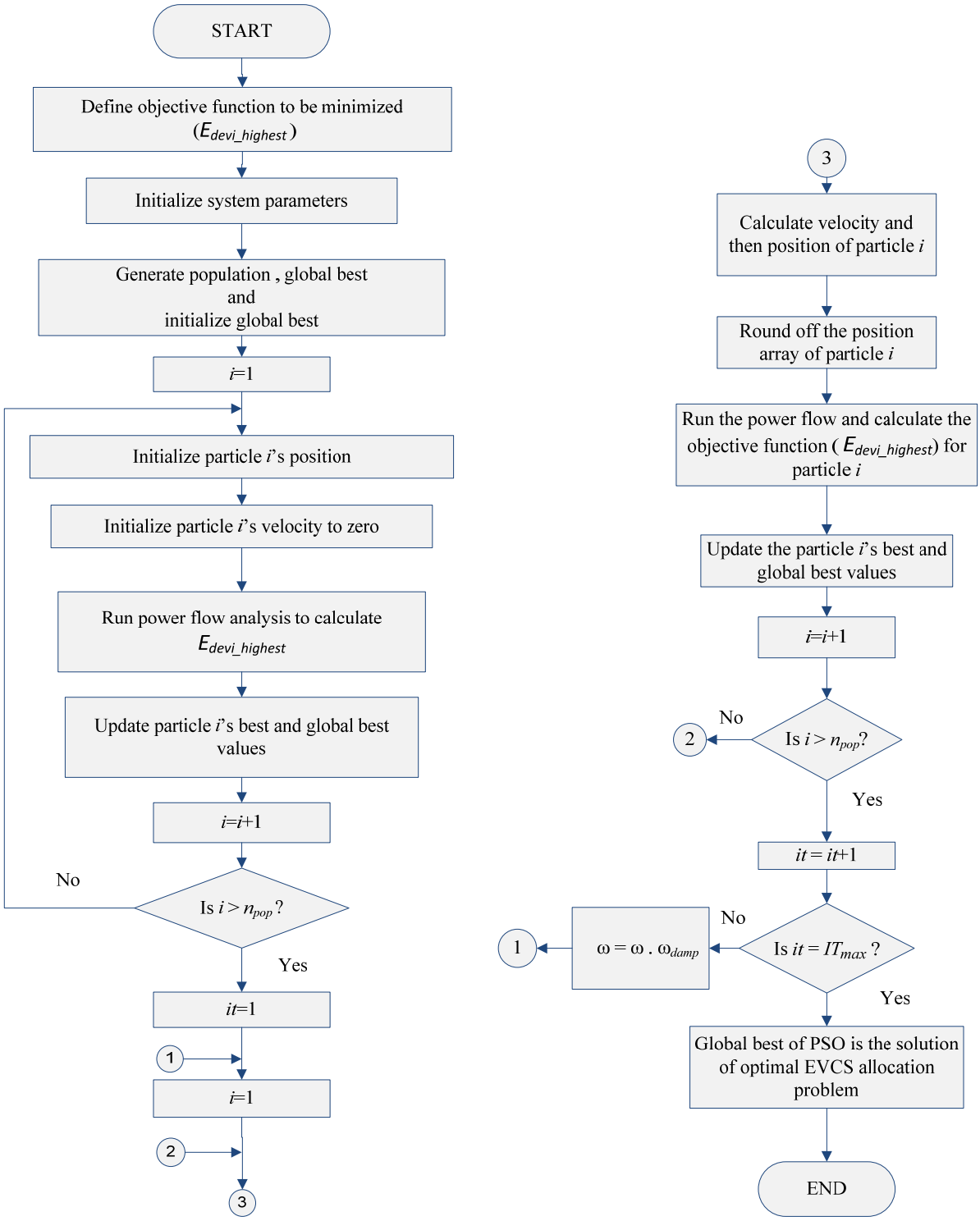

Fig. 1. Flow chart of the power flow coordinated PSO technique

7. Results and discussion. The IEEE 15-bus radial distribution system, shown in Fig. 2 is taken for the case study. The active and reactive power demands are 1126.5 kW and 1251.182 kVAR respectively. The base values are chosen as 100 MVA, 11 kV. The normalized voltage sensitivity indices of all nodes are calculated by finding out the $\delta V_n/\delta Q_n$ value of the n^{th} node, where $n = [FN(i, j)]$, excluding the main feeder first node. For this purpose, an incremental change in reactive power of the n^{th} node is introduced and the corresponding incremental change in node voltage is obtained by applying power flow analysis. Figure 3 presents the normalized voltage sensitivity indices of the test network.

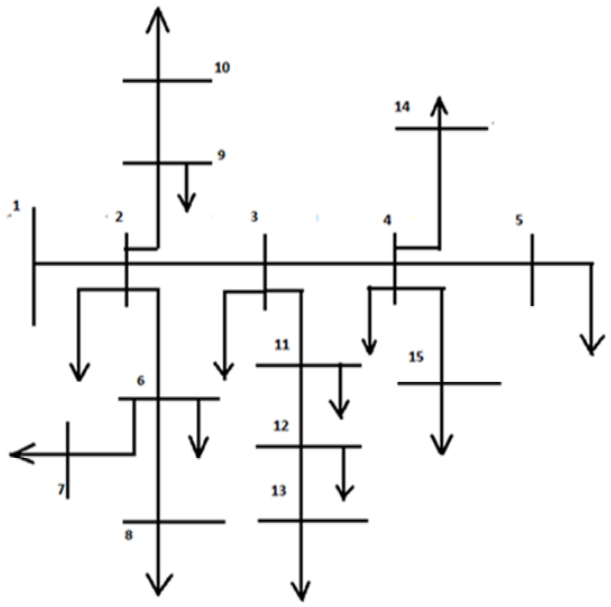

Fig. 2. IEEE 15-bus system

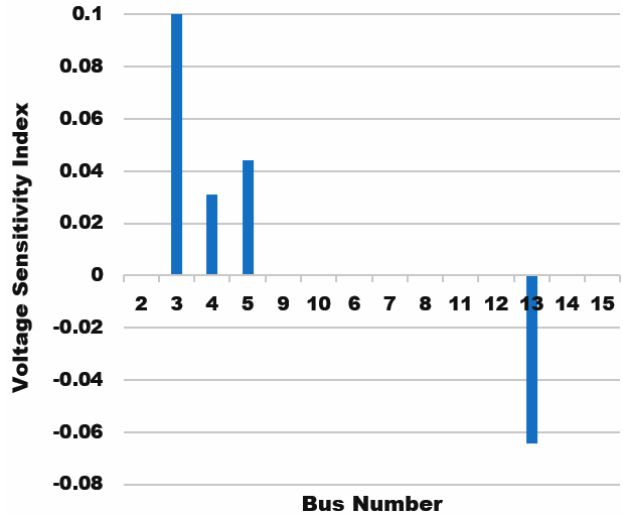

Fig. 3. Normalized voltage sensitivity indices of 15-bus system

It is observed that node number 13 is inappropriate for power injection or extraction into the system as the VSI value of this node is negative. Other nodes are having positive VSIs and guarantee the sustained stability of the system. But amidst them, node numbers 3, 4 and 5 attain high values of VSI. Therefore, these are the comparatively weaker nodes. Amongst these three nodes, node 3 is unsuitable for power injection as the VSI value of this node is very high. The other two nodes, i.e. nodes 4 and 5, can be considered for EVCS integration. After sensitivity analysis, gradually augmented numbers of identical EVCSs are approached to investigate the effect of newly integrated EVCSs upon the system voltage profile. The motive is to find out the maximum number of such EVCSs that the network can accommodate without compromising the voltage profile. The proposed power flow collaborated PSO technique is utilized for this purpose. For the execution of the PSO algorithm, the value of ω_{damp} is taken as 0.99. c_1 and c_2 are set to 0.5 each. r_1 and r_2 are taken from the uniform distribution interval [0 1]. For deciding the capacity of each EVCS, maximum 2 EV charging requirement per EVCS is considered. Considering 8 kW DC charger, the total power consumed by 2 EVs are 16(2×8) kW DC. Rectifier efficiency is 90 %. Henceforth, the rectifier input power is 17.78 (16×100/90) kVA AC. Taking grid load power factor as 0.7, the active and reactive powers drawn from the grid by each EVCS are 12.446 (17.78×0.7) kW and 12.7 (17.78×0.7141) kVAR correspondingly. The per unit values of these powers are 0.00012446 pu and 0.000127 pu. Four trials are carried out considering 2, 3, 4 and 5 EVCS allocation. In each trial, the global best values i.e. optimum values of highest over and under voltage deviations ($E_{overvol-h}$ and $E_{undervol-h}$) along with the optimum EVCS locations are captured. The results are illustrated in Table 1.

Table 1

Optimum feasible EVCS locations for gradually augmented EVCS numbers along with the optimum voltage errors

No. of EVCSs ↓	Optimum feasible EVCS Locations →				$E_{overvol-h}$ (in pu)	$E_{undervol-h}$ (in pu)	
2	9	10				0.0472	0
3	8	9	10			0.0475	0
4	**7**	**8**	**9**	**10**		**0.0478**	**0**
5	3	8	9	10	10	0.483	0

From the results, it is seen that maximum 4 numbers of EVCSs of stipulated sizes are feasible to be integrated at optimum locations 7, 8, 9 and 10. Increasing the EVCS number to 5 gives two repeated optimum locations at node number 10 which is not suitable for implementation. The optimum nodes 7, 8, 9 and 10 achieved from this case study are verified with the results of sensitivity analysis and found to be satisfactory. The highest over and under voltage errors are substantially lesser (0.0033 pu and 0 pu) compared to the stipulated voltage errors limits (± 0.1 %). That's why these locations are considered as the optimum locations for EVCS integration.

Figure 4 shows a comparison in between the voltage profiles of the system with EVCS and without EVCS. From this analysis, it is observed that voltage profile of the system with EVCS is far better than that of without EVCS. For the system without EVCS, the highest over and under voltage errors are 0 pu and 0.0554 pu, respectively.

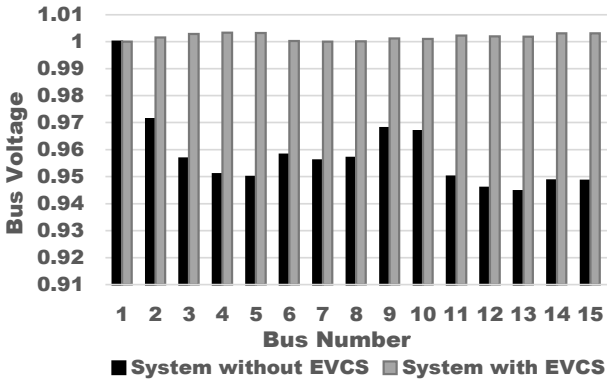

Fig. 4 Comparison of node voltage profile with and without EVCS for 15-bus system

8. Conclusions.

Optimal allocation of electric vehicle charging stations in an existing power distribution system is of great importance for maintaining voltage profile. An effective strategy, i.e. power flow analysis coordinated with particle swarm optimization, is applied for the deployment of electric vehicle charging stations in a distribution network with the intention of optimal power flow and voltage profile improvement. Voltage stability analysis is carried out by calculating the voltage sensitivity indices of the network nodes to identify the suitable nodes for the integration. IEEE 15-bus system is taken to validate the usefulness of the anticipated procedure. Comparison of system voltage profiles with and without electric vehicle charging stations is presented to reveal the effectiveness of the optimal allocation with the proposed strategy.

Conflict of interest. The authors declare that they have no conflicts of interest.

REFERENCES

1. Xu X., Yao L., Zeng P., Liu Y., Cai T. Architecture and performance analysis of a smart battery charging and swapping operation service network for electric vehicles in China. *Journal of Modern Power Systems and Clean Energy*, 2015, vol. 3, no. 2, pp. 259-268. doi: https://doi.org/10.1007/s40565-015-0118-y.

2. Fathabadi H. Novel solar powered electric vehicle charging station with the capability of vehicle-to-grid. *Solar Energy*, 2017, vol. 142, pp. 136-143. doi: https://doi.org/10.1016/j.solener.2016.11.037.

3. Mehrjerdi H. Dynamic and multi-stage capacity expansion planning in microgrid integrated with electric vehicle charging station. *Journal of Energy Storage*, 2020, vol. 29, no. 101351, pp. 1-11. doi: https://doi.org/10.1016/j.est.2020.101351.

4. Lam A. Y. S., Leung Y.-W., Chu X. Electric vehicle charging station placement: formulation, complexity, and solutions. *IEEE Transactions on Smart Grid*, 2014, vol. 5, no. 6, pp. 2846-2856. doi: https://doi.org/10.1109/tsg.2014.2344684.

5. Wang S., Dong Z. Y., Luo F., Meng K., Zhang Y. Stochastic collaborative planning of electric vehicle charging stations and power distribution system. *IEEE Transactions on Industrial Informatics*, 2018, vol. 14, no. 1, pp. 321-331. doi: https://doi.org/10.1109/tii.2017.2662711.

6. Xiong Y., Gan J., An B., Miao C., Bazzan A. L. C. Optimal electric vehicle fast charging station placement based on game theoretical framework. *IEEE Transactions on Intelligent Transportation Systems*, 2018, vol. 19, no. 8, pp. 2493-2504. doi: https://doi.org/10.1109/tits.2017.2754382.

7. Faddel S., Elsayed A. T., Mohammed O. A. Bilayer multi-objective optimal allocation and sizing of electric vehicle parking garage. *IEEE Transactions on Industry Applications*, 2018, vol. 54, no. 3, pp. 1992-2001. doi: https://doi.org/10.1109/tia.2018.2803151.

8. Jiang C., Jing Z., Ji T., Wu Q. Optimal location of PEVCSs using MAS and ER approach. *IET Generation, Transmission & Distribution*, 2018, vol. 12, no. 20, pp. 4377-4387. doi: https://doi.org/10.1049/iet-gtd.2017.1907.

9. Gong D., Tang M., Buchmeister B., Zhang H. Solving location problem for electric vehicle charging stations – a sharing charging model. *IEEE Access*, 2019, vol. 7, pp. 138391-138402. doi: https://doi.org/10.1109/access.2019.2943079.

10. Gupta V., Konda S.R., Kumar R., Panigrahi B.K. Collaborative multi-aggregator electric vehicle charge scheduling with PV-assisted charging stations under variable solar profiles. *IET Smart Grid*, 2020, vol. 3, no. 3, pp. 287-299. doi: https://doi.org/10.1049/iet-stg.2019.0088.

11. Wang Y., Wang X., Shao C., Gong N. Distributed energy trading for an integrated energy system and electric vehicle charging stations: A Nash bargaining game approach. *Renewable Energy*, 2020, vol. 155, pp. 513-530. doi: https://doi.org/10.1016/j.renene.2020.03.006.

12. Zhou J., Wu Y., Wu C., He F., Zhang B., Liu F. A geographical information system based multi-criteria decision-making approach for location analysis and evaluation of urban photovoltaic charging station: A case study in Beijing. *Energy Conversion and Management*, 2020, vol. 205, no. 112340, pp. 1-21. doi: https://doi.org/10.1016/j.enconman.2019.112340.

13. Qu B., Li C., Liang J., Yan L., Yu K., Zhu Y. A self-organized speciation based multi-objective particle swarm optimizer for multimodal multi-objective problems. *Applied Soft Computing*, 2020, vol. 86, no. 105886, pp. 1-28. doi: https://doi.org/10.1016/j.asoc.2019.105886.

14. Roy P., Das P.K. Reactive power sensitivity index based voltage stability analysis to a real system (400 kV system of WBSEB). *International Journal of Electronics & Communication Technology,* 2013, vol. 4, no. Spl-1, pp. 167-169. Available at: iject.org/vol4/spl1/c0055.pdf (accessed 12 October 2020).

15. Ghosh S., Sherpa K.S. An efficient method for load-flow solution of radial distribution networks. *International Journal of Electrical and Computer Engineering*, 2008, vol. 2, no. 9, pp. 2094-2101. Available at: publications.waset.org/8855/an-efficient-method-for-loadflow-solution-of-radial-distribution-networks (accessed 12 October 2020).

Received 27.03.2021
Accepted 03.05.2021
Published 25.06.2021

Debaparna Sengupta [1], *PhD Student, Assistant Professor,*
Asim Datta [2], *PhD, Associate Professor,*
[1] Department of Electrical Engineering,
Techno International New Town,
Rajarhat, Kolkata-700156, Kolkata, India,
e-mail: imdebaparna@gmail.com (Corresponding author)
[2] Department of Electrical Engineering,
Mizoram University,
Aizawl-796004, Mizoram, India,
e-mail: asimdatta2012@gmail.com

How to cite this article:
Sengupta D., Datta A. Validation of optimal electric vehicle charging station allotment on IEEE 15-bus system. *Electrical Engineering & Electromechanics*, 2021, no. 3, pp. 68-73. doi: https://doi.org/10.20998/2074-272X.2021.3.11.

Матеріали приймаються за адресою:
Кафедра "Електричні апарати", НТУ "ХПИ", вул. Кирпичова, 21, м. Харків, 61002, Україна
Електронні варіанти матеріалів по e-mail: a.m.grechko@gmail.com

Довідки за телефонами: +38 050 653 49 82 Клименко Борис Володимирович
+38 067 359 46 96 Гречко Олександр Михайлович

Передплатний індекс: 01216